Analysis of the CP structure of the Yukawa coupling between the Higgs boson and τ leptons in proton-proton collisions at $\sqrt{s} = 13$ TeV

The CMS collaboration

E-mail: cms-publication-committee-chair@cern.ch

ABSTRACT: The first measurement of the CP structure of the Yukawa coupling between the Higgs boson and τ leptons is presented. The measurement is based on data collected in proton-proton collisions at $\sqrt{s} = 13$ TeV by the CMS detector at the LHC, corresponding to an integrated luminosity of $137\,\mathrm{fb}^{-1}$. The analysis uses the angular correlation between the decay planes of τ leptons produced in Higgs boson decays. The effective mixing angle between CP-even and CP-odd τ Yukawa couplings is found to be $-1 \pm 19^\circ$, compared to an expected value of $0 \pm 21^\circ$ at the 68.3% confidence level. The data disfavour the pure CP-odd scenario at 3.0 standard deviations. The results are compatible with predictions for the standard model Higgs boson.

https://doi.org/10.1007/JHEP06(2022)012

Contents

1 Introduction

In the standard model (SM), the electroweak symmetry breaking is postulated via the Brout-Englert-Higgs mechanism [1–6]. This mechanism predicts the existence of a scalar particle, the Higgs boson (H). A particle compatible with this boson was discovered by the ATLAS [7] and CMS [8, 9] Collaborations at the LHC using proton-proton (pp) collision data collected in 2011 and 2012 at centre-of-mass energies of 7 and 8 TeV, respectively. Since 2012, the couplings of the Higgs boson to heavy quarks, leptons, and gauge bosons have been measured, including the coupling to τ leptons [10–12], and the most recent measurement of its mass value yields 125.38 ± 0.14 GeV [13].

The SM H is even under charge-parity (CP) inversion. A sizeable deviation from a pure CP-even interaction of the H with any of the SM particles would be a direct indication of physics beyond the SM. Therefore, the CP structure of the couplings of the H is of paramount interest. The CMS and ATLAS Collaborations have studied the couplings of the H to vector gauge bosons, including tests of CP violation [14–27]. These studies excluded pure pseudoscalar (CP-odd) interactions of the H with the W and Z bosons (referred to collectively as V bosons).

There are strong theoretical motivations to search for CP-violating effects in couplings of the H to fermions rather than V bosons. In couplings to V bosons, CP-odd contributions enter via nonrenormalisable higher-order operators that are suppressed by powers of $1/\Lambda^2$ [28–30], where Λ is the scale of the physics beyond the SM in an effective field theory. Therefore, these are expected to only yield a small contribution to the coupling. A renormalisable CP-violating Higgs-to-fermion coupling may occur at tree level. The τ lepton and top quark Yukawa couplings, H$\tau\tau$ and Htt, respectively, are therefore the optimal couplings for CP studies in pp collisions [31], and measurements of these two couplings are complementary. Recently, both the CMS [32] and ATLAS [33] Collaborations presented first measurements of the CP structure of the H coupling to top quarks. The CMS result rejects the purely CP-odd hypothesis with a significance of 3.2 standard deviations, σ, while the ATLAS analysis rejects it with a significance of 3.9σ. The CMS and ATLAS Collaborations have also studied the CP-nature of the H interaction with gluons [21, 34] which was found to be consistent with the SM expectation, albeit with limited sensitivity. Such studies may also be interpreted in terms of the H coupling to top quarks, under the assumption that the interaction is mediated predominantly via top quark loops.

The CP-properties of the H $\to \tau\tau$ process is commonly described in terms of an effective mixing angle $\alpha^{\mathrm{H}\tau\tau}$, which is virtually equal to 0° in the SM. The measurement of

Mode	$e^\pm\nu\nu$	$\mu^\pm\nu\nu$	$h^\pm\nu$	$h^\pm\pi^0\nu$	$h^\pm\pi^0\pi^0\nu$	$h^\pm h^\mp h^\pm\nu$
Type	τ_e	τ_μ	τ_h	τ_h	τ_h	τ_h
$\mathcal{B}(\%)$	17.8	17.4	11.5	25.9	9.5	9.8
Resonance	—	—	—	$\rho(770)$	$a_1(1260)$	$a_1(1260)$
Symbol	e	μ	π	ρ	a_1^{1pr}	a_1^{3pr}

Table 1. Decay modes of τ leptons used in this analysis and their branching fractions $\mathcal{B}$ [38]. Where appropriate, we indicate the known intermediate resonances. The last row gives the shorthand notation for the decays used throughout this paper.

a nonzero $\alpha^{H\tau\tau}$ would therefore directly contradict the SM predictions, and have implications for beyond the SM physics models, such as two-Higgs-doublet models [35], including supersymmetry. For example, in the minimal supersymmetric model *CP* violation in the Higgs-to-fermion couplings is expected to be small and therefore the measurement of a sizeable mixing angle would disfavour such scenarios. In contrast, in the next-to-minimal supersymmetric model, $\alpha^{H\tau\tau}$ can be as large as 27° [36]. Feasibility studies have indicated that the LHC experiments can measure $\alpha^{H\tau\tau}$ to a precision of about 5–10° with $3\,\mathrm{ab}^{-1}$ of data [29, 37].

In this paper we present the first measurement of the *CP* structure of the H coupling to τ leptons. This analysis uses the pp data sets collected by the CMS detector at $\sqrt{s} = 13\,\mathrm{TeV}$ in 2016, 2017, and 2018. These correspond to integrated luminosities of 35.9, 41.5, and $59.7\,\mathrm{fb}^{-1}$, respectively. This analysis targets the most sensitive $\tau_h\tau_h$, $\tau_\mu\tau_h$ and $\tau_e\tau_h$ decay channels, where a τ lepton decaying to hadrons is denoted as τ_h, and a τ lepton decaying to a muon or an electron as τ_μ or τ_e (or collectively as τ_ℓ), respectively. The decays into light leptons are accompanied by two neutrinos, while the hadronic modes involve one neutrino. These particles are not directly detected but result in a transverse momentum imbalance which can be used to partially constrain the $\tau\tau$ system. In total, this analysis covers about 70% of all possible τ lepton pair decay modes. Table 1 summarises the τ lepton decay modes used in this analysis, their branching fractions, and the shorthand symbols that we use to denote them in the rest of this paper. The charged hadrons are denoted by the symbol $h^\pm$, which consist mainly of charged pions but include a smaller contribution from charged kaons. Throughout this paper we will assume that all $h^\pm$ are charged pions ($\pi^\pm$) since the CMS detector is not able to distinguish between different types of $h^\pm$.

This paper is organised as follows. The parameterisation of the *CP* properties of the τ Yukawa coupling is discussed in section 2. In section 3 the experimental setup is outlined, and this is followed by a discussion of the data sets and simulated samples in section 4. Subsequently, the event reconstruction is presented in section 5. Thereafter, in section 6 the *CP*-sensitive observables used to extract the results are outlined. In section 7 the event selection is presented. The estimation of the backgrounds is discussed in section 8. The techniques used to distinguish the signal from the background events are outlined in section 9. In section 10 various distributions that are used to extract the results are displayed and discussed. In section 11 the systematic uncertainties are presented. The results are discussed in section 12, and a summary of the analysis is given in section 13.

2   Parametrisation of the *CP* properties of the τ Yukawa coupling

We parameterise the Lagrangian for the τ Yukawa coupling in terms of the coupling strength modifiers κ_τ and $\widetilde{\kappa}_\tau$ that parameterise the *CP*-even and *CP*-odd contributions, respectively [31]:

$$\mathcal{L}_{\mathrm{Y}} = -\frac{m_\tau}{v} \mathrm{H}(\kappa_\tau \bar{\tau}\tau + \widetilde{\kappa}_\tau \bar{\tau} i\gamma_5 \tau). \tag{2.1}$$

In this equation, m_τ is the mass of the τ lepton, τ denotes the Dirac spinor of τ lepton fields, and the vacuum expectation value of the Higgs field, v, has a value of 246 GeV. The effective mixing angle $\alpha^{\mathrm{H}\tau\tau}$ for the Hττ coupling is defined in terms of the coupling strengths as

$$\tan(\alpha^{\mathrm{H}\tau\tau}) = \frac{\widetilde{\kappa}_\tau}{\kappa_\tau}, \tag{2.2}$$

while the fractional contribution of the *CP*-odd coupling $f_{CP}^{\mathrm{H}\tau\tau}$ is obtained from the mixing angle as $f_{CP}^{\mathrm{H}\tau\tau} = \sin^2(\alpha^{\mathrm{H}\tau\tau})$. A mixing angle of $\alpha^{\mathrm{H}\tau\tau} = 0\,(90)^\circ$ corresponds to a pure scalar (pseudoscalar) coupling. For any other value of $\alpha^{\mathrm{H}\tau\tau}$, the H has a mixed coupling with *CP*-even and *CP*-odd components, with maximal mixing at a value of $\pm 45^\circ$.

The angle ϕ_{CP} denotes the angle between the τ lepton decay planes in the H rest frame. An illustration of the decay planes in the single pion channel is depicted in figure 1. The relation between $\alpha^{\mathrm{H}\tau\tau}$ and ϕ_{CP} may be inferred from the decay of a H via τ leptons to two outgoing charged particles [39] as

$$\frac{\mathrm{d}\Gamma}{\mathrm{d}\phi_{CP}}(\mathrm{H} \to \tau^+\tau^-) \sim 1 - b(E^+)b(E^-)\frac{\pi^2}{16}\cos(\phi_{CP} - 2\alpha^{\mathrm{H}\tau\tau}). \tag{2.3}$$

In this equation, the outgoing charged particles have an energy $E^\pm$ in their respective τ rest frames. The functions b are spectral functions [40] that encapsulate the correlation between the τ spin and the momentum of the outgoing charged particle. We note that the spectral functions for the leptonic and various hadronic decays are different.
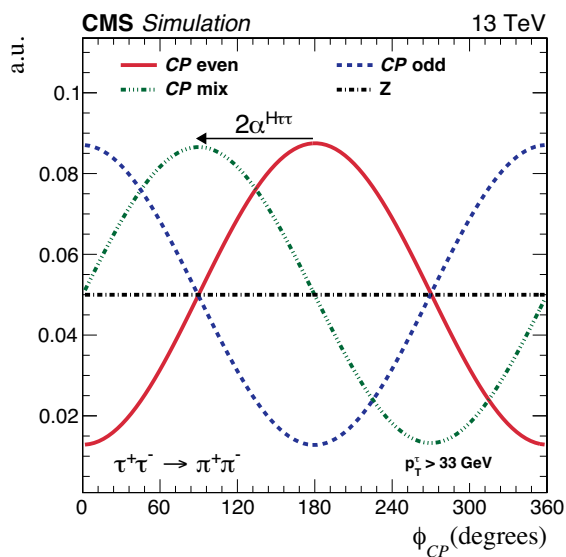
Figure 2 shows the normalised distribution of ϕ_{CP} at the generator level, calculated in the rest frame of the H, for the scalar, pseudoscalar, and maximally mixed values of $\alpha^{\mathrm{H}\tau\tau}$, as well as the ϕ_{CP} distribution from Drell-Yan processes. The simulated event samples that are used to generate these distributions are discussed in section 4. These distributions are for the scenario where both τ leptons decay to a charged pion and a neutrino.

There is a phase shift between different mixing scenarios such that the difference in ϕ_{CP} equals two times the difference in $\alpha^{\mathrm{H}\tau\tau}$, as given by eq. (2.3). It is important to note that the distribution of ϕ_{CP} for the Drell-Yan background is constant; we will exploit this symmetry to reduce statistical fluctuations in the background estimates, as explained in section 9.

The observable ϕ_{CP} was originally introduced in the context of $\mathrm{e^+e^-}$ collisions [41, 42] where the τ lepton momenta can be reconstructed and thus ϕ_{CP} can be calculated in the H rest frame. In hadronic collisions the momenta of the neutrinos cannot be well constrained, except for the configuration in which both τ leptons decay via the $\mathrm{a_1^{3pr}}$ mode to three charged pions — where the momenta of the τ leptons can be further constrained from the
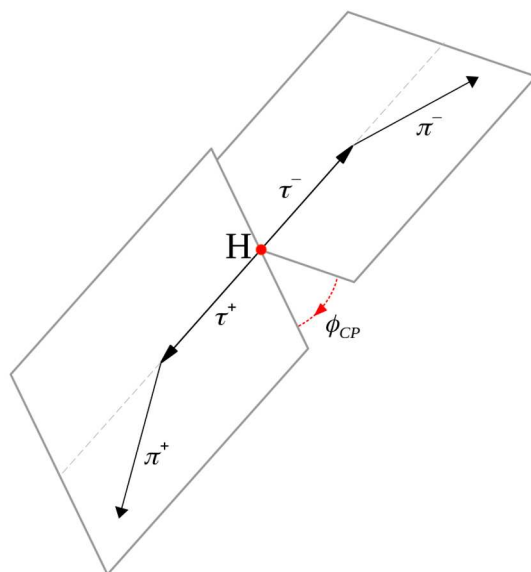
Figure 1. The decay planes of two τ leptons decaying to a single charged pion. The angle ϕ_{CP} is the angle between the decay planes. The illustration is in the H rest frame.

Figure 2. The normalised distribution of ϕ_{CP} between the τ lepton decay planes in the H rest frame at the generator level, for both τ leptons decaying to a charged pion and a neutrino. The distributions are for a decaying scalar (*CP*-even, solid red), pseudoscalar (*CP*-odd, dash blue), a maximal mixing angle of 45° (*CP*-mix, dash-dot-dot green), and a Z vector boson (black dash-dot). The transverse momentum of the visible τ decay products p_T^τ was required to be larger than $33\,\text{GeV}$ during the event generation.

reconstruction of the τ lepton production and decay vertices. Therefore, the methods for estimating ϕ_{CP} have been extended and optimised for hadronic collisions [37], as discussed in section 6. Throughout this document, we will denote the angle between the τ decay planes as ϕ_{CP}, irrespective of the frame in which it is calculated.

3   The CMS detector

The central feature of the CMS apparatus is a superconducting solenoid of 6 m internal diameter, providing a magnetic field of 3.8 T. Within the solenoid volume are a silicon pixel and strip tracker, a lead tungstate crystal electromagnetic calorimeter (ECAL), and a brass and scintillator hadron calorimeter (HCAL), each composed of a barrel and two endcap sections. Forward calorimeters extend the pseudorapidity (η) coverage provided by the barrel and endcap detectors. Muons are detected in gas-ionisation chambers embedded in the steel flux-return yoke outside the solenoid. Events of interest are selected using a two-tiered trigger system. The first level (L1), composed of custom hardware processors, uses information from the calorimeters and muon detectors to select events at a rate of around 100 kHz within a fixed latency of about 4 μs [43]. The second level, known as the high-level trigger, consists of a farm of processors running a version of the full event reconstruction software optimised for fast processing, and reduces the event rate to around 1 kHz before data storage [44]. A more detailed description of the CMS detector, together with a definition of the coordinate system used and the relevant kinematic variables, can be found in ref. [45].

4   Simulated samples

The signal and relevant background processes are modelled with samples of Monte Carlo simulated events. The signal samples with a H produced through gluon-gluon fusion (ggH), vector boson fusion (VBF), or in association with a W or Z vector boson (denoted as WH or ZH, or VH when combined) are generated at next-to-leading order (NLO) in perturbative quantum chromodynamics (QCD) with the POWHEG 2.0 [46–52] event generator. The H production mechanism is configured to only produce scalar Higgs bosons, as opposed to pseudoscalar Higgs bosons or mixed couplings. The latter scenarios would also affect various properties of the production, e.g. the production rate and the topology of associated jets, such as the azimuthal angle $\Delta\phi_{jj}$ between the two leading jets, when present [53]. We note that in our analysis of $\alpha^{H\tau\tau}$ we are not sensitive to the modifications to the ggH and VBF+VH production rates as we treat them as unconstrained parameters that are allowed to float freely in the fit to data. We also do not use the $\Delta\phi_{jj}$ or similar variables to define event selection criteria or as inputs to discriminants; whereas modifications to other kinematic variables must be negligibly small in order to avoid experimental bounds from dedicated measurements (e.g. ref. [21]). For the ggH production process, we used dedicated simulations [49, 54] to confirm that modifications to the *CP* properties of the Yukawa couplings between the Higgs and top and bottom quarks did not significantly influence either the signal acceptance or the distributions of discriminants used to extract

our results. We observed that such effects are typically at the $\mathcal{O}(1\%)$ level or smaller and are negligible compared to theoretical uncertainties on the signal modelling. Therefore, our measurement of $\alpha^{\mathrm{H}\tau\tau}$ is not sensitive to the assumptions made about the *CP*-nature of the production interactions.

The distributions of the Higgs boson's transverse momentum (p_{T}) and of the jet multiplicity are reweighted to match the predictions at next-to-NLO (NNLO) accuracy obtained from full phase space calculations with the POWHEG NNLOPS (version 1) generator [55, 56]. The decay of the H does not depend on its production. The description of the decay of the H to τ leptons is obtained using the PYTHIA generator version 8.230 [57]. These samples are simulated without accounting for the τ spin correlations. After the samples have been generated, the TAUSPINNER package [58] is used to calculate event weights that can be applied to the simulated signal samples to model τ polarisation effects for a boson with *CP*-mixing angles of 0, 45, and 90°. There is no normalisation effect from the reweighting procedure, i.e. the integrated H $\rightarrow \tau\tau$ cross section of the signal samples is invariant under rotations in $\alpha^{\mathrm{H}\tau\tau}$. All 2016 samples are generated with the NNPDF3.0 [59] NLO parton distribution functions (PDFs), while the NNPDF3.1 [60] NNLO distributions are used for 2017-2018.

The MADGRAPH5_AMC@NLO [61] generator (version 2.6.0) is used for processes involving a Z or W boson and up to four outgoing partons generated with the matrix element, and these processes are denoted Z + jets and W + jets, respectively. Processes involving W bosons originating from top quark decays are not considered in these samples. They are simulated at leading order (LO) with the MLM jet matching and merging approach [62]. The same generator is used at NLO for diboson production, whereas POWHEG 2.0 (1.0) is used for top quark-antiquark pair production [63] and single top quark production (associated with a W boson) [64, 65]. The generators are interfaced with PYTHIA to model the parton showering and fragmentation, as well as the decay of the τ leptons. The PYTHIA parameters that affect the description of the underlying event are set to the CUETP8M1 tune [66] in 2016, and CP5 tune [67] in 2017-2018.

Monte Carlo generated events are processed through a simulation of the CMS detector that is based on GEANT4 [68], and are reconstructed with the same algorithms as the ones used for data. Additional pp interactions per bunch crossing ("pileup") are included. The effect of pileup is taken into account by generating concurrent minimum bias collision events with PYTHIA. The pileup distribution in simulation is weighted to match the pileup in data.

5 Event reconstruction

The reconstruction algorithms for both observed and simulated events are based on the particle-flow (PF) algorithm [69], which relies on the information from the different CMS subdetectors to reconstruct muons, electrons, photons, and charged and neutral hadrons. These objects are combined to form more complex ones, such as τ_{h} candidates or missing transverse momentum ($p_{\mathrm{T}}^{\mathrm{miss}}$).

5.1 Primary vertex reconstruction

The positions of all pp interactions (vertices) in the event, including the hard scatter (primary) and soft (pileup) vertices, are reconstructed in a two-step procedure [70]. The steps consist in clustering the tracks that appear to originate from the same interaction using the deterministic annealing algorithm [71], and subsequently fitting the position of each vertex using tracks associated to its cluster with the adaptive vertex fitter (AVF) algorithm [72]. The candidate vertex with the largest value of the sum of the p_T^2 of all associated physics objects is considered to be the primary pp interaction vertex (PV). The physics objects included in this sum are jets, clustered using the anti-k_T jet finding algorithm [73] with the tracks assigned to candidate vertices as inputs, and the associated p_T^{miss}, taken as the negative vector sum of the p_T of those jets.

5.2 Muon reconstruction

Muons are identified and reconstructed with requirements on the quality of the track reconstruction and on the number of hits in the tracker and muon systems [74], and selected within $|\eta| < 2.4$. In order to reject muons that originate from nonprompt interactions, or are misidentified, a relative isolation is defined as

$$I^{\mu} \equiv \frac{\sum_{\text{charged}} p_T + \max\left(0, \sum_{\text{neutral}} p_T - \frac{1}{2} \sum_{\text{charged, PU}} p_T\right)}{p_T^{\mu}}. \tag{5.1}$$

In this equation, $\sum_{\text{charged}} p_T$ is the scalar p_T sum of the charged particles originating from the PV and located in a cone of size $\Delta R = \sqrt{(\Delta\eta)^2 + (\Delta\phi)^2} = 0.4$ (where ϕ is azimuthal angle in radians) centred on the muon direction. The sum $\sum_{\text{neutral}} p_T$ is a similar quantity for neutral particles. The $\sum_{\text{charged, PU}} p_T$ term sums over charged particles originating from pileup vertices in order to estimate and subtract the contribution of pileup to the neutral particle sum, which is scaled by $1/2$ to account for the fraction of neutral to charged energy in pileup interactions. The p_T of the muon is denoted by p_T^{μ}. In the $\tau_{\mu}\tau_h$ channel, it is required that $I^{\mu} < 0.15$.

5.3 Electron reconstruction

Electrons are reconstructed using tracks from the tracking system and calorimeter deposits in the ECAL, with a veto on objects with a large HCAL to ECAL energy ratio. Electrons are identified using a multivariate analysis (MVA) discriminant combining several quantities that describe the shape of the energy deposits in the ECAL, the quality of tracks, and the compatibility of the measurements from the tracker and the ECAL [75]. The energy scale of electrons is adjusted in data and simulation using the Z mass peak, while its resolution in simulation is adjusted to data.

For the electrons, an isolation criterion I^{e} is defined for a cone size of $R < 0.3$ centred on the electron direction. Its definition is analogous to eq. (5.1) for the charged tracks, but the pileup contribution of neutral particles is estimated via an effective-area method as

$$I^{\text{e}} = \frac{\sum_{\text{charged}} p_T + \max\left(0, \sum_{\text{neutral}} p_T - \rho\,\text{EA}\right)}{p_T^{\text{e}}}. \tag{5.2}$$

In this equation, the pileup contribution is estimated as $\rho\,\mathrm{EA}$, where ρ is the event-specific average pileup energy density per unit area in the ϕ-η plane and EA, which depends on the electron η, is the effective area specific to the neutral component of the isolation variable [75]. In the $\tau_{\mathrm{e}}\tau_{\mathrm{h}}$ channel, it is required that $I^{\mathrm{e}} < 0.15$.

5.4 Jet and $p_{\mathrm{T}}^{\mathrm{miss}}$ reconstruction

Jets are reconstructed using the anti-k_{T} algorithm [73] with distance parameter $R = 0.4$ as implemented in the FASTJET package [76]. The anti-k_{T} algorithm functions by taking PF objects and grouping them together based on inverse powers of the p_{T} of the objects [73, 77]. Jet momentum is determined as the vectorial sum of all particle momenta in the jet, and is found from simulation to be, on average, within 5 to 10% of the true momentum over the whole p_{T} spectrum and detector acceptance. Pileup interactions can contribute additional tracks and calorimetric energy depositions to the jet momentum. To mitigate this effect, charged particles identified to be originating from pileup vertices are discarded and an offset correction is applied to correct for remaining contributions. Jet energy corrections are derived from simulation to bring the measured response of jets to that of particle level jets on average. In situ measurements of the momentum balance in dijet, photon + jet, Z + jet, and multijet events are used to account for any residual differences in the jet energy scale between data and simulation [78]. The jet energy resolution amounts typically to 15-20% at 30 GeV, 10% at 100 GeV, and 5% at 1 TeV [78]. Additional selection criteria are applied to each jet to remove jets potentially dominated by anomalous contributions from various subdetector components or reconstruction failures. Data collected in the ECAL endcaps were affected by large amounts of noise during the 2017 data-taking period, which led to disagreements between simulation and data. To mitigate this issue, jets used in the analysis of the 2017 data are discarded if they have $p_{\mathrm{T}} < 50\,\mathrm{GeV}$ and $2.65 < |\eta| < 3.10$. Hadronic jets that contain b-quarks (b-jets) are tagged using a deep neural network (DNN), called DEEPCSV algorithm [79]. The medium working point used for the DEEPCSV algorithm corresponds to a b-jet identification efficiency of about 70% for a misidentification rate for jets originating from light quarks and gluons of around 1%.

The pileup per particle identification algorithm [80] is applied to reduce the pileup dependence of the $\vec{p}_{\mathrm{T}}^{\mathrm{miss}}$ observable. The $\vec{p}_{\mathrm{T}}^{\mathrm{miss}}$ and its magnitude ($p_{\mathrm{T}}^{\mathrm{miss}}$) are computed from the PF candidates weighted by their probability to originate from the PV [81]. The $\vec{p}_{\mathrm{T}}^{\mathrm{miss}}$ is adjusted for the effect of jet energy corrections.

5.5 Tau lepton reconstruction

The τ_{h} lepton reconstruction is performed with the Hadron-Plus-Strips (HPS) algorithm [82]. Starting from the constituents of reconstructed jets, the algorithm works by combining charged hadrons with the signature of neutral pions — one or more electron/photon candidates falling within a certain $\Delta\eta \times \Delta\phi$ region (referred to as a "strip"). The combination of these signatures provides the four-vector of the visible decay products of the parent τ_{h}. The identification of τ_{h} candidates makes use of isolation discriminators to reject quark and gluon jets that could be misidentified as τ_{h}. For this analysis, a DNN called DEEP-TAU [83] is used on the HPS τ_{h} candidates to provide further discrimination. In order

to achieve an optimal τ_h identification performance, the DNN combines information from the high-level reconstructed τ_h features together with the low-level information from the inner tracker, calorimeters and muon sub-detectors, using PF candidates reconstructed within the τ_h isolation cone. The working point on the output discriminant is chosen to provide a τ_h identification efficiency of about 60% at a jet misidentification rate of approximately 5×10^{-3}. Two other DNNs are used to reject electrons and muons misidentified as τ_h candidates using dedicated criteria based on the consistency between the measurements in the tracker, calorimeters, and muon detectors.

The mass of the $\tau\tau$ system $m_{\tau\tau}$ is calculated using a simplified matrix-element algorithm, SVFIT [84], which combines the $\vec{p}_T^{\,miss}$ and its uncertainty matrix with the four-vectors of both τ candidates to calculate the parent boson's mass. The resolution of $m_{\tau\tau}$ is 15-20% depending on the $\tau\tau$ final state and the boost of the $\tau\tau$ system.

6 Reconstruction of *CP*-sensitive observables

In this section we outline the methods used to construct *CP*-sensitive observables, collectively referred to as ϕ_{CP} angles. Various techniques can be used to define ϕ_{CP} depending on the decay topology of the τ leptons. In total, four methods are employed in the analysis: the "impact parameter" [85, 86], "neutral-pion" [86, 87], "combined" [86], and "polarimetric vector" [88] methods. We provide a detailed description of these methods below. We then summarise for which di-τ final states each method is utilised, and outline the procedures used to optimise the resolving power of the ϕ_{CP} observables.

6.1 Impact parameter method

This method exploits the finite lifetime of the τ leptons and can be applied to all events where both τ leptons decay to a single charged particle. We define the impact parameter $\vec{j}^{\pm}$ of a track (where $\pm$ refers to the charge of the track) as the vector between the PV and the point on the track where distance to the PV is minimal.

For each τ lepton we define a plane using the impact parameter vector and the charged-particle momentum vector. This plane, which is constructed in the laboratory frame, only represents the genuine plane of the decay into a single charged pion and neutrino when the laboratory frame coincides with the rest frame of the H. This means that this method does not reconstruct the genuine τ lepton decay plane, but rather a plane that is correlated with it. In order to approximate the rest frame of the H we use the charged decay products of the τ leptons of the H to define a zero-momentum frame (ZMF) into which the decay planes are boosted. The ZMF is used to define ϕ_{CP} for all channels in this analysis, except the $a_1^{3pr}a_1^{3pr}$ channel, where both τ leptons decay to three charged pions and the H rest frame can be reconstructed.

We then construct four-component vectors in the laboratory frame as $\lambda^{\pm} = (0, \vec{j}^{\pm})$. The $\lambda^{\pm}$ four-vectors are boosted into the ZMF and denoted $\lambda^{ZMF\pm}$. We also boost the respective charged-pion four-vectors to the ZMF, denoted $q^{ZMF\pm}$. Subsequently, we take the transverse components of $\lambda^{ZMF\pm}$ with respect to $q^{ZMF\pm}$. We normalise the vectors to obtain unit vectors $\hat{\lambda}_{\perp}^{ZMF+}$ and $\hat{\lambda}_{\perp}^{ZMF-}$.
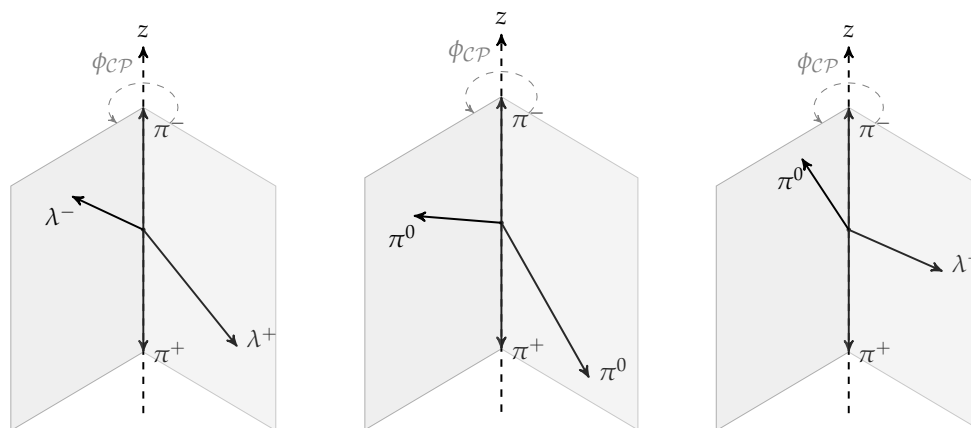
Figure 3. Illustration of the τ lepton decay planes and the angle ϕ_{CP} for various decay configurations. The decay planes are illustrated with the shaded regions, and either the vector $\hat{\lambda}$ or the momentum vector of the neutral pion is in the decay plane. The illustrations are in the frame in which the sum of the momenta of the charged particles is zero. Left: the decay plane for the decays $\tau^- \to \pi^- + \nu$ and $\tau^+ \to \pi^+ + \bar{\nu}$. Middle: the decay plane as reconstructed from the neutral and charged pion momenta. Right: ϕ_{CP} for the mixed scenario, in which one τ lepton decays to a pion while the other decays via an intermediate ρ meson.

To reconstruct ϕ_{CP}, we first define the angle ϕ^{ZMF} and O^{ZMF} as

$$
\begin{aligned}
\phi^{ZMF} &= \arccos(\hat{\lambda}_\perp^{ZMF+} \cdot \hat{\lambda}_\perp^{ZMF-}), \text{ and} \\
O^{ZMF} &= \hat{q}^{ZMF-} \cdot (\hat{\lambda}_\perp^{ZMF+} \times \hat{\lambda}_\perp^{ZMF-}).
\end{aligned}
\tag{6.1}
$$

From ϕ^{ZMF} and O^{ZMF} we reconstruct ϕ_{CP} in a range $[0, 360^\circ]$ as

$$
\phi_{CP} = \begin{cases} \phi^{ZMF} & \text{if } O^{ZMF} \geq 0 \\ 360^\circ - \phi^{ZMF} & \text{if } O^{ZMF} < 0 \end{cases}.
\tag{6.2}
$$

The τ lepton spectral functions have opposite signs for single-pion decays and leptonic decays in the kinematic regions considered in this analysis. This causes a phase flip between the ϕ_{CP} distributions for single pion decays and leptonic decays when the impact parameter method is used [40]. An illustration of the definition of the ϕ_{CP} observable using the impact parameter method is shown in figure 3 (left).

6.2 Neutral-pion method

This method can be applied to hadronic decay channels in which both τ leptons undergo decays involving more than one outgoing hadron. We describe the method applied to the intermediate ρ meson decay, and the intermediate $a_1(1260)$ meson to 1- and 3-prong decay modes.

For the ρ meson decays, the vector λ is replaced by the four-momentum vector of the π^0, which means we use the planes spanned by the ρ decay products (e.g. the $\pi^\pm$ and π^0
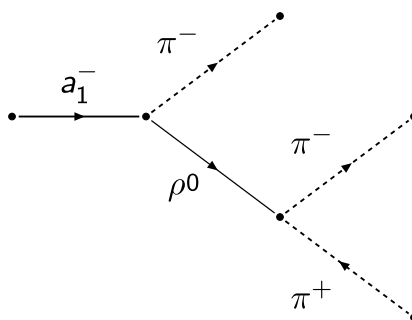
Figure 4. The decay of $a_1^{3\mathrm{pr}}$ via an intermediate ρ^0 to three charged pions.

in the case of the $\rho^\pm \to \pi^\pm\pi^0$ decay) to define the ϕ_{CP} observable. The four-momentum vector of the π^0 is obtained as follows: to estimate the π^0 energy, we sum the energies of all electron/photon candidates collected by the HPS algorithm. The direction of the π^0 is then taken as the direction of the leading electron/photon candidate. In most cases the leading candidate is a photon and the direction is determined by pointing its associated ECAL clusters back towards the PV. Finally, the mass is set to the known π^0 mass.

The same method is applied to $a_1^{1\mathrm{pr}}$ decays involving two neutral pions by summing the neutral constituents in the decay, as they cannot be easily resolved experimentally. The angle ϕ_{CP} is then calculated in an analogous method to that used in the impact parameter method except that to avoid destructive interference from differently polarised states of the mesons, the following observables need to be defined:

$$y^{\tau^\pm} = \frac{E_{\pi^\pm} - E_{\pi^0}}{E_{\pi^\pm} + E_{\pi^0}}, \; y^\tau = y^{\tau^-} y^{\tau^+}. \tag{6.3}$$

In this equation, E_π is the energy of the pion in the laboratory frame. If y^τ is negative, ϕ_{CP} is obtained via the shift $360^\circ - \phi_{CP}$. The neutral-pion method can also be successfully adapted to the $a_1^{3\mathrm{pr}}$ decay mode. In these decays we select the oppositely charged pion pair with an invariant mass closest to the intermediate ρ^0, an illustration is depicted in figure 4. Of this pair we treat the pion with the charge opposite of that of the τ_h lepton as though it was a π^0, and the momentum of the pion with the same sign as the τ_h is used for the calculation of the ZMF. After these assignments the neutral-pion method is applied as described for 1-prong decays.

An illustration of the definition of the ϕ_{CP} observable using the neutral-pion method is shown in figure 3 (middle).

6.3 Combined method

This method combines the impact parameter and neutral-pion methods outlined in the two previous sections, which is appropriate for events where only one of the two τ leptons

decay into multiple hadrons. For the τ lepton decaying into a ρ, a_1^{1pr}, or a_1^{3pr} mesons, the vector λ in eq. (6.1) is replaced by four-momentum vectors as described in section 6.2, and the angle ϕ_{CP} is then calculated using the same formulae.

Analogously to the neutral-pion method we avoid destructive interference from differently polarised states of the mesons by applying the shift $360^\circ - \phi_{CP}$ for events with $y^{\tau^\pm}$, where $y^{\tau^\pm}$ is computed for the τ lepton that decays to the intermediate resonance.

An illustration of the definition of the ϕ_{CP} observable using the combined method is shown in figure 3 (right).

6.4 Polarimetric vector method

This method can, in principle, be applied to any τ lepton decay mode in which both τ lepton momenta can be well reconstructed. When τ leptons decay via the a_1^{3pr} mode, the τ lepton rest frames can be reconstructed using the secondary vertices (SVs), that are extracted by fitting the three tracks originating from the a_1^{3pr} decays. Therefore, we only apply the polarimetric vector method to the $a_1^{3pr}a_1^{3pr}$ decay configuration.

The polarimetric vector $\vec{h}$ can be considered as an estimate of the most likely direction of the spin vector $\vec{s}$ of the τ lepton in the τ lepton rest frame [88]. We start by outlining the reconstruction of the τ lepton momenta, which are required to compute the polarimetric vectors. Subsequently, we describe how ϕ_{CP} is reconstructed in the H rest frame from both the τ lepton momenta and the polarimetric vectors.

To reconstruct the τ lepton momentum in the a_1^{3pr} channel we assume that the reconstructed τ lepton candidate has a mass m_τ and undergoes a two-body decay to a massless neutrino and an intermediate a_1 meson with mass m_{a_1}. Furthermore, we define the Gottfried-Jackson angle θ_{GJ} as the angle between the a_1 momentum and the τ lepton momentum [89]. The latter is reconstructed from the positions of the τ lepton production and decay vertex. The magnitude of the τ lepton momentum is then given by [89]

$$|\vec{p}_\tau| = \frac{(m_{a_1}^2 + m_\tau^2)|\vec{p}_{a_1}|\cos\theta_{GJ} \pm \sqrt{(m_{a_1}^2 + |\vec{p}_{a_1}|^2)((m_{a_1}^2 - m_\tau^2)^2 - 4m_\tau^2|\vec{p}_{a_1}|^2\sin^2\theta_{GJ})}}{2(m_{a_1}^2 + |\vec{p}_{a_1}|^2\sin^2\theta_{GJ})}.$$

(6.4)

The maximal allowed value θ_{GJ}^{max} of the Gottfried-Jackson angle is defined as

$$\theta_{GJ}^{max} = \arcsin\left(\frac{m_\tau^2 - m_{a_1}^2}{2m_\tau|\vec{p}_{a_1}|}\right).$$

(6.5)

For decays in which the reconstructed θ_{GJ} exceeds θ_{GJ}^{max}, due to the finite angular resolution of the charged pions and τ direction measurements, the value of θ_{GJ} is set to θ_{GJ}^{max}.

As can be seen in eq. (6.4), there can be two solutions for the τ lepton momentum. This can be understood by considering the decay in the τ lepton rest frame. In this frame, the a_1 meson may be emitted in either the same or the opposite direction to that of the τ lepton momentum in the lab frame. When the a_1 meson is emitted in the direction orthogonal to the τ lepton, we obtain the uniquely determined solution when the square root in the numerator of eq. (6.4) vanishes. Thus, we may obtain up to four pairs of solutions for the

momenta of the two τ leptons. This ambiguity is resolved by selecting the pair of solutions with the mass closest to that of the H. The direction of the τ lepton in the lab frame is determined by the vector SV−PV.

Once the τ leptons and a_1^{3pr} momenta have been determined, the polarimetric vectors $\vec{h}_{1,2}$ may be retrieved using the a_1^{3pr} resonance model as implemented in the TAUOLA [90–92] program, which uses the parameters as measured by the CLEO Collaboration [93]. To reconstruct ϕ_{CP} from the polarimetric vectors and the τ lepton momenta vectors, we introduce a vector $\vec{k}$ that is defined as

$$\vec{k}_{1,2} = \frac{\vec{h}_{1,2} \times \vec{n}_{1,2}}{|\vec{h}_{1,2} \times \vec{n}_{1,2}|}. \tag{6.6}$$

In this definition, $\vec{n}_{1,2}$ are the two τ lepton momentum unit vectors in the H rest frame. We then reconstruct ϕ^* and O^* (in the H rest frame) as

$$\begin{aligned} \phi^* &= \arccos(\vec{k}_1 \cdot \vec{k}_2), \text{ and} \\ O^* &= -(\vec{h}_1 \times \vec{h}_2) \cdot \vec{n}_1. \end{aligned} \tag{6.7}$$

From ϕ^* and O^* we reconstruct ϕ_{CP} via the assignments defined in eq. (6.2).

In summary, for the configuration involving two a_1^{3pr} decays, the secondary decay vertices are exploited to reconstruct the τ momenta in the rest frame of the H. Together with the a_1 resonance model, this allows for the extraction of the polarimetric vectors. Studies on simulated signal events revealed that fits to ϕ_{CP} measured using the polarimetric vector method have approximately twice the resolving power between the *CP*-even and *CP*-odd states as compared to applying the neutral-pion method.

6.5 Strategy for selecting the *CP*-sensitive observables

The τ_h impact parameter is relatively small compared to the tracking resolution and therefore the precision to which it can be measured is limited despite the excellent resolution of the CMS tracker. An advantage of the neutral-pion method is that it does not rely on the reconstruction of the impact parameter; instead, the direction of the neutral pion needs to be determined. Due to the relatively large distance between the primary interaction point and the ECAL ($\mathcal{O}(1\,\mathrm{m})$), coupled with the fine ECAL granularity, the direction of neutral pions can be reconstructed with smaller relative uncertainties compared to the impact parameter direction.

Studies were performed on signal events to review the *CP* sensitivity of the neutral pion and impact parameter methods in regions of phase space where the latter is expected to perform optimally. The sensitivity normalised to the number of events was comparable while the selections (explained below) that are needed for the impact parameter method discard a significant number of events. The cuts imposed on the impact parameter significance mean that the neutral-pion method can be applied to about twice as many events as the impact parameter method. Therefore, although the impact parameter method can in principle be applied to every τ lepton decay mode, in this analysis we only use this method for the ππ, μπ, and eπ final states. For the ρρ, ρa_1^{1pr}, $a_1^{1pr}a_1^{1pr}$, $a_1^{1pr}a_1^{3pr}$, and ρa_1^{3pr} final

states, the neutral-pion method is deployed, and the polarimetric vector method is used exclusively for the $a_1^{3pr}a_1^{3pr}$ channel. In other configurations where one τ lepton decays to a single charged hadron or lepton and the other to multiple hadrons, the combined methods is used.

6.6 Extraction of ϕ_{CP} optimisation

In this section we outline the experimental techniques that are developed for this analysis to optimise the experimental extraction of ϕ_{CP}. A dedicated MVA discriminant is deployed to improve the identification of the τ_h decay modes. To improve the estimate of the impact parameters, the reconstruction of the PV coordinates is improved, and a helical extrapolation of the track to the PV was implemented. These methods are discussed in detail below.

6.6.1 Multivariate discriminant for τ_h decay mode identification

In order to optimally discriminate between the different decay modes, a boosted decision tree (BDT) [94] is deployed. It is trained using the XGBOOST [95] framework, and is applied on top of the τ_h selection. The algorithm was trained to distinguish between the 1- and 3-prong τ lepton decays: π, ρ, a_1^{1pr}, a_1^{3pr}, and $\pi^{\pm}\pi^{\mp}\pi^{\pm}\pi^0$. The $\pi^{\pm}\pi^{\mp}\pi^{\pm}\pi^0$ decay is not used in the extraction of the CP angle but must be separated from a_1^{3pr} to avoid contamination.

The inputs to the BDT are the kinematic features of the τ_h reconstructed by the HPS method and its constituents. The BDT exploits angular correlations between the decay products, invariant mass quantities, and kinematic properties of the photons.

6.6.2 Primary vertex refitting

The finite lifetime of the τ lepton means that tracks emanating from its decay do not originate from the PV. These tracks are removed and the PV is refitted using the remaining tracks as input to the AVF algorithm. The LHC beamspot represents a three-dimensional (3-D) profile of the luminous region, where the LHC beams collide in the CMS detector. The parameters of the beamspot are determined from an average over many events [70]. The uncertainties in the beamspot parameters are relatively small and are incorporated into the AVF algorithm to provide an additional constraint on the PV position. The inclusion of the beamspot information leads to an improvement of the PV resolution in the transverse plane of a factor of about 3 for signal events and of about 4 for Drell-Yan events, while the z coordinate of the PV is largely unaffected. This refitted PV is used when estimating the impact parameters and the polarimetric vectors.

6.6.3 Impact parameter estimate and significance

A dedicated algorithm is deployed to derive the impact parameter of the charged track from the τ lepton decay using an analytic extrapolation of track trajectory towards the PV position. The extrapolation depends on the magnetic field and the helical parameters of the track. The distance between the extrapolated track and the PV position is then minimised numerically to determine the impact parameter.

Channel	Year	Trigger requirement	Offline p_T (GeV)
$\tau_h\tau_h$	All years	$\tau_h(35)\,\&\,\tau_h(35)$	$p_T^{\tau_h} > 40$
$\tau_\mu\tau_h$	2016	$\mu(22),\,\mu(19)\,\&\,\tau_h(20)$	$p_T^\mu > 20,\ p_T^{\tau_h} > 25$
	2017, 2018	$\mu(24),\,\mu(20)\,\&\,\tau_h(27)$	$p_T^\mu > 21,\ p_T^{\tau_h} > 32$
$\tau_e\tau_h$	2016	$e(25)$	$p_T^e > 26$
	2017	$e(27),\,e(24)\,\&\,\tau_h(30)$	$p_T^e > 25,\ p_T^{\tau_h} > 35$
	2018	$e(32),\,e(24)\,\&\,\tau_h(30)$	$p_T^e > 25,\ p_T^{\tau_h} > 35$

Table 2. Kinematic trigger and offline requirements applied to the $\tau_e\tau_h$, $\tau_\mu\tau_h$, and $\tau_h\tau_h$ channels. The trigger p_T requirement is indicated in parentheses (in GeV). The p_T thresholds indicated for the τ_h apply only for the object matched to the hadronic trigger or to the hadronic leg from the cross trigger.

This procedure has two advantages. Firstly, with this extrapolation, the minimisation of the impact parameter is performed in three dimensions. For tracks with large η values, the procedure leads to a better estimation of the z coordinate of the impact parameter than when the minimisation is done exclusively in the transverse plane. Secondly, the helical extrapolation allows for the propagation of both the track and PV uncertainties into an overall impact parameter significance S_{IP} (defined as the ratio of the magnitude of the impact parameter divided by its uncertainty). In this analysis, selections are made on the impact parameter significance, as further explained in section 9.

7 Event selection

Events are selected online by the CMS trigger system. For the $\tau_\ell\tau_h$ channels, events are triggered by either a paired $\ell + \tau_h$ cross trigger or a single-lepton trigger with a higher p_T threshold for the lepton compared to the cross trigger. For the $\tau_h\tau_h$ channel, a di-τ trigger is used.

Offline, a pair of oppositely charged τ leptons separated by $\Delta R > 0.5$ is required. The offline-reconstructed objects must match the required trigger objects (i.e. the object as reconstructed by the trigger system) within $\Delta R < 0.5$. The offline-reconstructed light lepton is required to have a p_T value that is at least 1 GeV higher than the online threshold. If an offline τ_h candidate is matched to a τ_h trigger object (including the τ_h leg of the $\ell + \tau_h$ cross trigger for the semileptonic channels), the τ_h must have a p_T at least 5 GeV above the trigger threshold. The offline thresholds are higher than the online thresholds due to the turn-on curve in the trigger efficiencies.

Table 2 summarises the online trigger and offline p_T thresholds for 2016–2018. The offline requirements apply only to objects that are matched to a trigger object. If, in the $\tau_\ell\tau_h$ channels, the event is selected online by the single-lepton trigger, the offline τ_h is required instead to have a p_T of at least 20 GeV.

For the $\tau_\ell\tau_h$ channels, the large W + jets background is reduced by rejecting events based on the transverse mass m_T of the light lepton and $\vec{p}_T^{\,\text{miss}}$ system,

$$m_T \equiv \sqrt{2p_T^\ell p_T^{\text{miss}}[1 - \cos(\Delta\phi)]} < 50\,\text{GeV}, \tag{7.1}$$

where $\Delta\phi$ is the azimuthal angle between the direction of the light lepton and $\vec{p}_T^{\,\text{miss}}$.

The longitudinal and transverse impact parameters d_z and d_{xy} of the muon and electron are required to satisfy $|d_z| < 0.2\,\text{cm}$ and $|d_{xy}| < 0.045\,\text{cm}$. These impact parameters originate from a minimisation of the magnitude of the impact parameters in the transverse plane only, in contrast to the impact parameters used for calculating ϕ_{CP}, which are derived using a 3-D minimisation. For the purpose of the event selection this factorised approach is sufficiently precise. For the leading τ_h track, only the requirement $|d_z| < 0.2\,\text{cm}$ is imposed to avoid loss of selection efficiency. Further, a veto on events containing loosely identified additional electrons or muons is imposed. For the $\tau_\ell\tau_h$ channels, a veto on jets passing b-tagging requirements is also applied. When multiple τ lepton pairs are present, the pairs are ranked based on the output scores of the DEEPTAU algorithm for the τ_h candidates, and the relative isolation for the τ_ℓ candidates. The highest ranked pair is selected.

8 Background estimation

The processes that contribute to the background in this analysis are Z + jets, W + jets, top quark-antiquark pair production ($t\bar{t}$), single top quark, and diboson production. Additionally, events comprised uniquely of jets produced through the strong interaction, referred to as QCD multijet events, form a significant background. These processes contribute to the production of genuine τ leptons, jets and leptons that are misidentified as τ_h, as well as prompt leptons and jets that are misidentified as τ_ℓ in the semileptonic channels. All background processes resulting in two genuine τ leptons constitute a major background, and are estimated from data using a τ-embedding technique [96]. The majority of the backgrounds due to jets misidentified as τ_h candidates are estimated using the "fake factor" (F_F) method, as described in ref. [97]. The remaining minor backgrounds are determined using simulated events. In the remainder of this section we outline the τ-embedding and F_F methods, and describe the corrections applied to simulated events in order to improve their description of the data.

8.1 The τ embedding method

In order to obtain the genuine $\tau\tau$ background we exploit lepton universality, and replace oppositely charged muon pairs in data events with simulated oppositely charged τ lepton pairs. The dominant process for this background is Z $\rightarrow$ $\tau\tau$, but there are also small contributions from $t\bar{t}$ and diboson processes.

For all data-taking periods, events containing an oppositely charged dimuon pair were collected using a dedicated di-μ trigger. The detector hits belonging to the muon tracks are removed from these events. A Z boson is simulated in an empty detector, which is forced to decay to a pair of oppositely charged τ leptons with identical kinematics to the muon pair

that was removed. The τ leptons are forced to decay fully hadronically or semileptonically in order to simulate either the $\tau_h\tau_h$ or $\tau_\ell\tau_h$ channels. The detector response to the τ pair is then simulated and added to the data event.

In order to model the background processes in data well, various corrections need to be applied to the embedded event samples. Muons and electrons are corrected for mismodelling of their trigger, tracking and identification, and isolation requirements efficiencies. The τ_h candidates are corrected for mismodelling of their trigger, reconstruction and identification efficiencies. The "tag-and-probe" method [98] is used to derive these corrections. The τ_h energy scales are corrected per decay mode to match the corresponding scales in data. The electron, muon, and pion impact parameters are corrected using a samples of $Z \to \mu\mu$ and $Z \to ee$ events and quantile-mapping techniques.

8.2 The F_F method

This method is designed to provide an estimate of the shape and normalisation of events in which at least one quark or gluon jet is misidentified as a τ_h lepton based on control samples in data. We refer to such a jet as a jet $\to \tau_h$.

We define a determination region that is orthogonal to the signal region and dominated by a background process resulting in jet $\to \tau_h$ misidentifications; the construction of these regions is outlined below. We define a τ_h nominal ID as a τ_h object that passes nominal ID requirements as outlined in section 5, and a relaxed τ_h ID as objects that pass a looser requirement on the DNN output but fail the nominal ID. In this determination region we obtain the ratio between the nominal ID τ_h rate and the relaxed ID τ_h rate. The ratio in the determination region is the F_F. To obtain the rate of misidentified jets in the signal region, an application region is defined by selecting events that fulfil all event selection criteria except that they contain a τ_h lepton that passes the relaxed instead of the nominal requirement (for the $\tau_h\tau_h$ channel it must be the leading τ_h). The rate of misidentified jet events in the signal region is obtained by applying the F_F values from the determination region on an event-by-event basis as an event weight to the events in the application region. In both determination and application regions the contribution of other background processes not involving jet $\to \tau_h$ events, which amounts to about 1% (5%) in the $\tau_h\tau_h$ ($\tau_\ell\tau_h$) channel(s), is subtracted using simulated events. The contamination from signal events is significantly smaller (<0.1%) and is therefore neglected.

The jet $\to \tau_h$ background in the $\tau_h\tau_h$ channel originates almost entirely from QCD multijet events. The determination region is thus defined by inverting the opposite-sign requirement on the τ lepton pair to a same-sign requirement, which effectively selects a control region pure in QCD jets. The F_F are parameterised for the leading τ_h lepton as a function of the p_T of the τ_h, and binned in the reconstructed decay mode, jet multiplicity, and impact parameter significance. Correction factors are derived using control regions in data to correct for residual differences in the $\vec{p}_T^{\text{miss}}$ spectrum, and to account for the sign inversion used to define the determination region. The final F_F value for the τ_h channel is obtained by applying the raw F_F and the two corrections multiplicatively. This F_F also accounts for other processes with a jet misidentified as the leading τ_h lepton, such as W + jets production. The events in which the subleading τ_h is a misidentified jet and

the leading τ_{h} candidate is a genuine τ lepton are modelled via simulation; these events constitute only a small fraction ($\mathcal{O}(2\%)$) of the total misidentified jet background in the $\tau_{\mathrm{h}}\tau_{\mathrm{h}}$ channel.

In the $\tau_{\ell}\tau_{\mathrm{h}}$ channels, the W + jets process, and to a lesser extent the $\mathrm{t\bar{t}}$ process, contribute to jet misidentification as well as events originating from QCD multijet production. Therefore, separate F_{F} are derived for these processes, and these individual F_{F} values are subsequently weighted into an overall F_{F} to account for their different contributions in the application region. Simulated events are used to determine the expected relative contributions of W + jets and $\mathrm{t\bar{t}}$ events, and the QCD contribution is estimated by subtracting all simulated non-QCD processes from the data in the application region. In order to account for dependencies of the weights on several kinematic variables, a multi-class BDT is trained to separate W + jets, QCD, and $\mathrm{t\bar{t}}$ events. The inputs to the BDT include kinematic features of the reconstructed $\tau\tau$ system and the associated jets, as well as the τ_{h} decay mode. The output of the BDT is a set of three scores (one per class) that sum to unity — meaning one of the outputs is redundant. The weights are thus determined in bins of two of these scores. The overall F_{F} accounts for the jet misidentification in all background processes. The procedure for the QCD F_{F} is similar to the method described for the $\tau_{\mathrm{h}}\tau_{\mathrm{h}}$ channel, except that the light lepton isolation parameter must be larger than 0.05 to reduce processes resulting in genuine leptons. Correction factors are derived to correct for residual differences in the lepton p_{T} and $\vec{p}_{\mathrm{T}}^{\,\mathrm{miss}}$ spectra, and to account for the sign inversion and additional lepton isolation requirement used to define the determination region. A determination region sufficiently pure in W + jets is defined by selecting events with $m_{\mathrm{T}} > 70\,\mathrm{GeV}$. Correction factors are derived to correct for residual differences in the lepton p_{T} and $\vec{p}_{\mathrm{T}}^{\,\mathrm{miss}}$ spectra, and to account for the inverted m_{T} selection used to define the determination region. For the $\mathrm{t\bar{t}}$ process, it is difficult to define a sufficiently pure region in data, and thus the F_{F} values are estimated from a simulated $\mathrm{t\bar{t}}$ sample. Correction factors are derived to correct for residual differences in the $\vec{p}_{\mathrm{T}}^{\,\mathrm{miss}}$ spectrum, and to account for differences in the F_{F} in data and simulation. The latter is derived by comparing the F_{F} values measured for W + jets in data and simulation.

8.3 Estimation of minor backgrounds

The τ-embedding and F_{F} methods combined describe around 90% of the backgrounds in this analysis. All events containing a genuine τ lepton pair are taken from the embedded samples, while events in which the (leading) τ_{h} is a misidentified hadronic jet in the ($\tau_{\mathrm{h}}\tau_{\mathrm{h}}$) $\tau_{\ell}\tau_{\mathrm{h}}$ channels are obtained from data using the F_{F} method. All other background events are obtained from simulation.

In addition to the genuine τ and $\mathrm{jet} \to \tau_{\mathrm{h}}$ contributions to the selected pairs, there are additional sources of τ misidentifications that may occur. This includes prompt leptons that may be either misidentified as a τ_{ℓ} or as a τ_{h}, τ_{ℓ} leptons being misidentified as τ_{h}, and jets misidentified as τ_{ℓ} candidates. In tables 3 and 4 we summarise the different background composition configurations and their modelling for the $\tau_{\mathrm{h}}\tau_{\mathrm{h}}$ and $\tau_{\ell}\tau_{\mathrm{h}}$ channels, respectively. To avoid double-counting events with a genuine τ lepton pair, such events are subtracted

Leading τ_h	Subleading τ_h		
	Genuine τ_h	Jet $\to \tau_h$	(Prompt lepton/τ_ℓ) $\to \tau_h$
Genuine τ_h	τ-Embedding	Simulation	Simulation
Jet $\to \tau_h$	F_F	F_F	F_F
(Prompt lepton/τ_ℓ) $\to \tau_h$	Simulation	Simulation	Simulation

Table 3. The different sources of backgrounds in the $\tau_h\tau_h$ channel are shown in the rows and columns. The entries in the table represent the possible τ lepton pair background contribution from different processes and misidentifications and encapsulate the different experimental techniques that are deployed to estimate the background contributions.

τ_ℓ	τ_h		
	Genuine τ_h	Jet $\to \tau_h$	(Prompt lepton/τ_ℓ) $\to \tau_h$
Genuine τ_ℓ	τ-Embedding	F_F	Simulation
Jet $\to \tau_\ell$	Simulation	F_F	Simulation
Prompt lepton $\to \tau_\ell$	Simulation	F_F	Simulation

Table 4. The different sources of backgrounds in the $\tau_\ell\tau_h$ channel are shown in the rows and columns. The entries in the table represent the possible τ lepton pair background contribution from different processes and misidentifications and encapsulate the different experimental techniques that are deployed to estimate the background contributions.

from all simulated samples, as well as events in which the τ_h is a misidentified hadronic jet (for the $\tau_h\tau_h$ channel this must be the leading τ_h).

In order to model the background processes in data well, various corrections need to be applied to the simulated samples. All corrections to the τ lepton decay products applied to the embedded samples (described in section 8.1) are also applied to the simulated samples. Although both embedded and simulated samples include simulated leptons, the corresponding corrections can differ slightly due to deposits from other nearby objects, that may influence, for example, isolation sums and/or particle identification decisions. Therefore, dedicated correction factors are derived in each case.

Jet energy scale corrections are applied to both data and simulated events as described in section 5. Recoil corrections to the $\vec{p}_T^{\text{miss}}$ are applied to reduce the mismodelling of the simulated $Z + $ jets, $W + $ jets, and Higgs boson samples. The corrections are applied to the simulated events based on the vectorial difference of the measured p_T^{miss} and total p_T of the neutrinos originating from the decay of the Z, W, or H. Their average effect is the reduction of the p_T^{miss} obtained from simulation by a few GeV. Recoil corrections to $\vec{p}_T^{\text{miss}}$ are measured in $Z \to \mu\mu$ events. The corrections are subsequently applied to Drell-Yan plus jets events, $W + $ jets, and signal event samples. The $\ell \to \tau_h$ misidentification rates are corrected in simulation by applying the tag-and-probe method to $Z \to \ell\ell$ events, and the energy scales are corrected in simulation to match the scale in data.

The Z boson mass and p_T spectra in simulation are corrected to better match the data. To this purpose the Z mass and p_T are measured in data and simulation in di-muon events, and the simulated events are corrected to match the spectra in data. A correction

is also applied to the top quark p_{T} spectrum in the $\mathrm{t\bar{t}}$ sample, using a dedicated control region. The procedure used to derive this correction is detailed in ref. [99].

After applying all corrections, we obtain a satisfactory description of the observables that we use to categorise events, which are described in section 9.

8.4 Validating the modelling of the ϕ_{CP} observables

To validate the modelling of the ϕ_{CP} spectrum, the $\tau_{\mu}\tau_{\mathrm{h}}$ events in data and the background estimates are divided into distributions in which the charged π is "nearly coplanar" or "nearly perpendicular" to the production plane of the beam axis and the τ momentum in the laboratory frame, as described in ref. [37]. To this purpose we introduce the observable α_{-}^{π} that is defined as

$$\cos\alpha_{-}^{\pi} = \left| \frac{\hat{z} \times \hat{p}}{|\hat{z} \times \hat{p}|} \cdot \frac{\hat{j} \times \hat{p}}{|\hat{j} \times \hat{p}|} \right|. \tag{8.1}$$

In this equation, $\hat{z}$ is the unit vector pointing along the beam axis, $\hat{p}$ is the unit momentum vector of the charged π, and $\hat{j}$ is the unit impact parameter vector. We can define a subset of events in which the charged π is nearly perpendicular or coplanar by requiring $\alpha_{-}^{\pi} > \pi/4$ or $\alpha_{-}^{\pi} < \pi/4$, respectively. We also perform equivalent checks for τ decays into ρ mesons, where we substitute the unit π^0 momentum vector for $\hat{j}$ in eq. (8.1) to define an equivalent observable, α_{-}^{ρ}. In figure 5 we display the coplanar and perpendicular distributions in the $\mu\pi$ and $\mu\rho$ channels.

9 Event categorisation

In order to enhance the sensitivity of this analysis we apply MVA discriminants to separate signal from background events.

This event categorisation is formulated as a multi-class problem. The output is a set of scores for each event (one per class) that, by construction, sum to unity. Each score can therefore be interpreted loosely as the probability that an event belongs to a given class. We then assign each event to a category depending on the class that received the highest score. Since both the $\tau_{\ell}\tau_{\mathrm{h}}$ and $\tau_{\mathrm{h}}\tau_{\mathrm{h}}$ channels are dominated by backgrounds containing contributions from genuine τ and jet $\to \tau_{\mathrm{h}}$ production, the discriminant is trained to categorise events in three classes:

- The "Higgs" category is trained to distinguish events from the ggH, VBF, and VH samples from background events, which are reweighed by their cross sections before merging them into one sample. Events in this category are used to infer the *CP* quantum number of the boson.

- The "Genuine" category includes all background processes involving two genuine τ leptons.

- The "Mis-ID" category includes all background processes in which minimally one hadronic jet is misidentified as a τ_{h} lepton. This category also contains $\ell \to \tau_{\mathrm{h}}$ misidentified events for all channels and prompt light leptons in the $\tau_{\ell}\tau_{\mathrm{h}}$ channels.
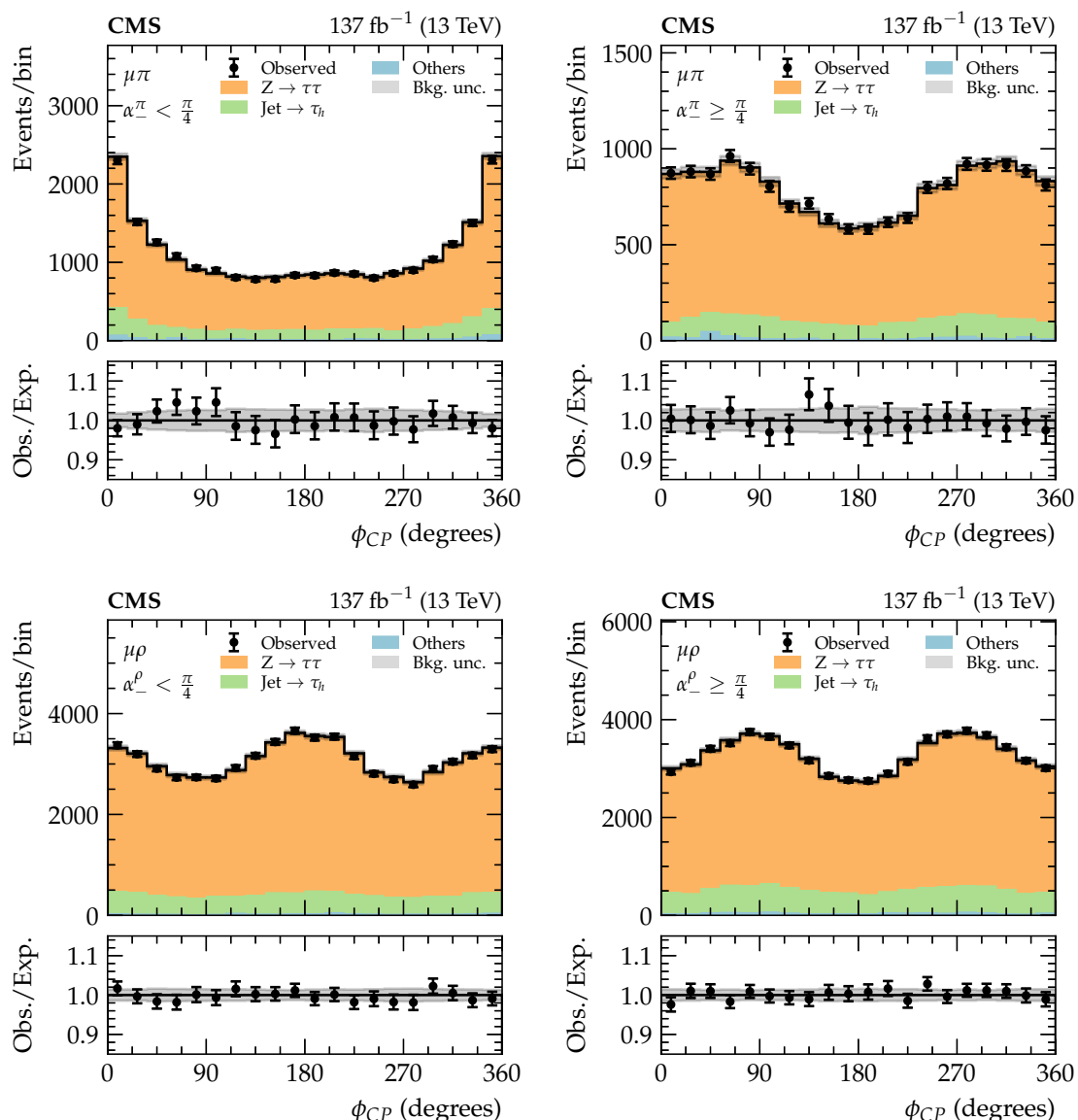
Figure 5. The angle ϕ_{CP} for $\tau_\mu\tau_h$ events in which the τ_h decays to a charged π (upper) or a charged ρ meson (lower). The distributions are decomposed in a subset in which the charged π is "nearly coplanar" (left) or "nearly perpendicular" (right) to the production plane.

The three categories are mutually exclusive and, by definition, the lower bound for the highest MVA score is 1/3. Subsequently, the three training categories are normalised to account for the different number of events in each data set. All event classes are then chosen to contribute to the training with the same weight, i.e. with uniform prevalence. For the semileptonic channels, the backgrounds for the training are provided from simulated samples, except for QCD events, which are obtained using same-sign τ lepton pair candidates in data. For the hadronic channel, the embedded samples and the F_F method are used in the training. For the latter, the events from the application region are used and reweighted

Observable	$\tau_\ell\tau_h$	$\tau_h\tau_h$
p_T of leading τ_h	✓	✓
p_T of trailing τ_h	—	✓
p_T of τ_ℓ	✓	—
p_T of visible di-τ	✓	✓
p_T of di-$\tau_h + p_T^{miss}$	—	✓
p_T of $\tau_\ell\tau_h + p_T^{miss}$	✓	—
Visible di-τ mass	✓	✓
Di-τ mass (using SVFIT)	✓	✓
Leading jet p_T	✓	✓
Trailing jet p_T	✓	
Jet multiplicity	✓	✓
Dijet invariant mass	✓	✓
Dijet p_T	✓	
Dijet $|\Delta\eta|$	✓	
p_T^{miss}	✓	✓

Table 5. Input variables to the MVA discriminants for the $\tau_\ell\tau_h$ and $\tau_h\tau_h$ channels. The SVFIT algorithm is used to estimate the di-τ mass.

by their F_F values. The contribution of other background processes not involving jet $\to \tau_h$ events is not removed in this case, but the impact of these events on the performance of the MVA is negligible as they amount to only $\mathcal{O}(1\%)$ of the total. A separate training was performed for each year to account for differences in the performance of the CMS detector in different data-taking periods. In the $\tau_\ell\tau_h$ channels, the event categorisation is performed with a multiclass neural network. In the $\tau_h\tau_h$ channel, the event categorisation is performed using a multi-class BDT algorithm combined with the XGBOOST package. The input variables used in the categorisation of the $\tau_\ell\tau_h$ and $\tau_h\tau_h$ channels are displayed in table 5. The training is performed inclusively for all the τ lepton decay modes.

Events are sorted into the three categories depending on which of the three output scores is closest to unity. The maximum output score is also retained and used for the purpose of signal extraction. These maximum scores will be referred to as the "MVA scores" henceforth.

After the categorisation, a cutoff of $S_{IP} > 1.5$ is applied to the impact parameter significances of the electron and muon, as well as to the single pions from a τ lepton for events that are classified as signal events. Events with a lower S_{IP} would dilute the sensitivity of the analysis. In the background categories, a cutoff on the impact parameter significance is only applied to the single-pion decays.

In figure 6, the post-fit MVA score distributions of the Genuine and Mis-ID categories are displayed for the $\tau_\mu\tau_h$ and $\tau_e\tau_h$ channels. The best fit signal contributions are overlaid. The fitting procedure is outlined in section 12. The genuine di-τ and jet $\to \tau_h$ background contributions are displayed separately as indicated in the legends. The remaining background contributions are collated and indicated by the "Others" label. The BDT scores for the $\tau_h\tau_h$ channel are analogously displayed in figure 7.
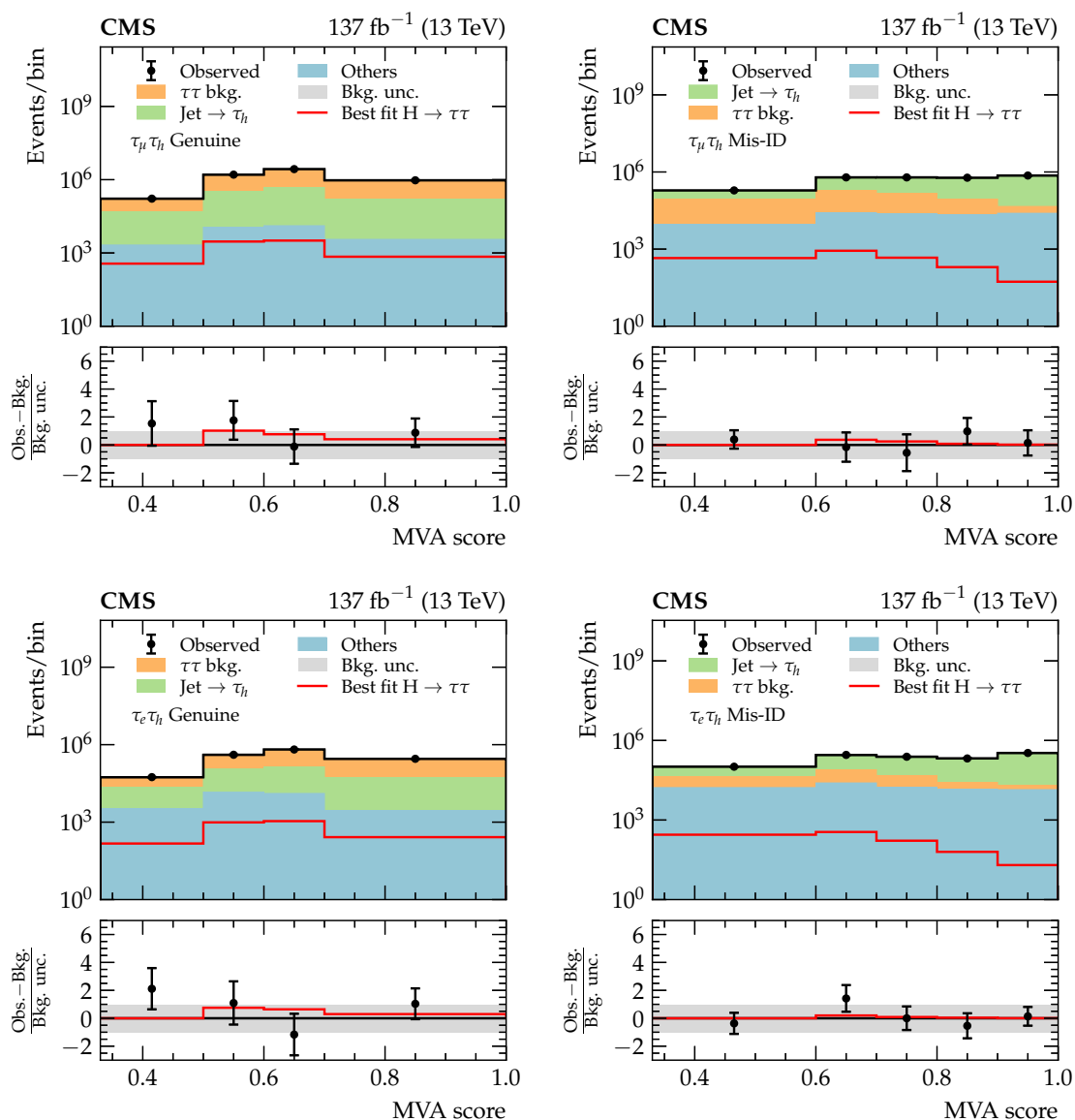
Figure 6. The post-fit MVA score distributions for the Genuine (left) and Mis-ID categories (right) in the $\tau_\mu\tau_h$ (upper) and $\tau_e\tau_h$ (lower) channels. The distributions are inclusive in τ_h decay mode. The best fit signal distributions are overlaid, where the signal cross sections are set to the values obtained from the fit to data, which are given in section 12.1. In the lower panels, the data minus the background template divided by the uncertainty in the background template is displayed, as well as the signal distribution divided by the uncertainty in the background template. The uncertainty band accounts for all sources of systematic uncertainty in the background prediction, after the fit to data.
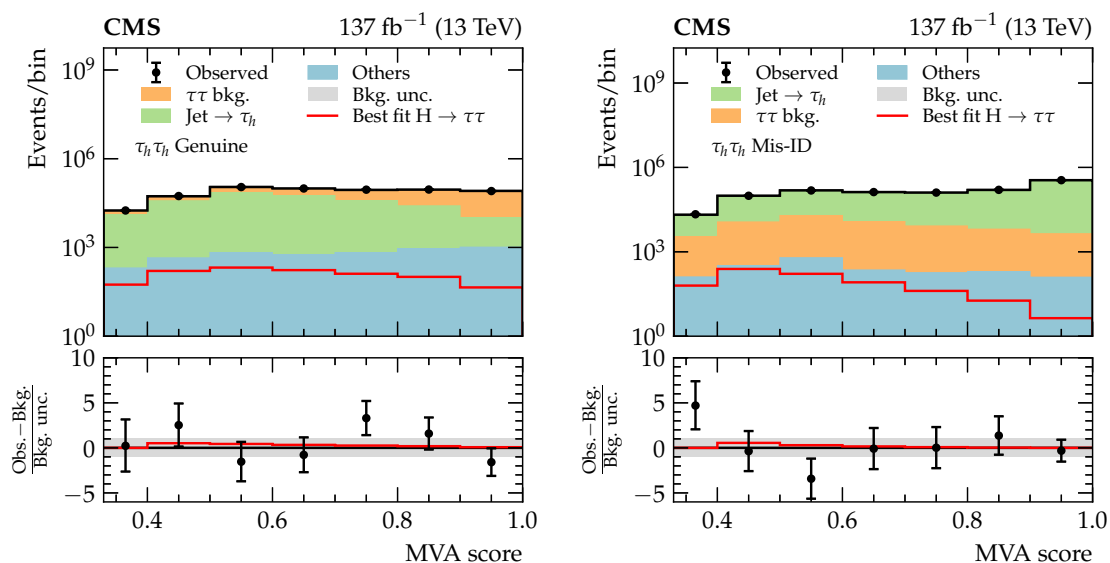
Figure 7. The post-fit MVA score distributions for the Genuine (left) and Mis-ID categories (right) in the $\tau_h\tau_h$ channel. The distributions are inclusive in τ_h decay mode. The best fit signal distributions are overlaid, where the signal cross sections are set to the values obtained from the fit to data, which are given in section 12.1. In the lower panels, the data minus the background template divided by the uncertainty in the background template is displayed, as well as the signal distribution divided by the uncertainty in the background template. The uncertainty band accounts for all sources of systematic uncertainty in the background prediction, after the fit to data.

10 The ϕ_{CP} distributions in windows of the MVA discriminant score

The MVA score distributions described in section 9 allow for a partial separation of signal from background events. The ϕ_{CP} distributions of the events in the signal categories are then analysed in windows of increasing MVA score, corresponding to progressively higher signal-to-background ratios. The result is a set of 2-D distributions built from the MVA score and ϕ_{CP} variables. These distributions are used in the fit to data to extract the results.

The statistical fluctuations in the estimates of the background contributions (denoted as background templates) in the signal and background categories are sizeable. It has been underlined that backgrounds involving two genuine τ leptons are flat in ϕ_{CP} at the generator level [37]. Experimental smearing effects do not modulate this flat shape for decay modes in which we apply the neutral pion method for at least one τ lepton. Therefore, for this background process and these decay modes we flatten the background templates by merging the bins. The ϕ_{CP} distribution is not flat for the jet $\to \tau_h$ background for all decay modes due to the kinematic properties of the events, but the distributions are still symmetric around $\phi_{CP} = 180°$, and so this background is symmetrised — meaning the symmetry around $\phi_{CP} = 180°$ is enforced. For other background templates, for example the $\mu \to \tau_h$ contribution, the distributions are found to be flat within the statistical uncertainties, and therefore these background templates are also flattened.

The backgrounds are not expected to be flat in decay modes in which the impact parameter method is used or when the polarimetric vector method is applied when both τ leptons decay via the $a_1^{3\mathrm{pr}}$ mode. This can be understood from the fact that smearing effects in the PV are correlated for the decay planes. The smearing of the PV results in a depletion in the region $\phi_{CP} = 180^\circ$ [37], such that the shape of the background distributions in the $\mu\pi$, eπ, and $a_1^{3\mathrm{pr}}a_1^{3\mathrm{pr}}$ ($\pi\pi$) channels tends to resemble the CP-even (CP-odd) signal rather than the CP-odd (CP-even). However, for such channels the backgrounds are symmetric around $\phi_{CP} = 180^\circ$, and therefore the background templates are symmetrised.

For certain decay modes, the statistical fluctuations in the signal templates are also sizeable. Therefore, the templates for the scalar and pseudoscalar cases are symmetrised around $\phi_{CP} = 180^\circ$ as well. The maximally mixed signal template, which is not displayed in the plots, is used in the fitting procedure described in section 12. In order to symmetrise this template, we reweight the signal sample to another sample with $\alpha^{\mathrm{H}\tau\tau} = -45^\circ$. The ϕ_{CP} distribution is shifted by 180°, and the average is taken between the sample with $\alpha^{\mathrm{H}\tau\tau} = 45^\circ$ and $\alpha^{\mathrm{H}\tau\tau} = -45^\circ$.

In figures 8–10 we display the post-fit data and background template distributions, after the bin smearing and symmetrisation, with the best fit and pseudoscalar signal templates overlaid. The cross sections for the pseudoscalar signal are set to the values determined from the fit to data for the best fit signal, which are given in section 12.1. The uncertainties have been adjusted to their value after the fit described in section 12. The most sensitive decay modes of the analysis are displayed, which are the $\mu\rho$ and $\mu\pi$ mode in the $\tau_\mu\tau_\mathrm{h}$ channel displayed in figure 8, the $\rho\rho$ and $\pi\rho$ mode in the $\tau_\mathrm{h}\tau_\mathrm{h}$ channel displayed in figure 9, and the eρ and eπ channels in the $\tau_\mathrm{e}\tau_\mathrm{h}$ channel displayed in figure 10. The distributions highlight the effectiveness of the MVA discriminant in optimising the signal over background ratio, as well as the CP-sensitivity of the measurement that follows from the visibly different phases of the best fit signal and CP-odd signal distributions. The 180° phase shift between the $\tau_\mathrm{h}\tau_\mathrm{h}$ and $\tau_\ell\tau_\mathrm{h}$ channels is manifest in the figures. The correlated effect of the PV smearing is also visible in the $\mu\pi$ and eπ modes via the non-flat shapes of the background distributions.
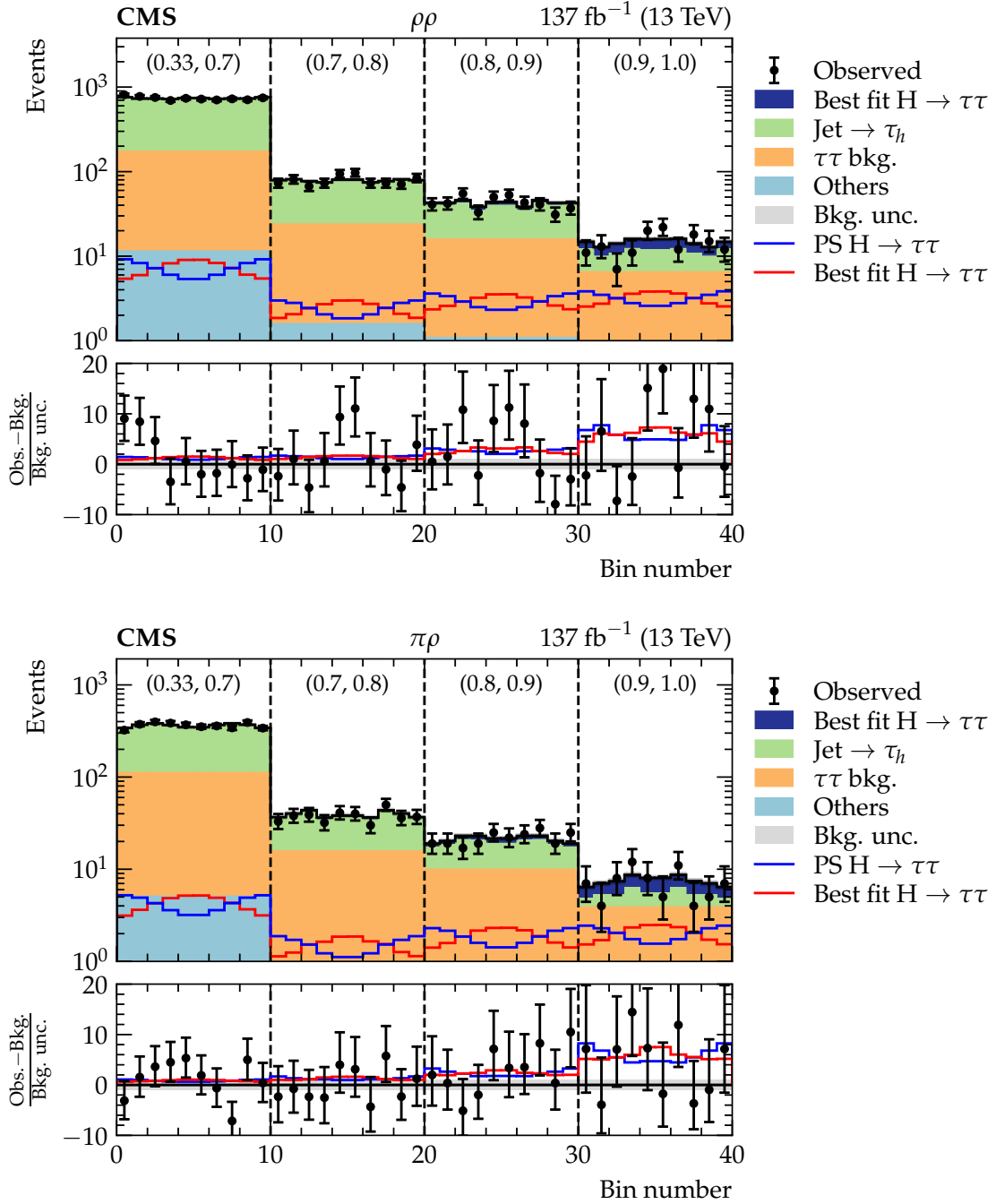
11   Systematic uncertainties

The uncertainties considered in this analysis can be categorised into normalisation and shape uncertainties. The former modify only the normalisation of a distribution while leaving its shape unchanged, whereas the latter allow for correlated changes across bins that also alter the shapes of the distributions. The uncertainties are accounted for as nuisance parameters in the fit to data. The normalisation and shape uncertainties are summarised in table 6, in which we also state their correlations between the three different years of data-taking considered in this analysis.

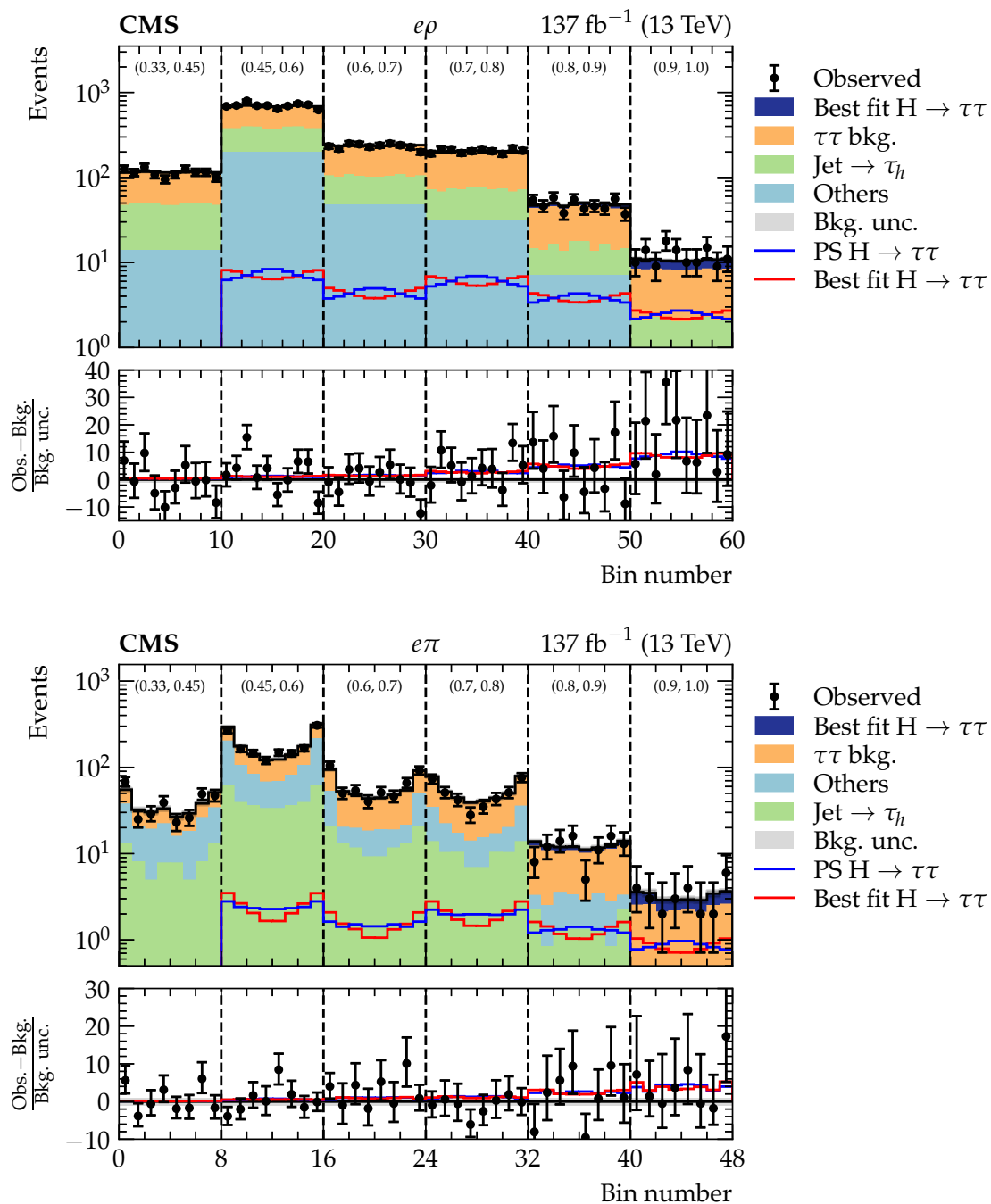### 11.1   Normalisation uncertainties

The integrated luminosity uncertainty amounts to 2.5, 2.3, and 2.5% for 2016, 2017, and 2018 respectively [101–103], and is applied to all simulated samples discussed in section 4.
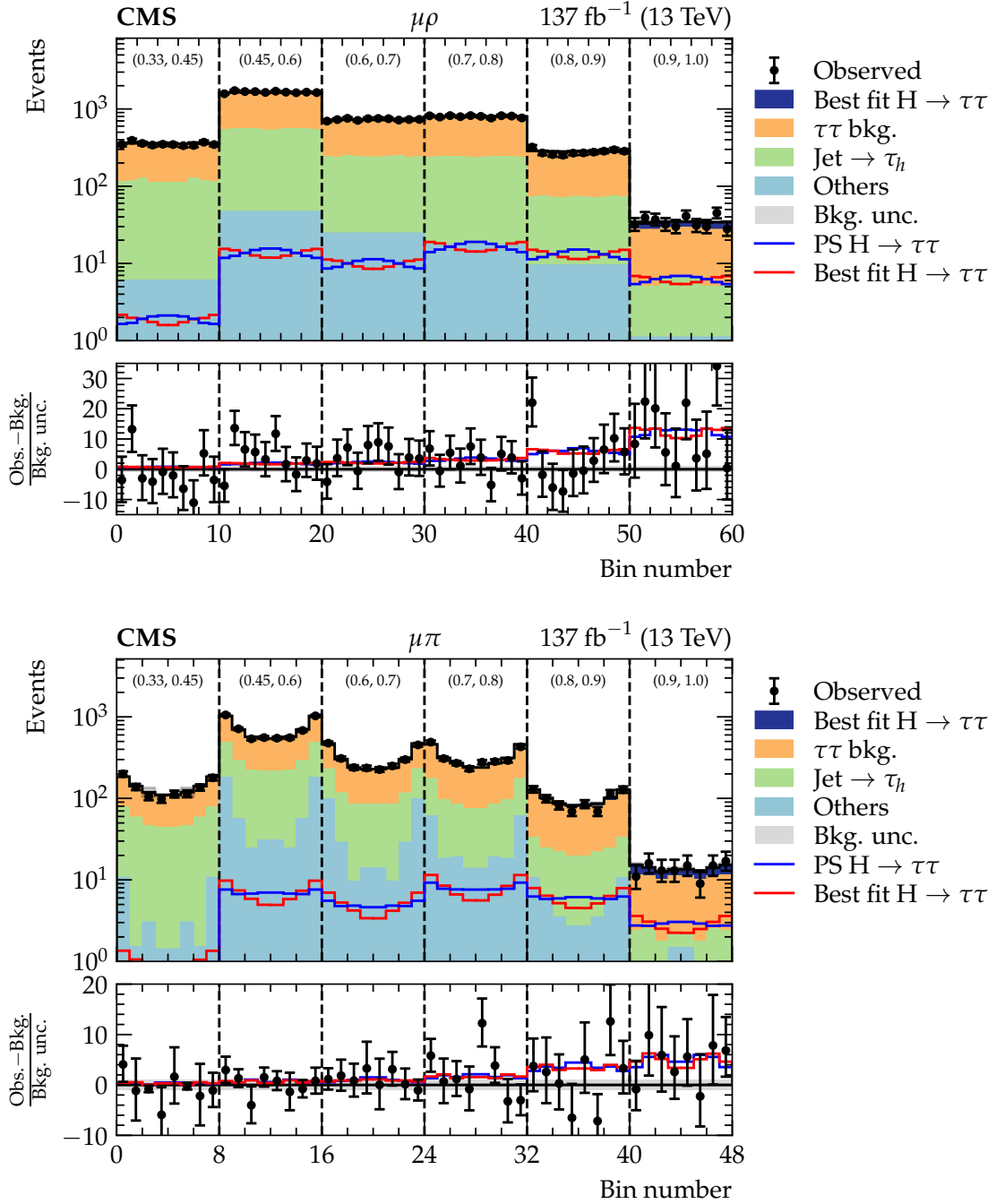
Figure 8. Distributions of ϕ_{CP} in the μρ (upper) and μπ (lower) channels in windows of increasing MVA score, shown on top of each window. The best fit and pseudoscalar (PS) signal distributions are overlaid, where in both cases the signal cross sections are set to the values obtained from the fit to data, which are given in section 12.1. The x-axis represents the cyclic bins in ϕ_{CP} in the range of $(0, 360°)$. In the lower panels, the data minus the background template divided by the uncertainty in the background template is displayed, as well as the signal distributions divided by the uncertainty in the background template. The uncertainty band accounts for all sources of systematic uncertainty in the background prediction, after the fit to data.

Figure 9. Distributions of ϕ_{CP} in the $\rho\rho$ (upper) and $\pi\rho$ (lower) channels in windows of increasing MVA score, shown on top of each window. The best fit and pseudoscalar (PS) signal distributions are overlaid, where in both cases the signal cross sections are set to the values obtained from the fit to data, which are given in section 12.1. The x-axis represents the cyclic bins in ϕ_{CP} in the range of $(0, 360^\circ)$. In the lower panels, the data minus the background template divided by the uncertainty in the background template is displayed, as well as the signal distributions divided by the uncertainty in the background template. The uncertainty band accounts for all sources of systematic uncertainty in the background prediction, after the fit to data.

Figure 10. Distributions of ϕ_{CP} in the eρ (upper) and eπ (lower) channels in windows of increasing MVA score, shown on top of each window. The best fit and pseudoscalar (PS) signal distributions are overlaid, where in both cases the signal cross sections are set to the values obtained from the fit to data, which are given in section 12.1. The x-axis represents the cyclic bins in ϕ_{CP} in the range of $(0, 360°)$. In the lower panels, the data minus the background template divided by the uncertainty in the background template is displayed, as well as the signal distributions divided by the uncertainty in the background template. The uncertainty band accounts for all sources of systematic uncertainty in the background prediction, after the fit to data.

Uncertainty	Magnitude	Correlation	Shape
Muon reconstruction	1%	Yes	No
Electron reconstruction	2%	Yes	No
Muon trigger	2%	No	No
Electron trigger	2%	No	No
$e \to \tau_h$ rate in $\tau_h\tau_h$	10 (2)% 2016 (2017,2018)	No	No
$e \to \tau_h$ rate in $\tau_e\tau_h$	10%	No	No
$\mu \to \tau_h$ rate in $\tau_\mu\tau_h$	up to 40%	No	No
b-jet veto	1-9%	No	No
Luminosity	2.3-2.5%	Partial	No
Embedded yield	4%	No	No
$t\bar{t}$ cross section	4.2%	Yes	No
Diboson cross section	5%	Yes	No
Single top quark cross section	5%	Yes	No
W + jets cross section	4%	Yes	No
Drell-Yan cross section	2%	Yes	No
H cross sections	2-5% [100]	Yes	No
$H \to \tau\tau$ branching fraction	2% [100]	Yes	No
SV reco. eff. in $a_1^{3pr}a_1^{3pr}$	2%	No	No
τ_h ID efficiency	3%	No	No
S_{IP} In μ, π, and e decays	Decay-mode dependent, 1-5%	No	No
Muon energy scale	0.4-2.7%	Yes	Yes
Electron energy scale	<1%	Yes	Yes
τ_h Trigger	p_T/Decay-mode dependent	No	Yes
τ_h Reconstruction	p_T/Decay-mode dependent (2-3%)	Partial	Yes
Top quark p_T reweighing	p_T^{top}-Dependent	Yes	Yes
Z p_T and mass reweighing	p_T^Z/m_Z-Dependent	Partial	Yes
τ_h Energy scale	p_T/Decay-mode dependent (0.2-1.1%)	No	Yes
$e \to \tau_h$ Energy scale	0.5-6.5%	No	Yes
$\mu \to \tau_h$ Energy scale	1%	No	Yes
Jet energy scale	Event-dependent	Partial	Yes
Jet energy resolution	Event-dependent	No	Yes
p_T^{miss} Unclustered scale	Event-dependent	No	Yes
p_T^{miss} Recoil corrections	Event-dependent	No	Yes
F_F uncertainties	Described in text	Partial	Yes
$t\bar{t}$/diboson in embedded	10%	Yes	Yes
L1 trigger timing (2016-2017)	Event-dependent (0-4%)	Yes	Yes
Renorm./Fact. scales	Event-dependent	Yes	Yes
Parton showering	Event-dependent	Yes	Yes

Table 6. Overview of the systematic uncertainties. The third column indicates if the source of uncertainty was treated as being correlated between the years in the fit described in section 12. The fourth column indicates if the uncertainty affects the shapes of the distributions.

The uncertainty in the muon reconstruction efficiency including the tracking, identification, and isolation requirements is 1%, while for electrons it is 2%. The uncertainty in the muon and electron trigger efficiencies, which affect both the single-lepton and cross-triggers, is 2%. An additional normalisation uncertainty of 4% is applied to the embedded event samples, originating from the uncertainty in the measurement of the muon trigger and identification efficiencies used to scale the embedded samples.

For the $\tau_\ell \tau_h$ channels, which contain a veto on events containing b-jets, an uncertainty in the propagation of the b-quark tagging scale factors of 1-9% is applied on the $t\bar{t}$ and diboson event yields (the uncertainties on the event yields for other simulated processes are found to be negligible).

The FEWZ 3.1 program [104] was used to calculate the W + jets and Z + jets cross sections. Uncertainties in the factorisation and renormalisation scales, the PDF, and the running coupling α_S were propagated and added in quadrature. The TOP++v2.0 program [105] was used to calculate the $t\bar{t}$ cross section and its uncertainty. The extracted uncertainties for the simulated Z + jets, W + jets, and $t\bar{t}$ cross sections amount to 2, 4, and 4%, respectively. For the diboson and single top quark production processes, a combined systematic uncertainty in the background yield is estimated to be 5% using CMS measurements [106, 107]. The uncertainties in the signal ggH, VBF, and VH production cross sections, as well as the uncertainty in the H $\to \tau\tau$ branching fraction, are applied as recommended in ref. [100].

The uncertainty in the $\mu \to \tau_h$ misidentification rate in the $\tau_\mu \tau_h$ channel is split into four independent uncertainties depending on the MVA decay mode of the $\mu \to \tau_h$ candidate. The sizes of the uncertainties are 20% for π and ρ, 30% for a_1^{1pr}, and 40% for a_1^{3pr}, respectively. An uncertainty of 10 (2)% to the $e \to \tau_h$ misidentification rate is applied for 2016 (2017, 2018) in the $\tau_h \tau_h$ channel. In the $\tau_e \tau_h$ channel, the $e \to \tau_h$ misidentification rate is split per decay mode and is, at most, 10%.

For the $\tau_h \tau_h$ channel, the uncertainty in the jet $\to \tau_h$ background normalisation due to the extrapolation of the F_F from same-sign to opposite-sign regions ranges between 4 and 7%.

For the decay of the τ lepton to μ or a single-pion, an uncertainty in the correction of S_{IP} is applied by varying the size of the correction by $\pm 25\%$, while for the decay to an electron the correction is varied by 40%. The uncertainty is converted into a normalisation uncertainty per decay mode and ranges 1-5%. For the $a_1^{3pr} a_1^{3pr}$ mode, the uncertainty in the SV reconstruction efficiency is 2%.

Finally, a 3% uncertainty in the efficiency of the τ_h candidates to pass the DNN discrimination against muon and electron misidentifications is applied.

11.2 Shape uncertainties

The uncertainty in the τ_h reconstruction and identification efficiency is typically of the order of 3%, and split into several uncertainties in each p_T and MVA decay mode bin. The uncertainties in these corrections originates from uncertainties in the fits to the scale factors for these corrections and are statistically dominated. We also checked if applying separate uncertainties for τ_h candidates that are incorrectly classified in a different decay

mode (e.g. a_1^{1pr} misclassified as a ρ) creates any variations in the shapes of the signal or background distributions. However, we found that such uncertainties only resulted in tiny modifications of the shapes of the ϕ_{CP} distributions, which were negligible in comparison to the statistical uncertainties in the signal and background templates, and therefore common uncertainties were used for correctly and incorrectly classified τ_h candidates in each MVA decay mode bin. The uncertainty in the τ_h trigger depends on the p_T and decay mode, and originates from the statistical uncertainty in parameterising the turn-on curve of the triggers. The τ_h energy scale uncertainty is 0.8-1.1 (0.2-0.5)% for simulated (embedded) events, and is decay mode dependent. The uncertainty in the μ momentum scale varies as a function of the η of the muon and ranges 0.4-2.7%. The uncertainty in the electron energy scale is less than 1% and depends on the p_T and η. The $e \to \tau_h$ energy scale uncertainty ranges 0.5-6.5%, while the $\mu \to \tau_h$ energy scale uncertainty is 1%.

Uncertainties in the jet energy scale originate from different sources with limited correlations. The uncertainties depend on the jet kinematics and are typically larger in the forward regions. Uncertainties in the jet energy resolution are also incorporated; these uncertainties are typically smaller than the jet energy scale uncertainties. Uncertainties related to the hadronic recoil response and resolution as derived from the $Z + jets$, $W + jets$ and signal samples, are propagated to $\vec{p}_T^{\,miss}$ and observables dependent on $\vec{p}_T^{\,miss}$ in the simulated samples that are subject to hadronic recoil corrections. For the samples in which no hadronic recoil is applied (diboson, single top quark, and $t\bar{t}$), the jet energy scale and resolution uncertainties as well as the uncertainty in the unclustered energy are propagated to $\vec{p}_T^{\,miss}$ and observables dependent on $\vec{p}_T^{\,miss}$ in the simulated samples instead.

The embedded samples contain small fractions of $t\bar{t}$ and diboson events. A shape uncertainty is therefore applied by adding and subtracting 10% of the simulated $t\bar{t}$ and diboson contributions. The top quark p_T and Drell-Yan p_T and mass spectra are reweighed. For the top samples, the size of the correction is taken as the uncertainty, while for the Drell-Yan samples the correction is varied by 10%.

The F_F values are parameterised with continuous functions, and the statistical uncertainties in the fitted parameters are treated as nuisance parameters. The uncertainties are parameterised in a manner that allows for asymmetric variations above and below the p_T value where the uncertainty is minimal; the procedure is similar to the method described in detail in ref. [11]. The size of the correction in p_T^{miss} is taken as an uncertainty for all F_F values. For the $\tau_h\tau_h$ channel, the shape uncertainty in the QCD same-sign to opposite-sign region correction is determined as the difference between a correction binned in the distance ΔR between the two τ leptons and the jet multiplicity, and the unbinned correction. For the $\tau_\ell\tau_h$ channels, the equivalent shape uncertainty is taken as the size of the same-sign to opposite-sign correction. In addition, a systematic uncertainty due to the light-lepton p_T correction is taken as the size of the correction. For the $W + jets$ F_F values, the uncertainty due to the extrapolation from the high-m_T to the low-m_T region is taken as the size of residual differences observed when applying F_F values derived for high-m_T simulated events to low-m_T simulated events. For the $t\bar{t}$ F_F, a systematic uncertainty is applied to account for potential differences between data and simulation. To this purpose, the difference between F_F values derived via data and simulated $W + jets$ samples is ap-

plied as the uncertainty. An uncertainty in the subtraction of the background processes not involving jet $\rightarrow \tau_h$ events is considered by varying the contribution predicted from simulation by $\pm 10\%$.

For uncertainties that are common to simulated and embedded samples we treat the lepton and τ_h identification uncertainties and the lepton and τ_h energy scale uncertainties as being 50% correlated. All other common uncertainties are treated as being uncorrelated.

During the 2016 and 2017 data-taking periods, a gradual shift in the timing of the inputs of the ECAL L1 trigger in the forward endcap region ($2.5 < |\eta| < 3.0$) led to a specific inefficiency. Additional correction factors and corresponding uncertainties are applied to the simulation to account for this inefficiency. The magnitude of the uncertainties ranges between 0-4% depending on the process, category, and channel.

For the signal samples, renormalisation and factorisation scales and parton showering uncertainties were incorporated [100] .

The limited number of events in the signal and background templates is accounted for using the "Barlow-Beeston" method [108, 109], which assigns a single nuisance parameter per bin per process. For background templates that have been flattened as described in section 9 the bin-by-bin uncertainties are fully correlated such that there is only one independent nuisance parameter for all ϕ_{CP} bins. For background templates that are symmetric in $\phi_{CP} = 180^\circ$ one nuisance parameter per pair of symmetrised bins is utilised. It should be noted that for flattened background templates multiple nuisance parameters are still needed per process since multiple windows of increasing MVA score are used.

We also considered other systematic uncertainties that could modify the shape of the simulated ϕ_{CP} distributions, including the energy scale, and energy and angular resolutions of the charged and neutral pions, impact parameters, and SV−PV directions. However, we found that such uncertainties only resulted in tiny modifications to the shapes of the ϕ_{CP} distributions, which were negligible in comparison to the statistical uncertainties in the signal and background templates, and they were therefore neglected in this analysis.

The systematic uncertainty scheme is validated by fitting the ϕ_{CP} distributions in a $Z \rightarrow \tau\tau$ control region, obtained following the procedure described in section 8.4. Goodness of fit tests have been performed to assess the validity of the statistical model. These tests indicated a good compatibility between the data and the model.

12 Results

In order to extract the CP-mixing angle $\alpha^{H\tau\tau}$, a simultaneous fit to the data is performed using the likelihood function $L(\mathcal{L}, \vec{\mu}, \alpha^{H\tau\tau}, \vec{\theta})$ that depends on $\vec{\mu} = (\mu_{ggH}, \mu_{qqH})$, which are the Higgs boson signal strength modifiers (defined as the cross section times $H \rightarrow \tau\tau$ branching fraction with respect to the SM value), the CP-mixing angle $\alpha^{H\tau\tau}$, and the nuisance parameters $\vec{\theta}$ that account for the systematic uncertainties. In the fit, all $H \rightarrow \tau\tau$ production processes involving V boson couplings, namely VBF and VH, are scaled by μ_{qqH}, while the ggH process is scaled by μ_{ggH}. The fit is able to differentiate between these production modes because the shapes of the MVA score distributions are different;

the VBF signal tends to peak more sharply towards larger MVA scores, whereas the ggH distribution is broader.

The likelihood function is defined as a product of conditional probabilities P over binned distributions of the discriminating observables in each event category:

$$L(\mathcal{L}, \vec{\mu}, \alpha^{\mathrm{H}\tau\tau}, \vec{\theta}) = \prod_{\mathrm{j}}^{N_{\mathrm{categories}}} \prod_{\mathrm{i}}^{N_{\mathrm{bin}}} P(n_{\mathrm{i,j}} \mid \mathcal{L}\, \vec{\mu}\, \vec{A}_{\mathrm{i,j}}(\vec{\theta}, \alpha^{\mathrm{H}\tau\tau}) + B_{\mathrm{i,j}}(\vec{\theta})) \prod_{\mathrm{m}}^{N_{\mathrm{nuisance}}} C_{\mathrm{m}}(\vec{\theta}). \quad (12.1)$$

In this equation, the Poisson distributions P correspond to the observation of $n_{\mathrm{i,j}}$ events in each bin of the discriminating observable given the expectation for the background $B_{\mathrm{i,j}}(\vec{\theta})$ and the signal $S_{\mathrm{i,j}}(\mathcal{L}, \alpha^{\mathrm{H}\tau\tau}, \vec{\mu}, \vec{\theta}) = \mathcal{L}\, \vec{\mu}\, \vec{A}_{\mathrm{i,j}}(\vec{\theta}, \alpha^{\mathrm{H}\tau\tau})$, in which $\mathcal{L}$ is the integrated luminosity and $\vec{A}_{\mathrm{i,j}}(\vec{\theta}, \alpha^{\mathrm{H}\tau\tau})$ is the signal acceptance in each production bin. Constraints on the nuisance parameters corresponding to the systematic uncertainties described in section 11 are represented by the functions $C_{\mathrm{m}}(\vec{\theta})$. A more detailed discussion on the formulation of the statistical inference may be found in refs. [109, 110]. The systematic uncertainties affecting the normalisation of the signal and background templates are incorporated in the fit via nuisance parameters with a log-normal prior probability density function. The shape-altering systematic uncertainties are represented by nuisance parameters whose variations cause continuous morphing of the signal or background template shapes, and are assigned a Gaussian prior probability density function. The bin-by-bin statistical uncertainties in the background samples are also assigned a Gaussian prior probability density function.

Using the negative log-likelihood, which is defined as

$$-2\Delta \ln L = -2 \left(\ln(L\alpha^{\mathrm{H}\tau\tau}) - \ln(L\alpha^{\mathrm{H}\tau\tau}_{\mathrm{best\ fit}}) \right), \quad (12.2)$$

we find the 68.3, 95.5, and 99.7% confidence intervals when $-2\Delta \ln L$ equals 1.00, 4.02, and 8.81, respectively. A detailed discussion may be found in section 3.2 of ref. [111].

The inputs to the likelihood fits differ for the signal and background categories. For the signal categories, the ϕ_{CP} distributions in bins of the MVA score are used (a subset of these are displayed in figures 8–10). For the background categories, the MVA score distributions are used. This allows for the background contributions and systematic uncertainties to be further constrained, and helps to improve the fit convergence.

12.1 $\alpha^{\mathrm{H}\tau\tau}$ mixing angle results

We present the observed and expected negative log-likelihood scan for the combination of the $\tau_{\mathrm{e}}\tau_{\mathrm{h}}$, $\tau_{\mu}\tau_{\mathrm{h}}$, and $\tau_{\mathrm{h}}\tau_{\mathrm{h}}$ channels in figure 11. The two rate parameters that scale the ggH and qqH production signal strength were left to float freely in the fit. The best fit values of these parameters are $\mu_{\mathrm{ggH}} = 0.59^{+0.28}_{-0.32}$ and $\mu_{\mathrm{qqH}} = 1.39^{+0.56}_{-0.47}$, respectively, with the correlation coefficient $\rho = -0.76$. We note that there is a strong anticorrelation between these parameters as the analysis does not directly attempt to differentiate between the production modes.

The data disfavour the pure CP-odd scenario at 3.0σ. The expected exclusion assuming the SM H is 2.6σ. The observed (expected) value of $\alpha^{\mathrm{H}\tau\tau}$ is found to be $-1 \pm 19^{\circ}$ ($0 \pm 21^{\circ}$) at the 68.3% CL, and $\pm 41^{\circ}$ ($\pm 49^{\circ}$) at the 95.5% CL. Furthermore, we obtain an observed
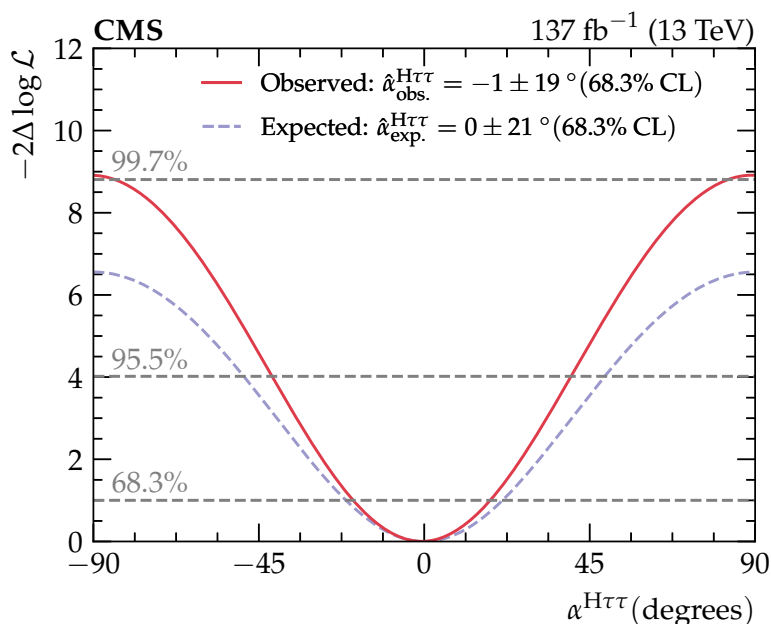
Figure 11. Negative log-likelihood scan for the combination of the $\tau_e\tau_h$, $\tau_\mu\tau_h$, and $\tau_h\tau_h$ channels. The observed (expected) sensitivity to distinguish between the scalar and pseudoscalar hypotheses, defined at $\alpha^{H\tau\tau} = 0$ and $\pm 90°$, respectively, is 3.0σ (2.6σ). The observed (expected) value for $\alpha^{H\tau\tau}$ is $-1 \pm 19°$ ($0 \pm 21°$) at the 68.3% CL. At 95.5% CL the range is $\pm 41°$ ($\pm 49°$), and at the 99.7% CL the observed range is $\pm 84°$.

$\pm 84°$ at the 99.7% CL. The uncertainty can be decomposed into: statistical; bin-by-bin fluctuations in the background templates; experimental systematic uncertainties; and theoretical uncertainties. In this decomposition we obtain

$$\alpha^{H\tau\tau} = -1 \pm 19\,(\text{stat}) \pm 1\,(\text{syst}) \pm 2\,(\text{bin-by-bin}) \pm 1\,(\text{theo})°.$$

This result is compatible with the SM predictions within the experimental uncertainties.

The expected sensitivities of the $\tau_e\tau_h$, $\tau_\mu\tau_h$, and $\tau_h\tau_h$ channels are 1.0, 1.5, and 1.8σ, respectively. The $\mu\rho$ mode yields the most sensitive expected contribution of 1.2σ, followed by the $\rho\rho$ and $\pi\rho$ modes that contribute 1.1 and 1.0σ, respectively. All other modes have sensitivities below 1σ.

The statistical uncertainties in the background templates are the subleading source of systematic uncertainty in this analysis. As the dominant contributions to the backgrounds are determined themselves from control samples in data, the amount of data is the limiting factor in this uncertainty. The next most dominant sources of uncertainty are the hadronic trigger efficiency, theory uncertainties, the τ_h energy scale, and uncertainties related to the implementation of the F_F method.

It was shown in ref. [36] that in the next-to-minimal supersymmetric model mixing angles as large as $\approx 27°$ can be accommodated by the latest electric dipole moment and Higgs boson measurements. This measurement is thus sensitive to the larger allowed mixing angles in this model.
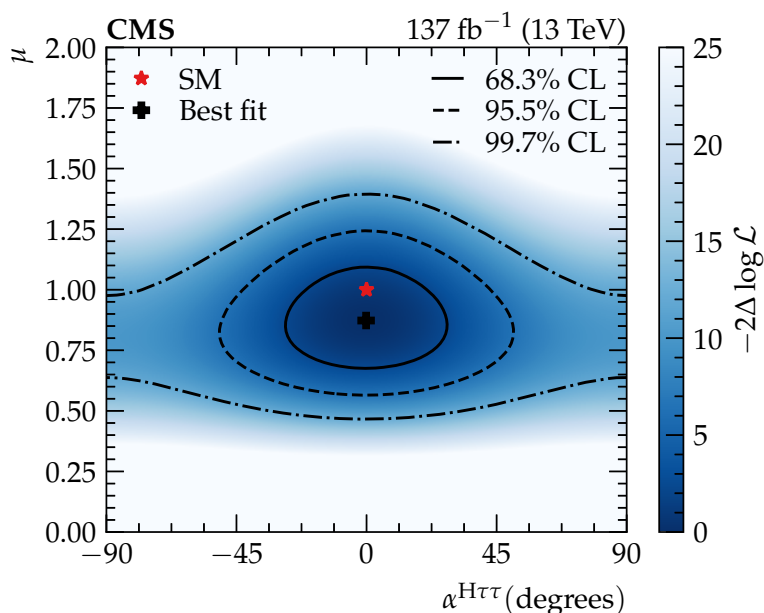
Figure 12. The 2-D scan of the signal strength modifier μ versus $\alpha^{\mathrm{H}\tau\tau}$. The 68.3, 95.5, and 99.7% confidence regions are overlaid.

A fit to the data is also performed assuming $\mu_{\mathrm{ggH}} = \mu_{\mathrm{qqH}} = \mu$. In this case μ is the combined signal strength modifier that scales the total H production cross section times $\mathrm{H} \to \tau\tau$ branching fraction relative to the SM value. In figure 12 we display a scan of μ versus $\alpha^{\mathrm{H}\tau\tau}$. We observe that there is no strong correlation between these parameters.

In order to make a 2-D scan of κ_τ and $\widetilde{\kappa}_\tau$, as defined in eq. (2.2), we parameterise the likelihood from eq. (12.1) in terms of κ_τ and $\widetilde{\kappa}_\tau$. All other H couplings are fixed to their expected SM values.

In the case of a 2-D negative log-likelihood, the 68.3, 95.5, and 99.7% confidence regions are found when $-2\Delta \ln L_{\mathrm{2D}}$ equals 2.30, 6.20, and 11.62 [111], respectively, defined analogously to eq. (12.2) with the likelihood now a function of both κ_τ and $\widetilde{\kappa}_\tau$. All other CP-even (CP-odd) couplings affecting the production cross sections and/or the $\mathrm{H} \to \tau\tau$ branching fraction are fixed to their SM values, $\kappa_i = 1$ ($\widetilde{\kappa}_i = 0$). The observed result of the scan is shown in figure 13. It should be noted that the fit is only sensitive to the relative sign between κ_τ and $\widetilde{\kappa}_\tau$ and thus the scan has two best fit points for positive and negative values of κ_τ.

In figure 14 we display the data of the $\rho\rho$, $\pi\rho$, $\mu\rho$, and $\mathrm{e}\rho$ channel together with CP-even and CP-odd predictions. These channels are chosen as the same number of ϕ_{CP} bins are used in the fit to data, and collectively they account for most of the sensitivity to $\alpha^{\mathrm{H}\tau\tau}$. Events are included from all MVA score bins in these signal categories. Each MVA score bin is weighed by $A\,S/(S+B)$, where S and B are the signal and background rates, respectively, and A is a measure for the average asymmetry between the scalar
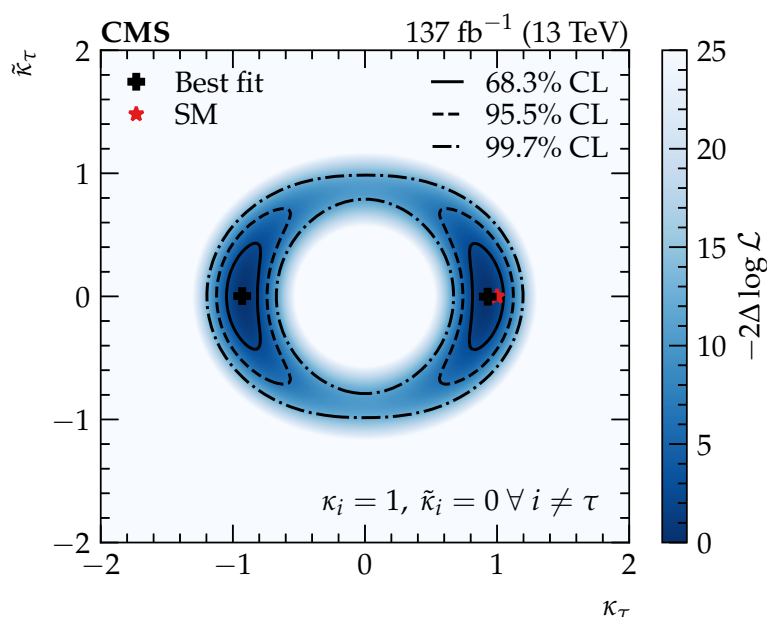
Figure 13. The 2-D scan of the (reduced) *CP*-even (κ_τ) and *CP*-odd ($\widetilde{\kappa}_\tau$) τ Yukawa couplings. The 68.3, 95.5, and 99.7% confidence regions are overlaid.

and pseudoscalar distributions. The definition of the value of A per bin is $|CP^{\mathrm{even}} - CP^{\mathrm{odd}}|/(CP^{\mathrm{even}} + CP^{\mathrm{odd}})$, and A is normalised to the total number of bins. In this equation, CP^{even} and CP^{odd} are the scalar and pseudoscalar contributions per bin. This distribution shows that the data favour the *CP*-even scenario.

13 Summary

The first measurement of the effective mixing angle $\alpha^{\mathrm{H}\tau\tau}$ between scalar and pseudoscalar Hττ couplings has been presented for a data set of proton-proton collisions at $\sqrt{s} = 13\,\mathrm{TeV}$ corresponding to an integrated luminosity of $137\,\mathrm{fb}^{-1}$. The data were collected with the CMS experiment at the LHC in the period 2016-2018. The following τ lepton decay modes were included: $\mathrm{e}^\pm$, $\mu^\pm$, $\pi^\pm$, $\rho^\pm \to \pi^\pm\pi^0$, $\mathrm{a_1}^\pm \to \pi^\pm\pi^0\pi^0$, and $\mathrm{a_1}^\pm \to \pi^\pm\pi^\mp\pi^\pm$. Dedicated strategies were adopted to reconstruct the angle ϕ_{CP} between the τ decay planes for the various τ decay modes. The data disfavour the pure *CP*-odd scenario at 3.0 standard deviations. The observed effective mixing angle is found to be $-1\pm19°$, while the expected value is $0\pm21°$ at the 68.3% confidence level (CL). The observed and expected uncertainties are found to be $\pm41°$ and $\pm49°$ at the 95.5% CL, respectively, and the observed sensitivity at the 99.7% CL is $\pm84°$. The leading uncertainty in the measurement is statistical, implying that the precision of the measurement will increase with the accumulation of more collision data. The measurement is consistent with the standard model expectation, and reduces the allowed parameter space for its extensions. Tabulated results are provided in HEPDATA [112].
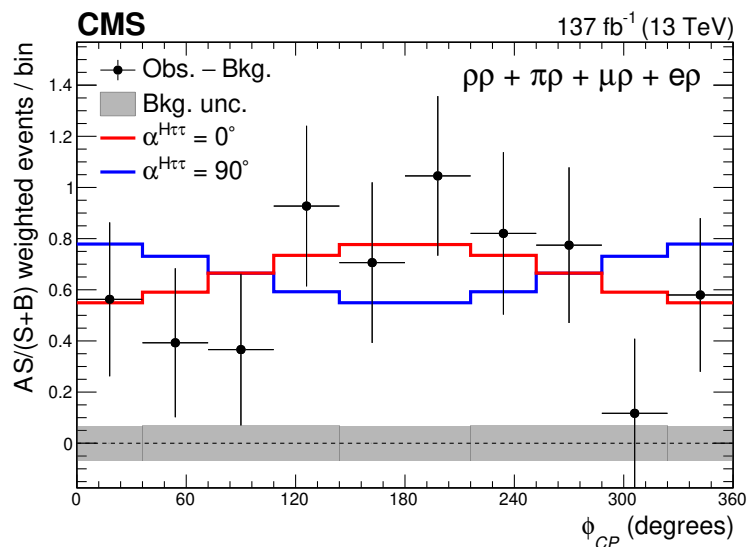
Figure 14. The ϕ_{CP} distributions for the $\rho\rho$, $\pi\rho$, $\mu\rho$, and $e\rho$ channels weighed by $A\,S/(S+B)$ are combined. Events are included from all MVA score bins in the four signal categories. The background is subtracted from the data. The scalar distribution is depicted in red, while the pseudoscalar is displayed in blue. In the predictions, the rate parameters are taken from their best fit values. The grey uncertainty band indicates the uncertainty in the subtracted background component. In combining the channels, a phase-shift of $180°$ was applied to the channels involving a lepton since this channel has a phase difference of $180°$ with respect to the two hadronic channels due to a sign-flip in the spectral function of the light lepton.

Acknowledgments

References

[1] F. Englert and R. Brout, *Broken Symmetry and the Mass of Gauge Vector Mesons*, *[Phys. Rev. Lett.](#)* **13** (1964) 321 [ɪɴSPIRE].

[2] P.W. Higgs, *Broken symmetries, massless particles and gauge fields*, *[Phys. Lett.](#)* **12** (1964) 132 [ɪɴSPIRE].

[3] P.W. Higgs, *Broken Symmetries and the Masses of Gauge Bosons*, *Phys. Rev. Lett.* **13** (1964) 508 [InSPIRE].

[4] G.S. Guralnik, C.R. Hagen and T.W.B. Kibble, *Global Conservation Laws and Massless Particles*, *Phys. Rev. Lett.* **13** (1964) 585 [InSPIRE].

[5] P.W. Higgs, *Spontaneous Symmetry Breakdown without Massless Bosons*, *Phys. Rev.* **145** (1966) 1156 [InSPIRE].

[6] T.W.B. Kibble, *Symmetry breaking in non-Abelian gauge theories*, *Phys. Rev.* **155** (1967) 1554 [InSPIRE].

[7] ATLAS collaboration, *Observation of a new particle in the search for the Standard Model Higgs boson with the ATLAS detector at the LHC*, *Phys. Lett. B* **716** (2012) 1 [arXiv:1207.7214] [InSPIRE].

[8] CMS collaboration, *Observation of a New Boson at a Mass of 125 GeV with the CMS Experiment at the LHC*, *Phys. Lett. B* **716** (2012) 30 [arXiv:1207.7235] [InSPIRE].

[9] CMS collaboration, *Observation of a New Boson with Mass Near 125 GeV in pp Collisions at $\sqrt{s}$ = 7 and 8 TeV*, *JHEP* **06** (2013) 081 [arXiv:1303.4571] [InSPIRE].

[10] ATLAS, CMS collaborations, *Measurements of the Higgs boson production and decay rates and constraints on its couplings from a combined ATLAS and CMS analysis of the LHC pp collision data at $\sqrt{s}$ = 7 and 8 TeV*, *JHEP* **08** (2016) 045 [arXiv:1606.02266] [InSPIRE].

[11] CMS collaboration, *Observation of the Higgs boson decay to a pair of τ leptons with the CMS detector*, *Phys. Lett. B* **779** (2018) 283 [arXiv:1708.00373] [InSPIRE].

[12] ATLAS collaboration, *Cross-section measurements of the Higgs boson decaying into a pair of τ-leptons in proton-proton collisions at $\sqrt{s}$ = 13 TeV with the ATLAS detector*, *Phys. Rev. D* **99** (2019) 072001 [arXiv:1811.08856] [InSPIRE].

[13] CMS collaboration, *A measurement of the Higgs boson mass in the diphoton decay channel*, *Phys. Lett. B* **805** (2020) 135425 [arXiv:2002.06398] [InSPIRE].

[14] CMS collaboration, *Study of the Mass and Spin-Parity of the Higgs Boson Candidate Via Its Decays to Z Boson Pairs*, *Phys. Rev. Lett.* **110** (2013) 081803 [arXiv:1212.6639] [InSPIRE].

[15] CMS collaboration, *Measurement of the Properties of a Higgs Boson in the Four-Lepton Final State*, *Phys. Rev. D* **89** (2014) 092007 [arXiv:1312.5353] [InSPIRE].

[16] CMS collaboration, *Constraints on the spin-parity and anomalous HVV couplings of the Higgs boson in proton collisions at 7 and 8 TeV*, *Phys. Rev. D* **92** (2015) 012004 [arXiv:1411.3441] [InSPIRE].

[17] CMS collaboration, *Limits on the Higgs boson lifetime and width from its decay to four charged leptons*, *Phys. Rev. D* **92** (2015) 072010 [arXiv:1507.06656] [InSPIRE].

[18] CMS collaboration, *Combined search for anomalous pseudoscalar HVV couplings in VH(H $\rightarrow b\bar{b}$) production and H $\rightarrow$ VV decay*, *Phys. Lett. B* **759** (2016) 672 [arXiv:1602.04305] [InSPIRE].

[19] CMS collaboration, *Constraints on anomalous Higgs boson couplings using production and decay information in the four-lepton final state*, *Phys. Lett. B* **775** (2017) 1 [arXiv:1707.00541] [InSPIRE].

[20] CMS collaboration, *Constraints on anomalous HVV couplings from the production of Higgs bosons decaying to τ lepton pairs*, *Phys. Rev. D* **100** (2019) 112002 [arXiv:1903.06973] [INSPIRE].

[21] CMS collaboration, *Constraints on anomalous Higgs boson couplings to vector bosons and fermions in its production and decay using the four-lepton final state*, *Phys. Rev. D* **104** (2021) 052004 [arXiv:2104.12152] [INSPIRE].

[22] ATLAS collaboration, *Evidence for the spin-0 nature of the Higgs boson using ATLAS data*, *Phys. Lett. B* **726** (2013) 120 [arXiv:1307.1432] [INSPIRE].

[23] ATLAS collaboration, *Study of the spin and parity of the Higgs boson in diboson decays with the ATLAS detector*, *Eur. Phys. J. C* **75** (2015) 476 [*Erratum ibid.* **76** (2016) 152] [arXiv:1506.05669] [INSPIRE].

[24] ATLAS collaboration, *Test of CP Invariance in vector-boson fusion production of the Higgs boson using the Optimal Observable method in the ditau decay channel with the ATLAS detector*, *Eur. Phys. J. C* **76** (2016) 658 [arXiv:1602.04516] [INSPIRE].

[25] ATLAS collaboration, *Measurement of inclusive and differential cross sections in the $H \to ZZ^* \to 4\ell$ decay channel in pp collisions at $\sqrt{s} = 13$ TeV with the ATLAS detector*, *JHEP* **10** (2017) 132 [arXiv:1708.02810] [INSPIRE].

[26] ATLAS collaboration, *Measurement of the Higgs boson coupling properties in the $H \to ZZ^* \to 4\ell$ decay channel at $\sqrt{s} = 13$ TeV with the ATLAS detector*, *JHEP* **03** (2018) 095 [arXiv:1712.02304] [INSPIRE].

[27] ATLAS collaboration, *Measurements of Higgs boson properties in the diphoton decay channel with 36 fb^{-1} of pp collision data at $\sqrt{s} = 13$ TeV with the ATLAS detector*, *Phys. Rev. D* **98** (2018) 052005 [arXiv:1802.04146] [INSPIRE].

[28] C. Zhang and S. Willenbrock, *Effective-Field-Theory Approach to Top-Quark Production and Decay*, *Phys. Rev. D* **83** (2011) 034006 [arXiv:1008.3869] [INSPIRE].

[29] R. Harnik, A. Martin, T. Okui, R. Primulando and F. Yu, *Measuring CP-violation in $h \to \tau^+\tau^-$ at Colliders*, *Phys. Rev. D* **88** (2013) 076009 [arXiv:1308.1094] [INSPIRE].

[30] T. Ghosh, R. Godbole and X. Tata, *Determining the spacetime structure of bottom-quark couplings to spin-zero particles*, *Phys. Rev. D* **100** (2019) 015026 [arXiv:1904.09895] [INSPIRE].

[31] A.V. Gritsan, R. Röntsch, M. Schulze and M. Xiao, *Constraining anomalous Higgs boson couplings to the heavy flavor fermions using matrix element techniques*, *Phys. Rev. D* **94** (2016) 055023 [arXiv:1606.03107] [INSPIRE].

[32] CMS collaboration, *Measurements of $t\bar{t}H$ Production and the CP Structure of the Yukawa Interaction between the Higgs Boson and Top Quark in the Diphoton Decay Channel*, *Phys. Rev. Lett.* **125** (2020) 061801 [arXiv:2003.10866] [INSPIRE].

[33] ATLAS collaboration, *CP Properties of Higgs Boson Interactions with Top Quarks in the $t\bar{t}H$ and tH Processes Using $H \to \gamma\gamma$ with the ATLAS Detector*, *Phys. Rev. Lett.* **125** (2020) 061802 [arXiv:2004.04545] [INSPIRE].

[34] ATLAS collaboration, *Constraints on Higgs boson properties using $WW^*(\to e\nu\mu\nu)jj$ production in 36.1 fb^{-1} of $\sqrt{s}$=13 TeV pp collisions with the ATLAS detector*, arXiv:2109.13808, submitted to *Eur. Phys. J. C* [INSPIRE].

[35] D. Fontes, J.C. Romão, R. Santos and J.P. Silva, *Large pseudoscalar Yukawa couplings in the complex 2HDM*, *JHEP* **06** (2015) 060 [arXiv:1502.01720] [INSPIRE].

[36] S.F. King, M. Mühlleitner, R. Nevzorov and K. Walz, *Exploring the CP-violating NMSSM: EDM Constraints and Phenomenology*, *Nucl. Phys. B* **901** (2015) 526 [arXiv:1508.03255] [INSPIRE].

[37] S. Berge, W. Bernreuther and S. Kirchner, *Determination of the Higgs CP-mixing angle in the tau decay channels at the LHC including the Drell–Yan background*, *Eur. Phys. J. C* **74** (2014) 3164 [arXiv:1408.0798] [INSPIRE].

[38] PARTICLE DATA GROUP collaboration, *Review of Particle Physics*, *PTEP* **2020** (2020) 083C01 [INSPIRE].

[39] S. Berge, W. Bernreuther and S. Kirchner, *Determination of the Higgs CP-mixing angle in the tau decay channels*, *Nucl. Part. Phys. Proc.* **273-275** (2016) 841 [arXiv:1410.6362] [INSPIRE].

[40] S. Berge, W. Bernreuther, B. Niepelt and H. Spiesberger, *How to pin down the CP quantum numbers of a Higgs boson in its tau decays at the LHC*, *Phys. Rev. D* **84** (2011) 116003 [arXiv:1108.0670] [INSPIRE].

[41] J.R. Dell'Aquila and C.A. Nelson, *Distinguishing a Spin 0 Technipion and an Elementary Higgs Boson: V_1V_2 Modes With Decays Into $\bar{\ell}_A\ell_B$ and/or $\bar{q}_Aq_B$*, *Phys. Rev. D* **33** (1986) 93 [INSPIRE].

[42] M. Krämer, J.H. Kühn, M.L. Stong and P.M. Zerwas, *Prospects of measuring the parity of Higgs particles*, *Z. Phys. C* **64** (1994) 21 [hep-ph/9404280] [INSPIRE].

[43] CMS collaboration, *Performance of the CMS Level-1 trigger in proton-proton collisions at $\sqrt{s} = 13$ TeV*, 2020 *JINST* **15** P10017 [arXiv:2006.10165] [INSPIRE].

[44] CMS collaboration, *The CMS trigger system*, 2017 *JINST* **12** P01020 [arXiv:1609.02366] [INSPIRE].

[45] CMS collaboration, *The CMS Experiment at the CERN LHC*, 2008 *JINST* **3** S08004 [INSPIRE].

[46] P. Nason, *A New method for combining NLO QCD with shower Monte Carlo algorithms*, *JHEP* **11** (2004) 040 [hep-ph/0409146] [INSPIRE].

[47] S. Frixione, P. Nason and C. Oleari, *Matching NLO QCD computations with Parton Shower simulations: the POWHEG method*, *JHEP* **11** (2007) 070 [arXiv:0709.2092] [INSPIRE].

[48] S. Alioli, P. Nason, C. Oleari and E. Re, *A general framework for implementing NLO calculations in shower Monte Carlo programs: the POWHEG BOX*, *JHEP* **06** (2010) 043 [arXiv:1002.2581] [INSPIRE].

[49] E. Bagnaschi, G. Degrassi, P. Slavich and A. Vicini, *Higgs production via gluon fusion in the POWHEG approach in the SM and in the MSSM*, *JHEP* **02** (2012) 088 [arXiv:1111.2854] [INSPIRE].

[50] P. Nason and C. Oleari, *NLO Higgs boson production via vector-boson fusion matched with shower in POWHEG*, *JHEP* **02** (2010) 037 [arXiv:0911.5299] [INSPIRE].

[51] T. Ježo and P. Nason, *On the Treatment of Resonances in Next-to-Leading Order Calculations Matched to a Parton Shower*, *JHEP* **12** (2015) 065 [arXiv:1509.09071] [INSPIRE].

[52] F. Granata, J.M. Lindert, C. Oleari and S. Pozzorini, *NLO QCD+EW predictions for HV and HV +jet production including parton-shower effects*, *JHEP* **09** (2017) 012 [arXiv:1706.03522] [INSPIRE].

[53] G. Klamke and D. Zeppenfeld, *Higgs plus two jet production via gluon fusion as a signal at the CERN LHC*, *JHEP* **04** (2007) 052 [hep-ph/0703202] [INSPIRE].

[54] F. Demartin, F. Maltoni, K. Mawatari, B. Page and M. Zaro, *Higgs characterisation at NLO in QCD: CP properties of the top-quark Yukawa interaction*, *Eur. Phys. J. C* **74** (2014) 3065 [arXiv:1407.5089] [INSPIRE].

[55] K. Hamilton, P. Nason, E. Re and G. Zanderighi, *NNLOPS simulation of Higgs boson production*, *JHEP* **10** (2013) 222 [arXiv:1309.0017] [INSPIRE].

[56] K. Hamilton, P. Nason and G. Zanderighi, *Finite quark-mass effects in the NNLOPS POWHEG+MiNLO Higgs generator*, *JHEP* **05** (2015) 140 [arXiv:1501.04637] [INSPIRE].

[57] T. Sjöstrand, S. Ask, J.R. Christiansen, R. Corke, N. Desai, P. Ilten et al., *An introduction to PYTHIA 8.2*, *Comput. Phys. Commun.* **191** (2015) 159 [arXiv:1410.3012] [INSPIRE].

[58] T. Przedzinski, E. Richter-Was and Z. Was, *Documentation of TauSpinner algorithms: program for simulating spin effects in τ -lepton production at LHC*, *Eur. Phys. J. C* **79** (2019) 91 [arXiv:1802.05459] [INSPIRE].

[59] NNPDF collaboration, *Parton distributions for the LHC Run II*, *JHEP* **04** (2015) 040 [arXiv:1410.8849] [INSPIRE].

[60] NNPDF collaboration, *Parton distributions from high-precision collider data*, *Eur. Phys. J. C* **77** (2017) 663 [arXiv:1706.00428] [INSPIRE].

[61] J. Alwall, R. Frederix, S. Frixione, V. Hirschi, F. Maltoni, O. Mattelaer et al., *The automated computation of tree-level and next-to-leading order differential cross sections, and their matching to parton shower simulations*, *JHEP* **07** (2014) 079 [arXiv:1405.0301] [INSPIRE].

[62] J. Alwall et al., *Comparative study of various algorithms for the merging of parton showers and matrix elements in hadronic collisions*, *Eur. Phys. J. C* **53** (2008) 473 [arXiv:0706.2569] [INSPIRE].

[63] S. Alioli, S.-O. Moch and P. Uwer, *Hadronic top-quark pair-production with one jet and parton showering*, *JHEP* **01** (2012) 137 [arXiv:1110.5251] [INSPIRE].

[64] E. Re, *Single-top Wt-channel production matched with parton showers using the POWHEG method*, *Eur. Phys. J. C* **71** (2011) 1547 [arXiv:1009.2450] [INSPIRE].

[65] R. Frederix, E. Re and P. Torrielli, *Single-top t-channel hadroproduction in the four-flavour scheme with POWHEG and aMC@NLO*, *JHEP* **09** (2012) 130 [arXiv:1207.5391] [INSPIRE].

[66] CMS collaboration, *Event generator tunes obtained from underlying event and multiparton scattering measurements*, *Eur. Phys. J. C* **76** (2016) 155 [arXiv:1512.00815] [INSPIRE].

[67] CMS collaboration, *Extraction and validation of a new set of CMS PYTHIA8 tunes from underlying-event measurements*, *Eur. Phys. J. C* **80** (2020) 4 [arXiv:1903.12179] [INSPIRE].

[68] GEANT4 collaboration, *GEANT4–a simulation toolkit*, *Nucl. Instrum. Meth. A* **506** (2003) 250 [INSPIRE].

[69] CMS collaboration, *Particle-flow reconstruction and global event description with the CMS detector*, 2017 *JINST* **12** P10003 [`arXiv:1706.04965`] [INSPIRE].

[70] CMS collaboration, *Description and performance of track and primary-vertex reconstruction with the CMS tracker*, 2014 *JINST* **9** P10009 [`arXiv:1405.6569`] [INSPIRE].

[71] K. Rose, *Deterministic annealing for clustering, compression, classification, regression, and related optimization problems*, *IEEE Proc.* **86** (1998) 2210 [INSPIRE].

[72] W. Waltenberger, R. Frühwirth and P. Vanlaer, *Adaptive vertex fitting*, *J. Phys. G* **34** (2007) N343,

[73] M. Cacciari, G.P. Salam and G. Soyez, *The anti-k_t jet clustering algorithm*, *JHEP* **04** (2008) 063 [`arXiv:0802.1189`] [INSPIRE].

[74] CMS collaboration, *Performance of CMS Muon Reconstruction in pp Collision Events at $\sqrt{s} = 7$ TeV*, 2012 *JINST* **7** P10002 [`arXiv:1206.4071`] [INSPIRE].

[75] CMS collaboration, *Performance of Electron Reconstruction and Selection with the CMS Detector in Proton-Proton Collisions at $\sqrt{s} = 8$ TeV*, 2015 *JINST* **10** P06005 [`arXiv:1502.02701`] [INSPIRE].

[76] M. Cacciari, G.P. Salam and G. Soyez, *FastJet User Manual*, *Eur. Phys. J. C* **72** (2012) 1896 [`arXiv:1111.6097`] [INSPIRE].

[77] CMS collaboration, *Jet algorithms performance in 13 TeV data*, Tech. Rep. CMS-PAS-JME-16-003, CERN, Geneva (2017).

[78] CMS collaboration, *Jet energy scale and resolution in the CMS experiment in pp collisions at 8 TeV*, 2017 *JINST* **12** P02014 [`arXiv:1607.03663`] [INSPIRE].

[79] CMS collaboration, *Identification of heavy-flavour jets with the CMS detector in pp collisions at 13 TeV*, 2018 *JINST* **13** P05011 [`arXiv:1712.07158`] [INSPIRE].

[80] D. Bertolini, P. Harris, M. Low and N. Tran, *Pileup Per Particle Identification*, *JHEP* **10** (2014) 059 [`arXiv:1407.6013`] [INSPIRE].

[81] CMS collaboration, *Performance of missing transverse momentum reconstruction in proton-proton collisions at $\sqrt{s} = 13$ TeV using the CMS detector*, 2019 *JINST* **14** P07004 [`arXiv:1903.06078`] [INSPIRE].

[82] CMS collaboration, *Performance of reconstruction and identification of τ leptons decaying to hadrons and ν_τ in pp collisions at $\sqrt{s} = 13$ TeV*, 2018 *JINST* **13** P10005 [`arXiv:1809.02816`] [INSPIRE].

[83] CMS collaboration, *Identification of hadronic tau lepton decays using a deep neural network*, `arXiv:2201.08458` [INSPIRE].

[84] L. Bianchini, J. Conway, E.K. Friis and C. Veelken, *Reconstruction of the Higgs mass in $H \to \tau\tau$ Events by Dynamical Likelihood techniques*, *J. Phys. Conf. Ser.* **513** (2014) 022035 [INSPIRE].

[85] S. Berge and W. Bernreuther, *Determining the CP parity of Higgs bosons at the LHC in the tau to 1-prong decay channels*, *Phys. Lett. B* **671** (2009) 470 [`arXiv:0812.1910`] [INSPIRE].

[86] S. Berge, W. Bernreuther and S. Kirchner, *Prospects of constraining the Higgs boson's CP nature in the tau decay channel at the LHC*, *Phys. Rev. D* **92** (2015) 096012 [`arXiv:1510.03850`] [INSPIRE].

[87] G.R. Bower, T. Pierzchala, Z. Was and M. Worek, *Measuring the Higgs boson's parity using* $\tau \to \rho\nu$, *Phys. Lett. B* **543** (2002) 227 [hep-ph/0204292] [INSPIRE].

[88] V. Cherepanov, E. Richter-Was and Z. Was, *Monte Carlo, fitting and Machine Learning for Tau leptons*, *SciPost Phys. Proc.* **1** (2019) 018 [arXiv:1811.03969] [INSPIRE].

[89] V. Cherepanov and A. Zotz, *Kinematic reconstruction of* $Z/H \to \tau\tau$ *decay in proton-proton collisions*, arXiv:1805.06988 [INSPIRE].

[90] S. Jadach, J.H. Kühn and Z. Was, *TAUOLA: A Library of Monte Carlo programs to simulate decays of polarized tau leptons*, *Comput. Phys. Commun.* **64** (1990) 275 [INSPIRE].

[91] M. Jezabek, Z. Was, S. Jadach and J.H. Kühn, *The tau decay library TAUOLA, update with exact O(alpha) QED corrections in* $\tau \to \mu(e)\nu\bar{\nu}$ *decay modes*, *Comput. Phys. Commun.* **70** (1992) 69 [INSPIRE].

[92] S. Jadach, Z. Was, R. Decker and J.H. Kühn, *The tau decay library TAUOLA: Version 2.4*, *Comput. Phys. Commun.* **76** (1993) 361 [INSPIRE].

[93] CLEO collaboration, *Hadronic structure in the decay* $\tau \to \nu_\tau \pi^- \pi^0 \pi^0$ *and the sign of the* ν_τ *helicity*, *Phys. Rev. D* **61** (2000) 012002 [hep-ex/9902022] [INSPIRE].

[94] CMS collaboration, *Identification of hadronic tau decay channels using multivariate analysis (MVA decay mode)*, CMS Detector Performance Note CMS-DP-2020-041, CERN-CMS-DP-2020-041, CERN, Geneva (2020).

[95] T. Chen and C. Guestrin, *XGBoost: A Scalable Tree Boosting System*, in proceedings of the *22nd ACM SIGKDD International Conference on Knowledge Discovery and Data Mining*, *KDD '16* (2016) p. 785. [arXiv:1603.02754] [INSPIRE].

[96] CMS collaboration, *An embedding technique to determine* $\tau\tau$ *backgrounds in proton-proton collision data*, 2019 *JINST* **14** P06032 [arXiv:1903.01216] [INSPIRE].

[97] CMS collaboration, *Measurement of the* $Z/\gamma^* \to \tau\tau$ *cross section in pp collisions at* $\sqrt{s} = 13$ *TeV and validation of* τ *lepton analysis techniques*, *Eur. Phys. J. C* **78** (2018) 708 [arXiv:1801.03535] [INSPIRE].

[98] CMS collaboration, *Measurements of Inclusive W and Z Cross Sections in pp Collisions at* $\sqrt{s} = 7$ *TeV*, *JHEP* **01** (2011) 080 [arXiv:1012.2466] [INSPIRE].

[99] CMS collaboration, *Measurement of the differential cross section for top quark pair production in pp collisions at* $\sqrt{s} = 8$ *TeV*, *Eur. Phys. J. C* **75** (2015) 542 [arXiv:1505.04480] [INSPIRE].

[100] LHC HIGGS CROSS SECTION WORKING GROUP collaboration, *Handbook of LHC Higgs Cross Sections: 4. Deciphering the Nature of the Higgs Sector*, arXiv:1610.07922 [INSPIRE].

[101] CMS collaboration, *CMS Luminosity Measurements for the 2016 Data Taking Period*, Tech. Rep. CMS-PAS-LUM-17-001, CERN, Geneva (2017).

[102] CMS collaboration, *CMS luminosity measurement for the 2017 data-taking period at* $\sqrt{s} = 13$ TeV, Tech. Rep. CMS-PAS-LUM-17-004, CERN, Geneva (2018).

[103] CMS collaboration, *CMS luminosity measurement for the 2018 data-taking period at* $\sqrt{s} = 13$ TeV, Tech. Rep. CMS-PAS-LUM-18-002, CERN, Geneva (2019).

[104] Y. Li and F. Petriello, *Combining QCD and electroweak corrections to dilepton production in FEWZ*, *Phys. Rev. D* **86** (2012) 094034 [arXiv:1208.5967] [INSPIRE].

[105] M. Czakon and A. Mitov, *Top++: A Program for the Calculation of the Top-Pair Cross-Section at Hadron Colliders*, *Comput. Phys. Commun.* **185** (2014) 2930 [arXiv:1112.5675] [INSPIRE].

[106] CMS collaboration, *Measurement of the WZ production cross section in pp collisions at $\sqrt{s} = 13$ TeV*, *Phys. Lett. B* **766** (2017) 268 [arXiv:1607.06943] [INSPIRE].

[107] CMS collaboration, *Cross section measurement of t-channel single top quark production in pp collisions at $\sqrt{s} = 13$ TeV*, *Phys. Lett. B* **772** (2017) 752 [arXiv:1610.00678] [INSPIRE].

[108] R.J. Barlow and C. Beeston, *Fitting using finite Monte Carlo samples*, *Comput. Phys. Commun.* **77** (1993) 219 [INSPIRE].

[109] J.S. Conway, *Incorporating Nuisance Parameters in Likelihoods for Multisource Spectra*, in *PHYSTAT 2011* (2011) 115 [arXiv:1103.0354] [INSPIRE].

[110] THE ATLAS COLLABORATION, THE CMS COLLABORATION, THE LHC HIGGS COMBINATION GROUP collaboration, *Procedure for the LHC Higgs boson search combination in Summer 2011*, Tech. Rep. CMS-NOTE-2011-005, ATL-PHYS-PUB-2011-11, CERN, Geneva (2011).

[111] CMS collaboration, *Precise determination of the mass of the Higgs boson and tests of compatibility of its couplings with the standard model predictions using proton collisions at 7 and 8 TeV*, *Eur. Phys. J. C* **75** (2015) 212 [arXiv:1412.8662] [INSPIRE].

[112] CMS collaboration, *Analysis of the CP structure of the Yukawa coupling between the Higgs boson and τ leptons in proton-proton collisions at $\sqrt{s} = 13$ TeV*, HEPData collection, 10.17182/hepdata.104978 (2021).

The CMS collaboration

Yerevan Physics Institute, Yerevan, Armenia

A. Tumasyan

Institut für Hochenergiephysik, Vienna, Austria

W. Adam, J.W. Andrejkovic, T. Bergauer, S. Chatterjee, M. Dragicevic, A. Escalante Del Valle, R. Frühwirth[1], M. Jeitler[1], N. Krammer, L. Lechner, D. Liko, I. Mikulec, P. Paulitsch, F.M. Pitters, J. Schieck[1], R. Schöfbeck, D. Schwarz, S. Templ, W. Waltenberger, C.-E. Wulz[1]

Institute for Nuclear Problems, Minsk, Belarus

V. Chekhovsky, A. Litomin, V. Makarenko

Universiteit Antwerpen, Antwerpen, Belgium

M.R. Darwish[2], E.A. De Wolf, T. Janssen, T. Kello[3], A. Lelek, H. Rejeb Sfar, P. Van Mechelen, S. Van Putte, N. Van Remortel

Vrije Universiteit Brussel, Brussel, Belgium

F. Blekman, E.S. Bols, J. D'Hondt, M. Delcourt, H. El Faham, S. Lowette, S. Moortgat, A. Morton, D. Müller, A.R. Sahasransu, S. Tavernier, W. Van Doninck, P. Van Mulders

Université Libre de Bruxelles, Bruxelles, Belgium

D. Beghin, B. Bilin, B. Clerbaux, G. De Lentdecker, L. Favart, A. Grebenyuk, A.K. Kalsi, K. Lee, M. Mahdavikhorrami, I. Makarenko, L. Moureaux, L. Pétré, A. Popov, N. Postiau, E. Starling, L. Thomas, M. Vanden Bemden, C. Vander Velde, P. Vanlaer, L. Wezenbeek

Ghent University, Ghent, Belgium

T. Cornelis, D. Dobur, J. Knolle, L. Lambrecht, G. Mestdach, M. Niedziela, C. Roskas, A. Samalan, K. Skovpen, M. Tytgat, B. Vermassen, M. Vit

Université Catholique de Louvain, Louvain-la-Neuve, Belgium

A. Benecke, A. Bethani, G. Bruno, F. Bury, C. Caputo, P. David, C. Delaere, I.S. Donertas, A. Giammanco, K. Jaffel, Sa. Jain, V. Lemaitre, K. Mondal, J. Prisciandaro, A. Taliercio, M. Teklishyn, T.T. Tran, P. Vischia, S. Wertz

Centro Brasileiro de Pesquisas Fisicas, Rio de Janeiro, Brazil

G.A. Alves, C. Hensel, A. Moraes

Universidade do Estado do Rio de Janeiro, Rio de Janeiro, Brazil

W.L. Aldá Júnior, M. Alves Gallo Pereira, M. Barroso Ferreira Filho, H. Brandao Malbouisson, W. Carvalho, J. Chinellato[4], E.M. Da Costa, G.G. Da Silveira[5], D. De Jesus Damiao, S. Fonseca De Souza, D. Matos Figueiredo, C. Mora Herrera, K. Mota Amarilo, L. Mundim, H. Nogima, P. Rebello Teles, A. Santoro, S.M. Silva Do Amaral, A. Sznajder, M. Thiel, F. Torres Da Silva De Araujo, A. Vilela Pereira

Universidade Estadual Paulista ^{a}, Universidade Federal do ABC ^{b}, São Paulo, Brazil

C.A. Bernardes[a,a,5], L. Calligaris[a], T.R. Fernandez Perez Tomei[a], E.M. Gregores[a,b], D.S. Lemos[a], P.G. Mercadante[a,b], S.F. Novaes[a], Sandra S. Padula[a]

Institute for Nuclear Research and Nuclear Energy, Bulgarian Academy of Sciences, Sofia, Bulgaria

A. Aleksandrov, G. Antchev, R. Hadjiiska, P. Iaydjiev, M. Misheva, M. Rodozov, M. Shopova, G. Sultanov

University of Sofia, Sofia, Bulgaria

A. Dimitrov, T. Ivanov, L. Litov, B. Pavlov, P. Petkov, A. Petrov

Beihang University, Beijing, China

T. Cheng, T. Javaid[6], M. Mittal, L. Yuan

Department of Physics, Tsinghua University

M. Ahmad, G. Bauer, C. Dozen[7], Z. Hu, J. Martins[8], Y. Wang, K. Yi[9,10]

Institute of High Energy Physics, Beijing, China

E. Chapon, G.M. Chen[6], H.S. Chen[6], M. Chen, F. Iemmi, A. Kapoor, D. Leggat, H. Liao, Z.-A. Liu[6], V. Milosevic, F. Monti, R. Sharma, J. Tao, J. Thomas-wilsker, J. Wang, H. Zhang, J. Zhao

State Key Laboratory of Nuclear Physics and Technology, Peking University, Beijing, China

A. Agapitos, Y. An, Y. Ban, C. Chen, A. Levin, Q. Li, X. Lyu, Y. Mao, S.J. Qian, D. Wang, Q. Wang, J. Xiao

Sun Yat-Sen University, Guangzhou, China

M. Lu, Z. You

Institute of Modern Physics and Key Laboratory of Nuclear Physics and Ion-beam Application (MOE) - Fudan University, Shanghai, China

X. Gao[3], H. Okawa

Zhejiang University, Hangzhou, China

Z. Lin, M. Xiao

Universidad de Los Andes, Bogota, Colombia

C. Avila, A. Cabrera, C. Florez, J. Fraga

Universidad de Antioquia, Medellin, Colombia

J. Mejia Guisao, F. Ramirez, J.D. Ruiz Alvarez, C.A. Salazar González

University of Split, Faculty of Electrical Engineering, Mechanical Engineering and Naval Architecture, Split, Croatia

D. Giljanovic, N. Godinovic, D. Lelas, I. Puljak

University of Split, Faculty of Science, Split, Croatia
Z. Antunovic, M. Kovac, T. Sculac

Institute Rudjer Boskovic, Zagreb, Croatia
V. Brigljevic, D. Ferencek, D. Majumder, M. Roguljic, A. Starodumov[11], T. Susa

University of Cyprus, Nicosia, Cyprus
A. Attikis, K. Christoforou, E. Erodotou, A. Ioannou, G. Kole, M. Kolosova, S. Konstantinou, J. Mousa, C. Nicolaou, F. Ptochos, P.A. Razis, H. Rykaczewski, H. Saka

Charles University, Prague, Czech Republic
M. Finger[12], M. Finger Jr.[12], A. Kveton

Escuela Politecnica Nacional, Quito, Ecuador
E. Ayala

Universidad San Francisco de Quito, Quito, Ecuador
E. Carrera Jarrin

Academy of Scientific Research and Technology of the Arab Republic of Egypt, Egyptian Network of High Energy Physics, Cairo, Egypt
A. Ellithi Kamel[13], E. Salama[14,15]

Center for High Energy Physics (CHEP-FU), Fayoum University, El-Fayoum, Egypt
A. Lotfy, M.A. Mahmoud

National Institute of Chemical Physics and Biophysics, Tallinn, Estonia
S. Bhowmik, R.K. Dewanjee, K. Ehataht, M. Kadastik, S. Nandan, C. Nielsen, J. Pata, M. Raidal, L. Tani, C. Veelken

Department of Physics, University of Helsinki, Helsinki, Finland
P. Eerola, L. Forthomme, H. Kirschenmann, K. Osterberg, M. Voutilainen

Helsinki Institute of Physics, Helsinki, Finland
S. Bharthuar, E. Brücken, F. Garcia, J. Havukainen, M.S. Kim, R. Kinnunen, T. Lampén, K. Lassila-Perini, S. Lehti, T. Lindén, M. Lotti, L. Martikainen, M. Myllymäki, J. Ott, H. Siikonen, E. Tuominen, J. Tuominiemi

Lappeenranta University of Technology, Lappeenranta, Finland
P. Luukka, H. Petrow, T. Tuuva

IRFU, CEA, Université Paris-Saclay, Gif-sur-Yvette, France
C. Amendola, M. Besancon, F. Couderc, M. Dejardin, D. Denegri, J.L. Faure, F. Ferri, S. Ganjour, A. Givernaud, P. Gras, G. Hamel de Monchenault, P. Jarry, B. Lenzi, E. Locci, J. Malcles, J. Rander, A. Rosowsky, M.Ö. Sahin, A. Savoy-Navarro[16], M. Titov, G.B. Yu

Laboratoire Leprince-Ringuet, CNRS/IN2P3, Ecole Polytechnique, Institut Polytechnique de Paris, Palaiseau, France
S. Ahuja, F. Beaudette, M. Bonanomi, A. Buchot Perraguin, P. Busson, A. Cappati, C. Charlot, O. Davignon, B. Diab, G. Falmagne, S. Ghosh, R. Granier de Cassagnac,

A. Hakimi, I. Kucher, J. Motta, M. Nguyen, C. Ochando, P. Paganini, J. Rembser, R. Salerno, U. Sarkar, J.B. Sauvan, Y. Sirois, A. Tarabini, A. Zabi, A. Zghiche

Université de Strasbourg, CNRS, IPHC UMR 7178, Strasbourg, France
J.-L. Agram[17], J. Andrea, D. Apparu, D. Bloch, G. Bourgatte, J.-M. Brom, E.C. Chabert, C. Collard, D. Darej, J.-C. Fontaine[17], U. Goerlach, C. Grimault, A.-C. Le Bihan, E. Nibigira, P. Van Hove

Institut de Physique des 2 Infinis de Lyon (IP2I), Villeurbanne, France
E. Asilar, S. Beauceron, C. Bernet, G. Boudoul, C. Camen, A. Carle, N. Chanon, D. Contardo, P. Depasse, H. El Mamouni, J. Fay, S. Gascon, M. Gouzevitch, B. Ille, I.B. Laktineh, H. Lattaud, A. Lesauvage, M. Lethuillier, L. Mirabito, S. Perries, K. Shchablo, V. Sordini, L. Torterotot, G. Touquet, M. Vander Donckt, S. Viret

Georgian Technical University, Tbilisi, Georgia
I. Bagaturia[18], I. Lomidze, Z. Tsamalaidze[12]

RWTH Aachen University, I. Physikalisches Institut, Aachen, Germany
V. Botta, L. Feld, K. Klein, M. Lipinski, D. Meuser, A. Pauls, N. Röwert, J. Schulz, M. Teroerde

RWTH Aachen University, III. Physikalisches Institut A, Aachen, Germany
A. Dodonova, D. Eliseev, M. Erdmann, P. Fackeldey, B. Fischer, S. Ghosh, T. Hebbeker, K. Hoepfner, F. Ivone, L. Mastrolorenzo, M. Merschmeyer, A. Meyer, G. Mocellin, S. Mondal, S. Mukherjee, D. Noll, A. Novak, T. Pook, A. Pozdnyakov, Y. Rath, H. Reithler, J. Roemer, A. Schmidt, S.C. Schuler, A. Sharma, L. Vigilante, S. Wiedenbeck, S. Zaleski

RWTH Aachen University, III. Physikalisches Institut B, Aachen, Germany
C. Dziwok, G. Flügge, W. Haj Ahmad[19], O. Hlushchenko, T. Kress, A. Nowack, C. Pistone, O. Pooth, D. Roy, H. Sert, A. Stahl[20], T. Ziemons, A. Zotz

Deutsches Elektronen-Synchrotron, Hamburg, Germany
H. Aarup Petersen, M. Aldaya Martin, P. Asmuss, S. Baxter, M. Bayatmakou, O. Behnke, A. Bermúdez Martínez, S. Bhattacharya, A.A. Bin Anuar, K. Borras[21], D. Brunner, A. Campbell, A. Cardini, C. Cheng, F. Colombina, S. Consuegra Rodríguez, G. Correia Silva, V. Danilov, M. De Silva, L. Didukh, G. Eckerlin, D. Eckstein, L.I. Estevez Banos, O. Filatov, E. Gallo[22], A. Geiser, A. Giraldi, A. Grohsjean, M. Guthoff, A. Jafari[23], N.Z. Jomhari, H. Jung, A. Kasem[21], M. Kasemann, H. Kaveh, C. Kleinwort, D. Krücker, W. Lange, J. Lidrych, K. Lipka, W. Lohmann[24], R. Mankel, I.-A. Melzer-Pellmann, M. Mendizabal Morentin, J. Metwally, A.B. Meyer, M. Meyer, J. Mnich, A. Mussgiller, Y. Otarid, D. Pérez Adán, D. Pitzl, A. Raspereza, B. Ribeiro Lopes, J. Rübenach, A. Saggio, A. Saibel, M. Savitskyi, M. Scham[25], V. Scheurer, P. Schütze, C. Schwanenberger[22], A. Singh, R.E. Sosa Ricardo, D. Stafford, N. Tonon, M. Van De Klundert, R. Walsh, D. Walter, Y. Wen, K. Wichmann, L. Wiens, C. Wissing, S. Wuchterl

University of Hamburg, Hamburg, Germany
R. Aggleton, S. Albrecht, S. Bein, L. Benato, P. Connor, K. De Leo, M. Eich, F. Feindt, A. Fröhlich, C. Garbers, E. Garutti, P. Gunnellini, M. Hajheidari, J. Haller, A. Hinzmann,

G. Kasieczka, R. Klanner, R. Kogler, T. Kramer, V. Kutzner, J. Lange, T. Lange, A. Lobanov, A. Malara, A. Nigamova, K.J. Pena Rodriguez, O. Rieger, P. Schleper, M. Schröder, J. Schwandt, J. Sonneveld, H. Stadie, G. Steinbrück, A. Tews, I. Zoi

Karlsruher Institut fuer Technologie, Karlsruhe, Germany

J. Bechtel, S. Brommer, E. Butz, R. Caspart, T. Chwalek, W. De Boer[†], A. Dierlamm, A. Droll, K. El Morabit, N. Faltermann, M. Giffels, J.o. Gosewisch, A. Gottmann, F. Hartmann[20], C. Heidecker, U. Husemann, P. Keicher, R. Koppenhöfer, S. Maier, M. Metzler, S. Mitra, Th. Müller, M. Neukum, A. Nürnberg, G. Quast, K. Rabbertz, J. Rauser, D. Savoiu, M. Schnepf, D. Seith, I. Shvetsov, H.J. Simonis, R. Ulrich, J. Van Der Linden, R.F. Von Cube, M. Wassmer, M. Weber, S. Wieland, R. Wolf, S. Wozniewski, S. Wunsch

Institute of Nuclear and Particle Physics (INPP), NCSR Demokritos, Aghia Paraskevi, Greece

G. Anagnostou, G. Daskalakis, T. Geralis, A. Kyriakis, D. Loukas, A. Stakia

National and Kapodistrian University of Athens, Athens, Greece

M. Diamantopoulou, D. Karasavvas, G. Karathanasis, P. Kontaxakis, C.K. Koraka, A. Manousakis-Katsikakis, A. Panagiotou, I. Papavergou, N. Saoulidou, K. Theofilatos, E. Tziaferi, K. Vellidis, E. Vourliotis

National Technical University of Athens, Athens, Greece

G. Bakas, K. Kousouris, I. Papakrivopoulos, G. Tsipolitis, A. Zacharopoulou

University of Ioánnina, Ioánnina, Greece

K. Adamidis, I. Bestintzanos, I. Evangelou, C. Foudas, P. Gianneios, P. Katsoulis, P. Kokkas, N. Manthos, I. Papadopoulos, J. Strologas

MTA-ELTE Lendület CMS Particle and Nuclear Physics Group, Eötvös Loránd University

M. Csanad, K. Farkas, M.M.A. Gadallah[26], S. Lökös[27], P. Major, K. Mandal, A. Mehta, G. Pasztor, A.J. Rádl, O. Surányi, G.I. Veres

Wigner Research Centre for Physics, Budapest, Hungary

M. Bartók[28], G. Bencze, C. Hajdu, D. Horvath[29], F. Sikler, V. Veszpremi, G. Vesztergombi[†]

Institute of Nuclear Research ATOMKI, Debrecen, Hungary

S. Czellar, J. Karancsi[28], J. Molnar, Z. Szillasi, D. Teyssier

Institute of Physics, University of Debrecen

P. Raics, Z.L. Trocsanyi[30], B. Ujvari

Karoly Robert Campus, MATE Institute of Technology

T. Csorgo[31], F. Nemes[31], T. Novak

Indian Institute of Science (IISc), Bangalore, India

J.R. Komaragiri, D. Kumar, L. Panwar, P.C. Tiwari

National Institute of Science Education and Research, HBNI, Bhubaneswar, India

S. Bahinipati[32], C. Kar, P. Mal, T. Mishra, V.K. Muraleedharan Nair Bindhu[33], A. Nayak[33], P. Saha, N. Sur, S.K. Swain, D. Vats[33]

Panjab University, Chandigarh, India

S. Bansal, S.B. Beri, V. Bhatnagar, G. Chaudhary, S. Chauhan, N. Dhingra[34], R. Gupta, A. Kaur, M. Kaur, S. Kaur, P. Kumari, M. Meena, K. Sandeep, J.B. Singh, A.K. Virdi

University of Delhi, Delhi, India

A. Ahmed, A. Bhardwaj, B.C. Choudhary, M. Gola, S. Keshri, A. Kumar, M. Naimuddin, P. Priyanka, K. Ranjan, A. Shah

Saha Institute of Nuclear Physics, HBNI, Kolkata, India

M. Bharti[35], R. Bhattacharya, S. Bhattacharya, D. Bhowmik, S. Dutta, S. Dutta, B. Gomber[36], M. Maity[37], P. Palit, P.K. Rout, G. Saha, B. Sahu, S. Sarkar, M. Sharan, B. Singh[35], S. Thakur[35]

Indian Institute of Technology Madras, Madras, India

P.K. Behera, S.C. Behera, P. Kalbhor, A. Muhammad, R. Pradhan, P.R. Pujahari, A. Sharma, A.K. Sikdar

Bhabha Atomic Research Centre, Mumbai, India

D. Dutta, V. Jha, V. Kumar, D.K. Mishra, K. Naskar[38], P.K. Netrakanti, L.M. Pant, P. Shukla

Tata Institute of Fundamental Research-A, Mumbai, India

T. Aziz, S. Dugad, M. Kumar

Tata Institute of Fundamental Research-B, Mumbai, India

S. Banerjee, R. Chudasama, M. Guchait, S. Karmakar, S. Kumar, G. Majumder, K. Mazumdar, S. Mukherjee

Indian Institute of Science Education and Research (IISER), Pune, India

K. Alpana, S. Dube, B. Kansal, A. Laha, S. Pandey, A. Rane, A. Rastogi, S. Sharma

Isfahan University of Technology, Isfahan, Iran

H. Bakhshiansohi[39], E. Khazaie, M. Zeinali[40]

Institute for Research in Fundamental Sciences (IPM), Tehran, Iran

S. Chenarani[41], S.M. Etesami, M. Khakzad, M. Mohammadi Najafabadi

University College Dublin, Dublin, Ireland

M. Grunewald

INFN Sezione di Bari [a], Università di Bari [b], Politecnico di Bari [c], Bari, Italy

M. Abbrescia[a,b], R. Aly[a,b,42], C. Aruta[a,b], A. Colaleo[a], D. Creanza[a,c], N. De Filippis[a,c], M. De Palma[a,b], A. Di Florio[a,b], A. Di Pilato[a,b], W. Elmetenawee[a,b], L. Fiore[a], A. Gelmi[a,b], M. Gul[a], G. Iaselli[a,c], M. Ince[a,b], S. Lezki[a,b], G. Maggi[a,c], M. Maggi[a], I. Margjeka[a,b],

V. Mastrapasqua[a,b], J.A. Merlin[a], S. My[a,b], S. Nuzzo[a,b], A. Pellecchia[a,b], A. Pompili[a,b], G. Pugliese[a,c], D. Ramos, A. Ranieri[a], G. Selvaggi[a,b], L. Silvestris[a], F.M. Simone[a,b], R. Venditti[a], P. Verwilligen[a]

INFN Sezione di Bologna [a], Università di Bologna [b], Bologna, Italy

G. Abbiendi[a], C. Battilana[a,b], D. Bonacorsi[a,b], L. Borgonovi[a], L. Brigliadori[a], R. Campanini[a,b], P. Capiluppi[a,b], A. Castro[a,b], F.R. Cavallo[a], M. Cuffiani[a,b], G.M. Dallavalle[a], T. Diotalevi[a,b], F. Fabbri[a], A. Fanfani[a,b], P. Giacomelli[a], L. Giommi[a,b], C. Grandi[a], L. Guiducci[a,b], S. Lo Meo[a,43], L. Lunerti[a,b], S. Marcellini[a], G. Masetti[a], F.L. Navarria[a,b], A. Perrotta[a], F. Primavera[a,b], A.M. Rossi[a,b], T. Rovelli[a,b], G.P. Siroli[a,b]

INFN Sezione di Catania [a], Università di Catania [b], Catania, Italy

S. Albergo[a,b,44], S. Costa[a,b,44], A. Di Mattia[a], R. Potenza[a,b], A. Tricomi[a,b,44], C. Tuve[a,b]

INFN Sezione di Firenze [a], Università di Firenze [b], Firenze, Italy

G. Barbagli[a], A. Cassese[a], R. Ceccarelli[a,b], V. Ciulli[a,b], C. Civinini[a], R. D'Alessandro[a,b], E. Focardi[a,b], G. Latino[a,b], P. Lenzi[a,b], M. Lizzo[a,b], M. Meschini[a], S. Paoletti[a], R. Seidita[a,b], G. Sguazzoni[a], L. Viliani[a]

INFN Laboratori Nazionali di Frascati, Frascati, Italy

L. Benussi, S. Bianco, D. Piccolo

INFN Sezione di Genova [a], Università di Genova [b], Genova, Italy

M. Bozzo[a,b], F. Ferro[a], R. Mulargia[a,b], E. Robutti[a], S. Tosi[a,b]

INFN Sezione di Milano-Bicocca [a], Università di Milano-Bicocca [b], Milano, Italy

A. Benaglia[a], G. Boldrini, F. Brivio[a,b], F. Cetorelli[a,b], F. De Guio[a,b], M.E. Dinardo[a,b], P. Dini[a], S. Gennai[a], A. Ghezzi[a,b], P. Govoni[a,b], L. Guzzi[a,b], M.T. Lucchini[a,b], M. Malberti[a], S. Malvezzi[a], A. Massironi[a], D. Menasce[a], L. Moroni[a], M. Paganoni[a,b], D. Pedrini[a], B.S. Pinolini, S. Ragazzi[a,b], N. Redaelli[a], T. Tabarelli de Fatis[a,b], D. Valsecchi[a,b,20], D. Zuolo[a,b]

INFN Sezione di Napoli [a], Università di Napoli 'Federico II' [b], Napoli, Italy, Università della Basilicata [c], Potenza, Italy, Università G. Marconi [d], Roma, Italy

S. Buontempo[a], F. Carnevali[a,b], N. Cavallo[a,c], A. De Iorio[a,b], F. Fabozzi[a,c], A.O.M. Iorio[a,b], L. Lista[a,b], S. Meola[a,d,20], P. Paolucci[a,20], B. Rossi[a], C. Sciacca[a,b]

INFN Sezione di Padova [a], Università di Padova [b], Padova, Italy, Università di Trento [c], Trento, Italy

P. Azzi[a], N. Bacchetta[a], D. Bisello[a,b], P. Bortignon[a], A. Bragagnolo[a,b], R. Carlin[a,b], P. Checchia[a], T. Dorigo[a], U. Dosselli[a], F. Gasparini[a,b], U. Gasparini[a,b], G. Grosso, S.Y. Hoh[a,b], L. Layer[a,45], E. Lusiani, M. Margoni[a,b], A.T. Meneguzzo[a,b], J. Pazzini[a,b], M. Presilla[a,b], P. Ronchese[a,b], R. Rossin[a,b], F. Simonetto[a,b], G. Strong[a], M. Tosi[a,b], H. Yarar[a,b], M. Zanetti[a,b], P. Zotto[a,b], A. Zucchetta[a,b], G. Zumerle[a,b]

INFN Sezione di Pavia ^{a}, Università di Pavia ^{b}

C. Aime'^{a,b}, A. Braghieri^a, S. Calzaferri^{a,b}, D. Fiorina^{a,b}, P. Montagna^{a,b}, S.P. Ratti^{a,b}, V. Re^a, C. Riccardi^{a,b}, P. Salvini^a, I. Vai^a, P. Vitulo^{a,b}

INFN Sezione di Perugia ^{a}, Università di Perugia ^{b}, Perugia, Italy

P. Asenov^{a,46}, G.M. Bilei^a, D. Ciangottini^{a,b}, L. Fanò^{a,b}, P. Lariccia^{a,b}, M. Magherini^b, G. Mantovani^{a,b}, V. Mariani^{a,b}, M. Menichelli^a, F. Moscatelli^{a,46}, A. Piccinelli^{a,b}, A. Rossi^{a,b}, A. Santocchia^{a,b}, D. Spiga^a, T. Tedeschi^{a,b}

INFN Sezione di Pisa ^{a}, Università di Pisa ^{b}, Scuola Normale Superiore di Pisa ^{c}, Pisa Italy, Università di Siena ^{d}, Siena, Italy

P. Azzurri^a, G. Bagliesi^a, V. Bertacchi^{a,c}, L. Bianchini^a, T. Boccali^a, E. Bossini^{a,b}, R. Castaldi^a, M.A. Ciocci^{a,b}, V. D'Amante^{a,d}, R. Dell'Orso^a, M.R. Di Domenico^{a,d}, S. Donato^a, A. Giassi^a, F. Ligabue^{a,c}, E. Manca^{a,c}, G. Mandorli^{a,c}, A. Messineo^{a,b}, F. Palla^a, S. Parolia^{a,b}, G. Ramirez-Sanchez^{a,c}, A. Rizzi^{a,b}, G. Rolandi^{a,c}, S. Roy Chowdhury^{a,c}, A. Scribano^a, N. Shafiei^{a,b}, P. Spagnolo^a, R. Tenchini^a, G. Tonelli^{a,b}, N. Turini^{a,d}, A. Venturi^a, P.G. Verdini^a

INFN Sezione di Roma ^{a}, Sapienza Università di Roma ^{b}, Rome, Italy

P. Barria^a, M. Campana^{a,b}, F. Cavallari^a, D. Del Re^{a,b}, E. Di Marco^a, M. Diemoz^a, E. Longo^{a,b}, P. Meridiani^a, G. Organtini^{a,b}, F. Pandolfi^a, R. Paramatti^{a,b}, C. Quaranta^{a,b}, S. Rahatlou^{a,b}, C. Rovelli^a, F. Santanastasio^{a,b}, L. Soffi^a, R. Tramontano^{a,b}

INFN Sezione di Torino ^{a}, Università di Torino ^{b}, Torino, Italy, Università del Piemonte Orientale ^{c}, Novara, Italy

N. Amapane^{a,b}, R. Arcidiacono^{a,c}, S. Argiro^{a,b}, M. Arneodo^{a,c}, N. Bartosik^a, R. Bellan^{a,b}, A. Bellora^{a,b}, J. Berenguer Antequera^{a,b}, C. Biino^a, N. Cartiglia^a, S. Cometti^a, M. Costa^{a,b}, R. Covarelli^{a,b}, N. Demaria^a, B. Kiani^{a,b}, F. Legger^a, C. Mariotti^a, S. Maselli^a, E. Migliore^{a,b}, E. Monteil^{a,b}, M. Monteno^a, M.M. Obertino^{a,b}, G. Ortona^a, L. Pacher^{a,b}, N. Pastrone^a, M. Pelliccioni^a, G.L. Pinna Angioni^{a,b}, M. Ruspa^{a,c}, K. Shchelina^a, F. Siviero^{a,b}, V. Sola^a, A. Solano^{a,b}, D. Soldi^{a,b}, A. Staiano^a, M. Tornago^{a,b}, D. Trocino^a, A. Vagnerini^{a,b}

INFN Sezione di Trieste ^{a}, Università di Trieste ^{b}, Trieste, Italy

S. Belforte^a, V. Candelise^{a,b}, M. Casarsa^a, F. Cossutti^a, A. Da Rold^{a,b}, G. Della Ricca^{a,b}, G. Sorrentino^{a,b}, F. Vazzoler^{a,b}

Kyungpook National University, Daegu, Korea

S. Dogra, C. Huh, B. Kim, D.H. Kim, G.N. Kim, J. Kim, J. Lee, S.W. Lee, C.S. Moon, Y.D. Oh, S.I. Pak, B.C. Radburn-Smith, S. Sekmen, Y.C. Yang

Chonnam National University, Institute for Universe and Elementary Particles, Kwangju, Korea

H. Kim, D.H. Moon

Hanyang University, Seoul, Korea

B. Francois, T.J. Kim, J. Park

Korea University, Seoul, Korea

S. Cho, S. Choi, Y. Go, B. Hong, K. Lee, K.S. Lee, J. Lim, J. Park, S.K. Park, J. Yoo

Kyung Hee University, Department of Physics, Seoul, Republic of Korea

J. Goh, A. Gurtu

Sejong University, Seoul, Korea

H.S. Kim, Y. Kim

Seoul National University, Seoul, Korea

J. Almond, J.H. Bhyun, J. Choi, S. Jeon, J. Kim, J.S. Kim, S. Ko, H. Kwon, H. Lee, S. Lee, B.H. Oh, M. Oh, S.B. Oh, H. Seo, U.K. Yang, I. Yoon

University of Seoul, Seoul, Korea

W. Jang, D.Y. Kang, Y. Kang, S. Kim, B. Ko, J.S.H. Lee, Y. Lee, I.C. Park, Y. Roh, M.S. Ryu, D. Song, I.J. Watson, S. Yang

Yonsei University, Department of Physics, Seoul, Korea

S. Ha, H.D. Yoo

Sungkyunkwan University, Suwon, Korea

M. Choi, H. Lee, Y. Lee, I. Yu

College of Engineering and Technology, American University of the Middle East (AUM), Egaila, Kuwait

T. Beyrouthy, Y. Maghrbi

Riga Technical University

T. Torims, V. Veckalns[47]

Vilnius University, Vilnius, Lithuania

M. Ambrozas, A. Carvalho Antunes De Oliveira, A. Juodagalvis, A. Rinkevicius, G. Tamulaitis

National Centre for Particle Physics, Universiti Malaya, Kuala Lumpur, Malaysia

N. Bin Norjoharuddeen, W.A.T. Wan Abdullah, M.N. Yusli, Z. Zolkapli

Universidad de Sonora (UNISON), Hermosillo, Mexico

J.F. Benitez, A. Castaneda Hernandez, M. León Coello, J.A. Murillo Quijada, A. Sehrawat, L. Valencia Palomo

Centro de Investigacion y de Estudios Avanzados del IPN, Mexico City, Mexico

G. Ayala, H. Castilla-Valdez, E. De La Cruz-Burelo, I. Heredia-De La Cruz[48], R. Lopez-Fernandez, C.A. Mondragon Herrera, D.A. Perez Navarro, A. Sanchez-Hernandez

Universidad Iberoamericana, Mexico City, Mexico

S. Carrillo Moreno, C. Oropeza Barrera, F. Vazquez Valencia

Benemerita Universidad Autonoma de Puebla, Puebla, Mexico

I. Pedraza, H.A. Salazar Ibarguen, C. Uribe Estrada

University of Montenegro, Podgorica, Montenegro

J. Mijuskovic[49], N. Raicevic

University of Auckland, Auckland, New Zealand

D. Krofcheck

University of Canterbury, Christchurch, New Zealand

P.H. Butler

National Centre for Physics, Quaid-I-Azam University, Islamabad, Pakistan

A. Ahmad, M.I. Asghar, A. Awais, M.I.M. Awan, H.R. Hoorani, W.A. Khan, M.A. Shah, M. Shoaib, M. Waqas

AGH University of Science and Technology Faculty of Computer Science, Electronics and Telecommunications, Krakow, Poland

V. Avati, L. Grzanka, M. Malawski

National Centre for Nuclear Research, Swierk, Poland

H. Bialkowska, M. Bluj, B. Boimska, M. Górski, M. Kazana, M. Szleper, P. Zalewski

Institute of Experimental Physics, Faculty of Physics, University of Warsaw, Warsaw, Poland

K. Bunkowski, K. Doroba, A. Kalinowski, M. Konecki, J. Krolikowski, M. Walczak

Laboratório de Instrumentação e Física Experimental de Partículas, Lisboa, Portugal

M. Araujo, P. Bargassa, D. Bastos, A. Boletti, P. Faccioli, M. Gallinaro, J. Hollar, N. Leonardo, T. Niknejad, M. Pisano, J. Seixas, O. Toldaiev, J. Varela

Joint Institute for Nuclear Research, Dubna, Russia

S. Afanasiev, D. Budkouski, I. Golutvin, I. Gorbunov, V. Karjavine, V. Korenkov, A. Lanev, A. Malakhov, V. Matveev[50,51], V. Palichik, V. Perelygin, M. Savina, D. Seitova, V. Shalaev, S. Shmatov, S. Shulha, V. Smirnov, O. Teryaev, N. Voytishin, B.S. Yuldashev[52], A. Zarubin, I. Zhizhin

Petersburg Nuclear Physics Institute, Gatchina (St. Petersburg), Russia

G. Gavrilov, V. Golovtcov, Y. Ivanov, V. Kim[53], E. Kuznetsova[54], V. Murzin, V. Oreshkin, I. Smirnov, D. Sosnov, V. Sulimov, L. Uvarov, S. Volkov, A. Vorobyev

Institute for Nuclear Research, Moscow, Russia

Yu. Andreev, A. Dermenev, S. Gninenko, N. Golubev, A. Karneyeu, D. Kirpichnikov, M. Kirsanov, N. Krasnikov, A. Pashenkov, G. Pivovarov, A. Toropin

Institute for Theoretical and Experimental Physics named by A.I. Alikhanov of NRC 'Kurchatov Institute', Moscow, Russia

V. Epshteyn, V. Gavrilov, N. Lychkovskaya, A. Nikitenko[55], V. Popov, A. Stepennov, M. Toms, E. Vlasov, A. Zhokin

Moscow Institute of Physics and Technology, Moscow, Russia

T. Aushev

National Research Nuclear University 'Moscow Engineering Physics Institute' (MEPhI), Moscow, Russia

M. Chadeeva[56], A. Oskin, P. Parygin, E. Popova, D. Selivanova, E. Zhemchugov[56]

P.N. Lebedev Physical Institute, Moscow, Russia

V. Andreev, M. Azarkin, I. Dremin, M. Kirakosyan, A. Terkulov

Skobeltsyn Institute of Nuclear Physics, Lomonosov Moscow State University, Moscow, Russia

A. Belyaev, E. Boos, V. Bunichev, M. Dubinin[57], L. Dudko, A. Ershov, A. Gribushin, V. Klyukhin, O. Kodolova, I. Lokhtin, S. Obraztsov, S. Petrushanko, V. Savrin

Novosibirsk State University (NSU), Novosibirsk, Russia

V. Blinov[58], T. Dimova[58], L. Kardapoltsev[58], A. Kozyrev[58], I. Ovtin[58], Y. Skovpen[58]

Institute for High Energy Physics of National Research Centre 'Kurchatov Institute', Protvino, Russia

I. Azhgirey, I. Bayshev, D. Elumakhov, V. Kachanov, D. Konstantinov, P. Mandrik, V. Petrov, R. Ryutin, S. Slabospitskii, A. Sobol, S. Troshin, N. Tyurin, A. Uzunian, A. Volkov

National Research Tomsk Polytechnic University, Tomsk, Russia

A. Babaev, V. Okhotnikov

Tomsk State University, Tomsk, Russia

V. Borshch, V. Ivanchenko, E. Tcherniaev

University of Belgrade: Faculty of Physics and VINCA Institute of Nuclear Sciences, Belgrade, Serbia

P. Adzic[59], M. Dordevic, P. Milenovic, J. Milosevic

Centro de Investigaciones Energéticas Medioambientales y Tecnológicas (CIEMAT), Madrid, Spain

M. Aguilar-Benitez, J. Alcaraz Maestre, A. Álvarez Fernández, I. Bachiller, M. Barrio Luna, Cristina F. Bedoya, C.A. Carrillo Montoya, M. Cepeda, M. Cerrada, N. Colino, B. De La Cruz, A. Delgado Peris, J.P. Fernández Ramos, J. Flix, M.C. Fouz, O. Gonzalez Lopez, S. Goy Lopez, J.M. Hernandez, M.I. Josa, J. León Holgado, D. Moran, Á. Navarro Tobar, C. Perez Dengra, A. Pérez-Calero Yzquierdo, J. Puerta Pelayo, I. Redondo, L. Romero, S. Sánchez Navas, L. Urda Gómez, C. Willmott

Universidad Autónoma de Madrid, Madrid, Spain

J.F. de Trocóniz, R. Reyes-Almanza

Universidad de Oviedo, Instituto Universitario de Ciencias y Tecnologías Espaciales de Asturias (ICTEA), Oviedo, Spain

B. Alvarez Gonzalez, J. Cuevas, C. Erice, J. Fernandez Menendez, S. Folgueras, I. Gonzalez Caballero, J.R. González Fernández, E. Palencia Cortezon, C. Ramón Álvarez, V. Rodríguez Bouza, A. Soto Rodríguez, A. Trapote, N. Trevisani, C. Vico Villalba

Instituto de Física de Cantabria (IFCA), CSIC-Universidad de Cantabria, Santander, Spain

J.A. Brochero Cifuentes, I.J. Cabrillo, A. Calderon, J. Duarte Campderros, M. Fernandez, C. Fernandez Madrazo, P.J. Fernández Manteca, A. García Alonso, G. Gomez, C. Martinez Rivero, P. Martinez Ruiz del Arbol, F. Matorras, Pablo Matorras-Cuevas, J. Piedra Gomez, C. Prieels, T. Rodrigo, A. Ruiz-Jimeno, L. Scodellaro, I. Vila, J.M. Vizan Garcia

University of Colombo, Colombo, Sri Lanka

M.K. Jayananda, B. Kailasapathy[60], D.U.J. Sonnadara, D.D.C. Wickramarathna

University of Ruhuna, Department of Physics, Matara, Sri Lanka

W.G.D. Dharmaratna, K. Liyanage, N. Perera, N. Wickramage

CERN, European Organization for Nuclear Research, Geneva, Switzerland

T.K. Aarrestad, D. Abbaneo, J. Alimena, E. Auffray, G. Auzinger, J. Baechler, P. Baillon[†], D. Barney, J. Bendavid, M. Bianco, A. Bocci, T. Camporesi, M. Capeans Garrido, G. Cerminara, S.S. Chhibra, M. Cipriani, L. Cristella, D. d'Enterria, A. Dabrowski, A. David, A. De Roeck, M.M. Defranchis, M. Deile, M. Dobson, M. Dünser, N. Dupont, A. Elliott-Peisert, N. Emriskova, F. Fallavollita[61], D. Fasanella, A. Florent, G. Franzoni, W. Funk, S. Giani, D. Gigi, K. Gill, F. Glege, L. Gouskos, M. Haranko, J. Hegeman, V. Innocente, T. James, P. Janot, J. Kaspar, J. Kieseler, M. Komm, N. Kratochwil, C. Lange, S. Laurila, P. Lecoq, A. Lintuluoto, K. Long, C. Lourenço, B. Maier, L. Malgeri, S. Mallios, M. Mannelli, A.C. Marini, F. Meijers, S. Mersi, E. Meschi, F. Moortgat, M. Mulders, S. Orfanelli, L. Orsini, F. Pantaleo, L. Pape, E. Perez, M. Peruzzi, A. Petrilli, G. Petrucciani, A. Pfeiffer, M. Pierini, D. Piparo, M. Pitt, H. Qu, T. Quast, D. Rabady, A. Racz, G. Reales Gutiérrez, M. Rieger, M. Rovere, H. Sakulin, J. Salfeld-Nebgen, S. Scarfi, C. Schäfer, C. Schwick, M. Selvaggi, A. Sharma, P. Silva, W. Snoeys, P. Sphicas[62], S. Summers, K. Tatar, V.R. Tavolaro, D. Treille, P. Tropea, A. Tsirou, G.P. Van Onsem, J. Wanczyk[63], K.A. Wozniak, W.D. Zeuner

Paul Scherrer Institut, Villigen, Switzerland

L. Caminada[64], A. Ebrahimi, W. Erdmann, R. Horisberger, Q. Ingram, H.C. Kaestli, D. Kotlinski, U. Langenegger, M. Missiroli[64], L. Noehte[64], T. Rohe

ETH Zurich - Institute for Particle Physics and Astrophysics (IPA), Zurich, Switzerland

K. Androsov[63], M. Backhaus, P. Berger, A. Calandri, N. Chernyavskaya, A. De Cosa, G. Dissertori, M. Dittmar, M. Donegà, C. Dorfer, F. Eble, K. Gedia, F. Glessgen, T.A. Gómez Espinosa, C. Grab, D. Hits, W. Lustermann, A.-M. Lyon, R.A. Manzoni, L. Marchese, C. Martin Perez, M.T. Meinhard, F. Nessi-Tedaldi, J. Niedziela, F. Pauss, V. Perovic, S. Pigazzini, M.G. Ratti, M. Reichmann, C. Reissel, T. Reitenspiess, B. Ristic, D. Ruini, D.A. Sanz Becerra, V. Stampf, J. Steggemann[63], R. Wallny, D.H. Zhu

Universität Zürich, Zurich, Switzerland

C. Amsler[65], P. Bärtschi, C. Botta, D. Brzhechko, M.F. Canelli, K. Cormier, A. De Wit, R. Del Burgo, J.K. Heikkilä, M. Huwiler, W. Jin, A. Jofrehei, B. Kilminster, S. Leontsinis, S.P. Liechti, A. Macchiolo, P. Meiring, V.M. Mikuni, U. Molinatti, I. Neutelings, A. Reimers, P. Robmann, S. Sanchez Cruz, K. Schweiger, Y. Takahashi

National Central University, Chung-Li, Taiwan

C. Adloff[66], C.M. Kuo, W. Lin, A. Roy, T. Sarkar[37], S.S. Yu

National Taiwan University (NTU), Taipei, Taiwan

L. Ceard, Y. Chao, K.F. Chen, P.H. Chen, W.-S. Hou, Y.y. Li, R.-S. Lu, E. Paganis, A. Psallidas, A. Steen, H.y. Wu, E. Yazgan, P.r. Yu

Chulalongkorn University, Faculty of Science, Department of Physics, Bangkok, Thailand

B. Asavapibhop, C. Asawatangtrakuldee, N. Srimanobhas

Çukurova University, Physics Department, Science and Art Faculty, Adana, Turkey

F. Boran, S. Damarseckin[67], Z.S. Demiroglu, F. Dolek, I. Dumanoglu[68], E. Eskut, Y. Guler[69], E. Gurpinar Guler[69], I. Hos[70], C. Isik, O. Kara, A. Kayis Topaksu, U. Kiminsu, G. Onengut, K. Ozdemir[71], A. Polatoz, A.E. Simsek, B. Tali[72], U.G. Tok, S. Turkcapar, I.S. Zorbakir, C. Zorbilmez

Middle East Technical University, Physics Department, Ankara, Turkey

B. Isildak[73], G. Karapinar[74], K. Ocalan[75], M. Yalvac[76]

Bogazici University, Istanbul, Turkey

B. Akgun, I.O. Atakisi, E. Gülmez, M. Kaya[77], O. Kaya[78], Ö. Özçelik, S. Tekten[79], E.A. Yetkin[80]

Istanbul Technical University, Istanbul, Turkey

A. Cakir, K. Cankocak[68], Y. Komurcu, S. Sen[81]

Istanbul University, Istanbul, Turkey

S. Cerci[72], B. Kaynak, S. Ozkorucuklu, D. Sunar Cerci[72]

Institute for Scintillation Materials of National Academy of Science of Ukraine, Kharkov, Ukraine

B. Grynyov

National Scientific Center, Kharkov Institute of Physics and Technology, Kharkov, Ukraine

L. Levchuk

University of Bristol, Bristol, United Kingdom

D. Anthony, E. Bhal, S. Bologna, J.J. Brooke, A. Bundock, E. Clement, D. Cussans, H. Flacher, J. Goldstein, G.P. Heath, H.F. Heath, L. Kreczko, B. Krikler, S. Paramesvaran, S. Seif El Nasr-Storey, V.J. Smith, N. Stylianou[82], K. Walkingshaw Pass, R. White

Rutherford Appleton Laboratory, Didcot, United Kingdom

K.W. Bell, A. Belyaev[83], C. Brew, R.M. Brown, D.J.A. Cockerill, C. Cooke, K.V. Ellis, K. Harder, S. Harper, M.l. Holmberg[84], J. Linacre, K. Manolopoulos, D.M. Newbold, E. Olaiya, D. Petyt, T. Reis, T. Schuh, C.H. Shepherd-Themistocleous, I.R. Tomalin, T. Williams

Imperial College, London, United Kingdom

R. Bainbridge, P. Bloch, S. Bonomally, J. Borg, S. Breeze, O. Buchmuller, V. Cepaitis, G.S. Chahal[85], D. Colling, P. Dauncey, G. Davies, M. Della Negra, A. Dow, S. Fayer, G. Fedi, G. Hall, M.H. Hassanshahi, G. Iles, J. Langford, L. Lyons, A.-M. Magnan, S. Malik, A. Martelli, D.G. Monk, J. Nash[86], M. Pesaresi, D.M. Raymond, A. Richards, A. Rose, E. Scott, C. Seez, A. Shtipliyski, A. Tapper, K. Uchida, T. Virdee[20], M. Vojinovic, N. Wardle, S.N. Webb, D. Winterbottom

Brunel University, Uxbridge, United Kingdom

K. Coldham, J.E. Cole, A. Khan, P. Kyberd, I.D. Reid, L. Teodorescu, S. Zahid

Baylor University, Waco, U.S.A.

S. Abdullin, A. Brinkerhoff, B. Caraway, J. Dittmann, K. Hatakeyama, A.R. Kanuganti, B. McMaster, N. Pastika, M. Saunders, S. Sawant, C. Sutantawibul, J. Wilson

Catholic University of America, Washington, DC, U.S.A.

R. Bartek, A. Dominguez, R. Uniyal, A.M. Vargas Hernandez

The University of Alabama, Tuscaloosa, U.S.A.

A. Buccilli, S.I. Cooper, D. Di Croce, S.V. Gleyzer, C. Henderson, C.U. Perez, P. Rumerio[87], C. West

Boston University, Boston, U.S.A.

A. Akpinar, A. Albert, D. Arcaro, C. Cosby, Z. Demiragli, E. Fontanesi, D. Gastler, S. May, J. Rohlf, K. Salyer, D. Sperka, D. Spitzbart, I. Suarez, A. Tsatsos, S. Yuan, D. Zou

Brown University, Providence, U.S.A.

G. Benelli, B. Burkle, X. Coubez[21], D. Cutts, M. Hadley, U. Heintz, J.M. Hogan[88], G. Landsberg, K.T. Lau, M. Lukasik, J. Luo, M. Narain, S. Sagir[89], E. Usai, W.Y. Wong, X. Yan, D. Yu, W. Zhang

University of California, Davis, Davis, U.S.A.

J. Bonilla, C. Brainerd, R. Breedon, M. Calderon De La Barca Sanchez, M. Chertok, J. Conway, P.T. Cox, R. Erbacher, G. Haza, F. Jensen, O. Kukral, R. Lander, M. Mulhearn, D. Pellett, B. Regnery, D. Taylor, Y. Yao, F. Zhang

University of California, Los Angeles, U.S.A.

M. Bachtis, R. Cousins, A. Datta, D. Hamilton, J. Hauser, M. Ignatenko, M.A. Iqbal, T. Lam, W.A. Nash, S. Regnard, D. Saltzberg, B. Stone, V. Valuev

University of California, Riverside, Riverside, U.S.A.

K. Burt, Y. Chen, R. Clare, J.W. Gary, M. Gordon, G. Hanson, G. Karapostoli, O.R. Long, N. Manganelli, M. Olmedo Negrete, W. Si, S. Wimpenny, Y. Zhang

University of California, San Diego, La Jolla, U.S.A.

J.G. Branson, P. Chang, S. Cittolin, S. Cooperstein, N. Deelen, D. Diaz, J. Duarte, R. Gerosa, L. Giannini, D. Gilbert, J. Guiang, R. Kansal, V. Krutelyov, R. Lee, J. Letts, M. Masciovecchio, M. Pieri, B.V. Sathia Narayanan, V. Sharma, M. Tadel, A. Vartak, F. Würthwein, Y. Xiang, A. Yagil

University of California, Santa Barbara - Department of Physics, Santa Barbara, U.S.A.

N. Amin, C. Campagnari, M. Citron, A. Dorsett, V. Dutta, J. Incandela, M. Kilpatrick, J. Kim, B. Marsh, H. Mei, M. Oshiro, M. Quinnan, J. Richman, U. Sarica, F. Setti, J. Sheplock, D. Stuart, S. Wang

California Institute of Technology, Pasadena, U.S.A.

A. Bornheim, O. Cerri, I. Dutta, J.M. Lawhorn, N. Lu, J. Mao, H.B. Newman, T.Q. Nguyen, M. Spiropulu, J.R. Vlimant, C. Wang, S. Xie, Z. Zhang, R.Y. Zhu

Carnegie Mellon University, Pittsburgh, U.S.A.

J. Alison, S. An, M.B. Andrews, P. Bryant, T. Ferguson, A. Harilal, C. Liu, T. Mudholkar, M. Paulini, A. Sanchez, W. Terrill

University of Colorado Boulder, Boulder, U.S.A.

J.P. Cumalat, W.T. Ford, A. Hassani, E. MacDonald, R. Patel, A. Perloff, C. Savard, K. Stenson, K.A. Ulmer, S.R. Wagner

Cornell University, Ithaca, U.S.A.

J. Alexander, S. Bright-thonney, Y. Cheng, D.J. Cranshaw, S. Hogan, J. Monroy, J.R. Patterson, D. Quach, J. Reichert, M. Reid, A. Ryd, W. Sun, J. Thom, P. Wittich, R. Zou

Fermi National Accelerator Laboratory, Batavia, U.S.A.

M. Albrow, M. Alyari, G. Apollinari, A. Apresyan, A. Apyan, S. Banerjee, L.A.T. Bauerdick, D. Berry, J. Berryhill, P.C. Bhat, K. Burkett, J.N. Butler, A. Canepa, G.B. Cerati, H.W.K. Cheung, F. Chlebana, M. Cremonesi, K.F. Di Petrillo, V.D. Elvira, Y. Feng, J. Freeman, Z. Gecse, L. Gray, D. Green, S. Grünendahl, O. Gutsche, R.M. Harris, R. Heller, T.C. Herwig, J. Hirschauer, B. Jayatilaka, S. Jindariani, M. Johnson, U. Joshi, T. Klijnsma, B. Klima, K.H.M. Kwok, S. Lammel, D. Lincoln, R. Lipton, T. Liu, C. Madrid, K. Maeshima, C. Mantilla, D. Mason, P. McBride, P. Merkel, S. Mrenna, S. Nahn, J. Ngadiuba, V. O'Dell, V. Papadimitriou, K. Pedro, C. Pena[57], O. Prokofyev, F. Ravera, A. Reinsvold Hall, L. Ristori, E. Sexton-Kennedy, N. Smith, A. Soha, W.J. Spalding, L. Spiegel, S. Stoynev, J. Strait, L. Taylor, S. Tkaczyk, N.V. Tran, L. Uplegger, E.W. Vaandering, H.A. Weber

University of Florida, Gainesville, U.S.A.

D. Acosta, P. Avery, D. Bourilkov, L. Cadamuro, V. Cherepanov, F. Errico, R.D. Field, D. Guerrero, B.M. Joshi, M. Kim, E. Koenig, J. Konigsberg, A. Korytov, K.H. Lo, K. Matchev, N. Menendez, G. Mitselmakher, A. Muthirakalayil Madhu, N. Rawal, D. Rosenzweig, S. Rosenzweig, J. Rotter, K. Shi, J. Sturdy, J. Wang, E. Yigitbasi, X. Zuo

Florida State University, Tallahassee, U.S.A.

T. Adams, A. Askew, R. Habibullah, V. Hagopian, K.F. Johnson, R. Khurana, T. Kolberg, G. Martinez, H. Prosper, C. Schiber, O. Viazlo, R. Yohay, J. Zhang

Florida Institute of Technology, Melbourne, U.S.A.

M.M. Baarmand, S. Butalla, T. Elkafrawy[15], M. Hohlmann, R. Kumar Verma, D. Noonan, M. Rahmani, F. Yumiceva

University of Illinois at Chicago (UIC), Chicago, U.S.A.

M.R. Adams, H. Becerril Gonzalez, R. Cavanaugh, X. Chen, S. Dittmer, O. Evdokimov, C.E. Gerber, D.A. Hangal, D.J. Hofman, A.H. Merrit, C. Mills, G. Oh, T. Roy, S. Rudrabhatla, M.B. Tonjes, N. Varelas, J. Viinikainen, X. Wang, Z. Wu, Z. Ye

The University of Iowa, Iowa City, U.S.A.

M. Alhusseini, K. Dilsiz[90], R.P. Gandrajula, O.K. Köseyan, J.-P. Merlo, A. Mestvirishvili[91], J. Nachtman, H. Ogul[92], Y. Onel, A. Penzo, C. Snyder, E. Tiras[93]

Johns Hopkins University, Baltimore, U.S.A.

O. Amram, B. Blumenfeld, L. Corcodilos, J. Davis, M. Eminizer, A.V. Gritsan, S. Kyriacou, P. Maksimovic, J. Roskes, M. Swartz, T.Á. Vámi

The University of Kansas, Lawrence, U.S.A.

A. Abreu, J. Anguiano, C. Baldenegro Barrera, P. Baringer, A. Bean, A. Bylinkin, Z. Flowers, T. Isidori, S. Khalil, J. King, G. Krintiras, A. Kropivnitskaya, M. Lazarovits, C. Lindsey, J. Marquez, N. Minafra, M. Murray, M. Nickel, C. Rogan, C. Royon, R. Salvatico, S. Sanders, E. Schmitz, C. Smith, J.D. Tapia Takaki, Q. Wang, Z. Warner, J. Williams, G. Wilson

Kansas State University, Manhattan, U.S.A.

S. Duric, A. Ivanov, K. Kaadze, D. Kim, Y. Maravin, T. Mitchell, A. Modak, K. Nam

Lawrence Livermore National Laboratory, Livermore, U.S.A.

F. Rebassoo, D. Wright

University of Maryland, College Park, U.S.A.

E. Adams, A. Baden, O. Baron, A. Belloni, S.C. Eno, N.J. Hadley, S. Jabeen, R.G. Kellogg, T. Koeth, A.C. Mignerey, S. Nabili, C. Palmer, M. Seidel, A. Skuja, L. Wang, K. Wong

Massachusetts Institute of Technology, Cambridge, U.S.A.

D. Abercrombie, G. Andreassi, R. Bi, S. Brandt, W. Busza, I.A. Cali, Y. Chen, M. D'Alfonso, J. Eysermans, C. Freer, G. Gomez Ceballos, M. Goncharov, P. Harris, M. Hu, M. Klute, D. Kovalskyi, J. Krupa, Y.-J. Lee, C. Mironov, C. Paus, D. Rankin, C. Roland, G. Roland, Z. Shi, G.S.F. Stephans, J. Wang, Z. Wang, B. Wyslouch

University of Minnesota, Minneapolis, U.S.A.

R.M. Chatterjee, A. Evans, P. Hansen, J. Hiltbrand, Sh. Jain, M. Krohn, Y. Kubota, J. Mans, M. Revering, R. Rusack, R. Saradhy, N. Schroeder, N. Strobbe, M.A. Wadud

University of Nebraska-Lincoln, Lincoln, U.S.A.

K. Bloom, M. Bryson, S. Chauhan, D.R. Claes, C. Fangmeier, L. Finco, F. Golf, C. Joo, I. Kravchenko, M. Musich, I. Reed, J.E. Siado, G.R. Snow[†], W. Tabb, F. Yan, A.G. Zecchinelli

State University of New York at Buffalo, Buffalo, U.S.A.

G. Agarwal, H. Bandyopadhyay, L. Hay, I. Iashvili, A. Kharchilava, C. McLean, D. Nguyen, J. Pekkanen, S. Rappoccio, A. Williams

Northeastern University, Boston, U.S.A.

G. Alverson, E. Barberis, Y. Haddad, A. Hortiangtham, J. Li, G. Madigan, B. Marzocchi, D.M. Morse, V. Nguyen, T. Orimoto, A. Parker, L. Skinnari, A. Tishelman-Charny, T. Wamorkar, B. Wang, A. Wisecarver, D. Wood

Northwestern University, Evanston, U.S.A.

S. Bhattacharya, J. Bueghly, Z. Chen, A. Gilbert, T. Gunter, K.A. Hahn, Y. Liu, N. Odell, M.H. Schmitt, M. Velasco

University of Notre Dame, Notre Dame, U.S.A.

R. Band, R. Bucci, A. Das, N. Dev, R. Goldouzian, M. Hildreth, K. Hurtado Anampa, C. Jessop, K. Lannon, J. Lawrence, N. Loukas, D. Lutton, N. Marinelli, I. Mcalister, T. McCauley, C. Mcgrady, K. Mohrman, Y. Musienko[50], R. Ruchti, P. Siddireddy, A. Townsend, M. Wayne, A. Wightman, M. Zarucki, L. Zygala

The Ohio State University, Columbus, U.S.A.

B. Bylsma, B. Cardwell, L.S. Durkin, B. Francis, C. Hill, M. Nunez Ornelas, K. Wei, B.L. Winer, B.R. Yates

Princeton University, Princeton, U.S.A.

F.M. Addesa, B. Bonham, P. Das, G. Dezoort, P. Elmer, A. Frankenthal, B. Greenberg, N. Haubrich, S. Higginbotham, A. Kalogeropoulos, G. Kopp, S. Kwan, D. Lange, D. Marlow, K. Mei, I. Ojalvo, J. Olsen, D. Stickland, C. Tully

University of Puerto Rico, Mayaguez, U.S.A.

S. Malik, S. Norberg

Purdue University, West Lafayette, U.S.A.

A.S. Bakshi, V.E. Barnes, R. Chawla, S. Das, L. Gutay, M. Jones, A.W. Jung, S. Karmarkar, D. Kondratyev, M. Liu, G. Negro, N. Neumeister, G. Paspalaki, C.C. Peng, S. Piperov, A. Purohit, J.F. Schulte, M. Stojanovic[16], J. Thieman, F. Wang, R. Xiao, W. Xie

Purdue University Northwest, Hammond, U.S.A.

J. Dolen, N. Parashar

Rice University, Houston, U.S.A.

A. Baty, M. Decaro, S. Dildick, K.M. Ecklund, S. Freed, P. Gardner, F.J.M. Geurts, A. Kumar, W. Li, B.P. Padley, R. Redjimi, W. Shi, A.G. Stahl Leiton, S. Yang, L. Zhang, Y. Zhang

University of Rochester, Rochester, U.S.A.

A. Bodek, P. de Barbaro, R. Demina, J.L. Dulemba, C. Fallon, T. Ferbel, M. Galanti, A. Garcia-Bellido, O. Hindrichs, A. Khukhunaishvili, E. Ranken, R. Taus

Rutgers, The State University of New Jersey, Piscataway, U.S.A.

B. Chiarito, J.P. Chou, A. Gandrakota, Y. Gershtein, E. Halkiadakis, A. Hart, M. Heindl, O. Karacheban[24], I. Laflotte, A. Lath, R. Montalvo, K. Nash, M. Osherson, S. Salur, S. Schnetzer, S. Somalwar, R. Stone, S.A. Thayil, S. Thomas, H. Wang

University of Tennessee, Knoxville, U.S.A.

H. Acharya, A.G. Delannoy, S. Fiorendi, S. Spanier

Texas A&M University, College Station, U.S.A.

O. Bouhali[94], M. Dalchenko, A. Delgado, R. Eusebi, J. Gilmore, T. Huang, T. Kamon[95], H. Kim, S. Luo, S. Malhotra, R. Mueller, D. Overton, D. Rathjens, A. Safonov

Texas Tech University, Lubbock, U.S.A.

N. Akchurin, J. Damgov, V. Hegde, S. Kunori, K. Lamichhane, S.W. Lee, T. Mengke, S. Muthumuni, T. Peltola, I. Volobouev, Z. Wang, A. Whitbeck

Vanderbilt University, Nashville, U.S.A.

E. Appelt, S. Greene, A. Gurrola, W. Johns, A. Melo, H. Ni, K. Padeken, F. Romeo, P. Sheldon, S. Tuo, J. Velkovska

University of Virginia, Charlottesville, U.S.A.

M.W. Arenton, B. Cox, G. Cummings, J. Hakala, R. Hirosky, M. Joyce, A. Ledovskoy, A. Li, C. Neu, B. Tannenwald, S. White, E. Wolfe

Wayne State University, Detroit, U.S.A.

N. Poudyal

University of Wisconsin - Madison, Madison, WI, U.S.A.

K. Black, T. Bose, C. Caillol, S. Dasu, I. De Bruyn, P. Everaerts, F. Fienga, C. Galloni, H. He, M. Herndon, A. Hervé, U. Hussain, A. Lanaro, A. Loeliger, R. Loveless, J. Madhusudanan Sreekala, A. Mallampalli, A. Mohammadi, D. Pinna, A. Savin, V. Shang, V. Sharma, W.H. Smith, D. Teague, S. Trembath-Reichert, W. Vetens

†: Deceased
1: Also at TU Wien, Wien, Austria
2: Also at Institute of Basic and Applied Sciences, Faculty of Engineering, Arab Academy for Science, Technology and Maritime Transport, Alexandria, Egypt
3: Also at Université Libre de Bruxelles, Bruxelles, Belgium
4: Also at Universidade Estadual de Campinas, Campinas, Brazil
5: Also at Federal University of Rio Grande do Sul, Porto Alegre, Brazil
6: Also at University of Chinese Academy of Sciences, Beijing, China
7: Also at Department of Physics, Tsinghua University, Beijing, China
8: Also at UFMS, Nova Andradina, Brazil

9: Also at Nanjing Normal University Department of Physics, Nanjing, China
10: Now at The University of Iowa, Iowa City, U.S.A.
11: Also at Institute for Theoretical and Experimental Physics named by A.I. Alikhanov of NRC 'Kurchatov Institute', Moscow, Russia
12: Also at Joint Institute for Nuclear Research, Dubna, Russia
13: Now at Cairo University, Cairo, Egypt
14: Also at British University in Egypt, Cairo, Egypt
15: Now at Ain Shams University, Cairo, Egypt
16: Also at Purdue University, West Lafayette, U.S.A.
17: Also at Université de Haute Alsace, Mulhouse, France
18: Also at Ilia State University, Tbilisi, Georgia
19: Also at Erzincan Binali Yildirim University, Erzincan, Turkey
20: Also at CERN, European Organization for Nuclear Research, Geneva, Switzerland
21: Also at RWTH Aachen University, III. Physikalisches Institut A, Aachen, Germany
22: Also at University of Hamburg, Hamburg, Germany
23: Also at Isfahan University of Technology, Isfahan, Iran, Isfahan, Iran
24: Also at Brandenburg University of Technology, Cottbus, Germany
25: Also at Forschungszentrum Jülich, Juelich, Germany
26: Also at Physics Department, Faculty of Science, Assiut University, Assiut, Egypt
27: Also at Karoly Robert Campus, MATE Institute of Technology, Gyongyos, Hungary
28: Also at Institute of Physics, University of Debrecen, Debrecen, Hungary
29: Also at Institute of Nuclear Research ATOMKI, Debrecen, Hungary
30: Also at MTA-ELTE Lendület CMS Particle and Nuclear Physics Group, Eötvös Loránd University, Budapest, Hungary
31: Also at Wigner Research Centre for Physics, Budapest, Hungary
32: Also at IIT Bhubaneswar, Bhubaneswar, India
33: Also at Institute of Physics, Bhubaneswar, India
34: Also at G.H.G. Khalsa College, Punjab, India
35: Also at Shoolini University, Solan, India
36: Also at University of Hyderabad, Hyderabad, India
37: Also at University of Visva-Bharati, Santiniketan, India
38: Also at Indian Institute of Technology (IIT), Mumbai, India
39: Also at Deutsches Elektronen-Synchrotron, Hamburg, Germany
40: Also at Sharif University of Technology, Tehran, Iran
41: Also at Department of Physics, University of Science and Technology of Mazandaran, Behshahr, Iran
42: Now at INFN Sezione di Bari [a], Università di Bari [b], Politecnico di Bari [c], Bari, Italy
43: Also at Italian National Agency for New Technologies, Energy and Sustainable Economic Development, Bologna, Italy
44: Also at Centro Siciliano di Fisica Nucleare e di Struttura Della Materia, Catania, Italy
45: Also at Università di Napoli 'Federico II', Napoli, Italy
46: Also at Consiglio Nazionale delle Ricerche - Istituto Officina dei Materiali, PERUGIA, Italy
47: Also at Riga Technical University, Riga, Latvia
48: Also at Consejo Nacional de Ciencia y Tecnología, Mexico City, Mexico
49: Also at IRFU, CEA, Université Paris-Saclay, Gif-sur-Yvette, France
50: Also at Institute for Nuclear Research, Moscow, Russia
51: Now at National Research Nuclear University 'Moscow Engineering Physics Institute' (MEPhI), Moscow, Russia

52: Also at Institute of Nuclear Physics of the Uzbekistan Academy of Sciences, Tashkent, Uzbekistan

53: Also at St. Petersburg State Polytechnical University, St. Petersburg, Russia

54: Also at University of Florida, Gainesville, U.S.A.

55: Also at Imperial College, London, United Kingdom

56: Also at P.N. Lebedev Physical Institute, Moscow, Russia

57: Also at California Institute of Technology, Pasadena, U.S.A.

58: Also at Budker Institute of Nuclear Physics, Novosibirsk, Russia

59: Also at Faculty of Physics, University of Belgrade, Belgrade, Serbia

60: Also at Trincomalee Campus, Eastern University, Sri Lanka, Nilaveli, Sri Lanka

61: Also at INFN Sezione di Pavia [a], Università di Pavia [b], Pavia, Italy

62: Also at National and Kapodistrian University of Athens, Athens, Greece

63: Also at Ecole Polytechnique Fédérale Lausanne, Lausanne, Switzerland

64: Also at Universität Zürich, Zurich, Switzerland

65: Also at Stefan Meyer Institute for Subatomic Physics, Vienna, Austria

66: Also at Laboratoire d'Annecy-le-Vieux de Physique des Particules, IN2P3-CNRS, Annecy-le-Vieux, France

67: Also at Şırnak University, Sirnak, Turkey

68: Also at Near East University, Research Center of Experimental Health Science, Nicosia, Turkey

69: Also at Konya Technical University, Konya, Turkey

70: Also at Istanbul University - Cerrahpasa, Faculty of Engineering, Istanbul, Turkey

71: Also at Piri Reis University, Istanbul, Turkey

72: Also at Adiyaman University, Adiyaman, Turkey

73: Also at Ozyegin University, Istanbul, Turkey

74: Also at Izmir Institute of Technology, Izmir, Turkey

75: Also at Necmettin Erbakan University, Konya, Turkey

76: Also at Bozok Universitetesi Rektörlügü, Yozgat, Turkey

77: Also at Marmara University, Istanbul, Turkey

78: Also at Milli Savunma University, Istanbul, Turkey

79: Also at Kafkas University, Kars, Turkey

80: Also at Istanbul Bilgi University, Istanbul, Turkey

81: Also at Hacettepe University, Ankara, Turkey

82: Also at Vrije Universiteit Brussel, Brussel, Belgium

83: Also at School of Physics and Astronomy, University of Southampton, Southampton, United Kingdom

84: Also at Rutherford Appleton Laboratory, Didcot, United Kingdom

85: Also at IPPP Durham University, Durham, United Kingdom

86: Also at Monash University, Faculty of Science, Clayton, Australia

87: Also at Università di Torino, TORINO, Italy

88: Also at Bethel University, St. Paul, Minneapolis, U.S.A., St. Paul, U.S.A.

89: Also at Karamanoğlu Mehmetbey University, Karaman, Turkey

90: Also at Bingol University, Bingol, Turkey

91: Also at Georgian Technical University, Tbilisi, Georgia

92: Also at Sinop University, Sinop, Turkey

93: Also at Erciyes University, KAYSERI, Turkey

94: Also at Texas A&M University at Qatar, Doha, Qatar

95: Also at Kyungpook National University, Daegu, Korea, Daegu, Korea